On the Impact of Three Dimensional Radiative Transfer on Cloud Evolution

Fabian Jakub

München 2016

On the Impact of Three Dimensional Radiative Transfer on Cloud Evolution

Fabian Jakub

Dissertation
at the Faculty of Physics
Ludwig-Maximilians-Universität
München

submitted by

Fabian Jakub

München, den 27. Juni 2016

Erstgutachter: Prof. Dr. Bernhard Mayer
Zweitgutachter: Prof. Dr. George Craig
Tag der mündlichen Prüfung: 2. August 2016

Contents

Zusammenfassung vii

Abstract viii

1 A Primer on Clouds and Radiation in the Atmosphere 1
- 1.1 Introduction . . . 2
- 1.2 Atmospheric RT . . . 4
- 1.3 Cloud modelling . . . 7
- 1.4 3D Approximations . . . 11

2 Methods 15
- 2.1 The TenStream solver . . . 15
  - 2.1.1 Method . . . 16
  - 2.1.2 Results and Discussion . . . 22
  - 2.1.3 Summary and Conclusions . . . 29
- 2.2 TenStream implementation in LES . . . 31
  - 2.2.1 Description of models and core components . . . 32
  - 2.2.2 Monte Carlo Spectral Integration . . . 34
  - 2.2.3 Performance Statistics . . . 35
  - 2.2.4 Conclusions . . . 41

3 Results 43
- 3.1 Warm-Bubble experiment . . . 45
  - 3.1.1 Influence of Atmospheric Radiative Heating . . . 46
  - 3.1.2 Coupling to an Interactive Surface Model . . . 51
  - 3.1.3 Influence of a Horizontal Wind . . . 56
  - 3.1.4 Discussion . . . 57
- 3.2 3D RT in Short Range Simulations . . . 63
  - 3.2.1 Shallow Cumulus . . . 63
  - 3.2.2 Cumulus Clouds with Surface Interaction . . . 69
  - 3.2.3 Evolution of a Shallow Cumulus Cloud Field with an Interactive Surface Model and a Horizontal Wind Profile . . . 76
  - 3.2.4 Discussion on the Shallow Cumulus Cloud Field Experiments 77

4 Summary and Conclusions 81
- 4.1 Summary . . . 81
- 4.2 Conclusions . . . 82

4.3 Outlook 84

Appendix **87**

Acknowledgments **95**

Zusammenfassung

In der vorliegenden Arbeit wird das Zusammenspiel von Wolken und Strahlung untersucht um die Rolle dreidimensionaler Strahlungstransfereffekte für die Entwicklung konvektiver Wolken zu ermitteln.

Die üblicherweise verwendeten eindimensionalen Strahlungstransfermethoden vernachlässigen jeglichen horizontalen Energieaustausch und führen zu erheblichen Fehlern in Bodenflüssen und atmosphärischen Erwärmungsraten. Der prominenteste Fehler eindimensionaler Verfahren tritt bei schräg einfallendem Sonnenlicht auf. Während eine Wolke natürlich seitlich beschienen werden sollte und der Bodenschatten dementsprechend versetzt sein müsste können, eindimensionale Verfahren die Wolke nur von oben bestrahlen und der Schatten befindet sich dementsprechend exakt unter der Wolke. Präzise dreidimensionale Strahlungstransfermethoden existieren bereits, sind aber mehrere Größenordnungen zu langsam um sie in einem numerischen Wettermodell zu nutzen.

In dieser Arbeit wurde ein schnelles und zugleich akkurates Verfahren zur Berechnung von dreidimensionalen Erwärmungsraten in der Atmospäre entwickelt. Das sogenannte TenStream Verfahren wurde in das wolkenauflösende Grobstrukturmodell UCLA–LES implementiert und erlaubt die Untersuchung der Effekte von dreidimensionalem Strahlungstransfer auf die Wolkenbildung und -entwicklung.

Das TenStream Verfahren erweitert das bekannte eindimensionale Twostream Verfahren indem es 10 statt nur 2 Strahlungsflüsse berücksichtigt und damit eine deutlich höhere Genauigkeit bei der Berechnung von Erwärmungsraten ermöglicht. Beispielsweise verringert sich der Fehler bei der Berechnung einer Szene mit Cumulus-Bewölkung von 178 % auf 31 %.

Die Effizienz des Verfahrens auf modernen, höchst parallelen Rechnerarchitekturen ist ein besonders wichtiger Aspekt und wird in “weak-” und “strong-scaling” Experimenten detailliert untersucht. Im Speziellen wurden bei diesen Experimenten zwei Methoden zur Vorkonditionierung von Matrizen untersucht: Ein algebraisch-geometrisches Mehrgitterverfahren und eine unvollständige LU-Zerlegung wobei sich besonders das Mehrgitterverfahren bei komplexen Szenen und hoher Parallelisierung auszeichnet. Das Verfahren wurde auf mehreren Super-Computern mit bis zu 4096 Prozessoren geprüft und zeigt eine parallele Skalierbarkeit von 80 bis 90%.

Die Untersuchungen innerhalb des UCLA–LES zielen darauf ab, den Einfluss von dreidimensionalem Strahlungstranfer auf einzelne Wolken innerhalb ihrer Lebenszeit von unter einer Stunde zu quantifizieren. Weitergehend werden die Methoden auch auf längere Zeitskalen und grössere Modellgebiete mit flacher Cumulus Bewölkung angewendet. Die Ausrichtung der direkten Sonneneinstrahlung

führt zu einem ungleichmässigem Aufheizen der Wolken und damit zu einer asymetrischen Entwicklung der Wolke. Dadurch, dass der Schatten der Wolke nicht mehr direkt unter der Wolke auftritt wird den bodennahen Schichten im Aufwindbereich weiterhin Energie zugeführt. Diese Energiezufuhr sensibler und latenter Wärme verlängert die Lebensdauer der Wolke um das zweifache und verstärkt die Wolkenentwicklung im Allgemeinen. Der Einfluss von dreidimensionalem Strahlungstransfer auf das Wolkenwachstum bleibt in den untersuchten Szenarien trotz eines horizontalen Windes bestehen.

Die in dieser Arbeit entwickelten Methoden und gezeigten Ergebnisse bilden die Grundlage für weitergehende Studien zur Wechselwirkung von Strahlung und Wolken und sind ein wichtiger Schritt für ein verbessertes Verständniss von Wetter und Klima.

Abstract

The goal of this study is to gain insight into cloud-radiative feedback mechanisms and what role three-dimensional radiative transfer effects play in the evolution of convective clouds. The usually employed one-dimensional radiative transfer solvers neglect any horizontal energy transfer and thereby introduce considerable errors in surface and atmospheric heating rates. While fully three-dimensional radiative transfer solvers exist, they are several orders of magnitude too slow. In conclusion, so far, there is no straightforward solution that would solve the task at hand — namely, compute accurate three-dimensional radiative heating rates in the atmosphere — fast enough to be coupled interactively to a cloud resolving model.

This thesis presents a new method — the TenStream solver — that provides a fast yet accurate approximation for three-dimensional heating rates. The TenStream is furthermore integrated into the University of California, Los Angeles large-eddy simulation (UCLA-LES) cloud-resolving model. This setup allows to study the effects of three-dimensional radiative heating on the evolution of clouds.

The TenStream method extends the well-known one-dimensional two-stream theory to 10 streams. The new solver significantly reduces the root mean square error for atmospheric heating and surface heating rates when compared to traditionally employed one-dimensional solvers. In the case of a cumulus cloud field and the solar zenith angle being 60°, the error is reduced from 178 % to 31 %.

Parallel scalability was a primary concern developing the TenStream solver. This thesis documents the overall performance of the solver as well as the technical challenges of migrating from 1-D schemes to 3-D schemes. To understand the performance characteristics of the TenStream solver, weak as well as strong-scaling experiments are conducted. In this context, two matrix preconditioner are investigated: geometric algebraic multigrid preconditioning (GAMG) and block Jacobi incomplete LU (ILU) factorization and it is found that algebraic multigrid preconditioning performs well for complex scenes and highly parallelized simulations. The TenStream solver is tested on several state of the art super-computers for up to 4096 cores and shows a parallel scaling efficiency of 80 % to 90 %.

The central part of this thesis examines the influence of three-dimensional radiative transfer effects on the development of convective cumulus clouds. The influence is tested on short time scales of a single convective warm-bubble and over a longer period of time and a reasonably large domain for shallow cumulus clouds. The directionality of the direct solar beam introduces an asymmetry in the atmospheric heating of the convective motion and tilts the updraft. While a cloud's shadow is always directly beneath itself in a one-dimensional radiative transfer solver. In contrast, the TenStream solver correctly displaces the shadowy region

according to the sun's zenith angle. The constant supply of warm and moist air due to the local heating in the updraft region beneath the cloud, prolongs the cloud's lifetime by a factor of two and generally increases cloud development. The influence of three-dimensional heating on the evolution of clouds shows to be persistent even in the presence of a horizontal wind.

The results presented here motivate further research in the field of cloud-radiative feedbacks and their role in weather and climate prediction simulations.

Chapter 1

A Primer on Clouds and Radiation in the Atmosphere

1.1 Introduction

Until today, the Intergovernmental Panel on Climate Change (IPCC) points out that deficiencies in the representation of clouds remain the biggest source of uncertainty for climate predictions. Besides, short term weather forecasts are equally dependent on a sound description and understanding of cloud processes. If we are to improve our understanding of cloud physical processes it is of paramount importance that we further our knowledge of clouds and their intricate link to radiative processes.

Radiation is the single most effective energy transport mechanism in the atmosphere and interacts with every aspect of the earth system. Radiation authoritatively influences the surface energy budget and drives local convection. Solar radiation, emitted by the sun, warms the atmosphere and the surface and is by far the most important source of energy on our planet. Thermal radiation is emitted by clouds and the surface. Clouds influence the radiation budget by reflecting solar radiation back to space or trapping thermal radiation from the surface. At the same time, clouds emit radiation back towards the surface and out space. Those often fluffy shapes of white regulate the earth energy budget by interaction with radiation and redistribute heat and moisture through convection. The fractal nature of clouds over many spatial scales make them particularly hard to represent in numerical models. Clouds incorporate processes over a wide range of spatial and temporal scales. At the micro-scales, microphysical processes such as droplet nucleation, coagulation, or the formation of rain and snow occur on time scales of seconds. At the same time, cloud systems may reside for hours or days and may influence the flow they reside in through adiabatic or radiative processes.

One goal of the " **H**igh **D**efinition **C**louds and **P**recipitation for **C**limate **P**rediction ", the HD(CP)^2 project is to improve our understanding of cloud-radiative processes through high-resolution modeling to ultimately enhance parameterizations for climate prediction. The HD(CP)^2 project targets at a model resolution of 100 m where the major part of convective clouds are supposed to be resolved. This allows to go from statistical cloud parameterizations to physics based convection schemes. This shift also necessitates the correct treatment of solar and thermal radiative transfer (RT).

Virtually all radiative transfer methods employed in todays atmospheric models depend on the so called plane-parallel approximation. The radiative transfer equation (introduced in section 1.2, eq. (1.1)) only has an analytic solution if we assume the atmosphere to be an infinite, horizontally homogeneous, slab. Solvers that depend on the plane-parallel approximation are inherently one-dimensional. To account for horizontally varying conditions, one usually employs the so called "**I**ndependent **C**olumn **A**pproximation" (ICA) where the atmosphere is sub-divided into adjacent vertical columns and the RT is computed for each vertical column independent of each other. While this proves to be fast computationally, it does, by definition, not allow for any horizontal energy exchange between columns. The ICA has two major flaws when applied to high resolution models. First, the direct solar beam should obviously be allowed to propagate horizontally according to the sun's zenith angle. Clouds are consequently only illuminated from the top, and the shadow falls always directly beneath the cloud. The second shortcoming of the

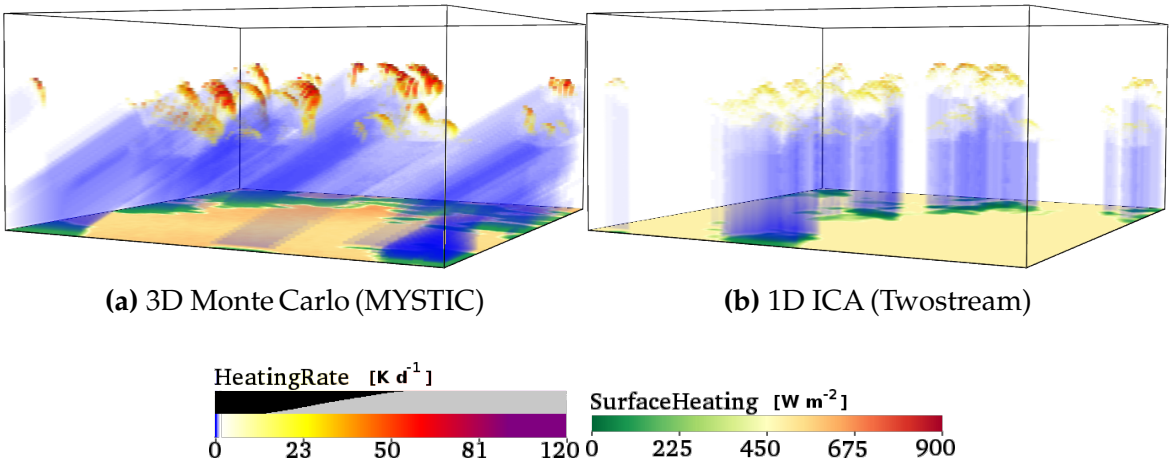

(a) 3D Monte Carlo (MYSTIC) **(b)** 1D ICA (Twostream)

Figure 1.1: Volume rendered perspective on solar atmospheric and surface heating rates of a cumulus cloud field (see section 2.1.2 for details). On the left a benchmark 3D Monte Carlo MYSTIC calculation, and on the right a 1D Twostream computation with ICA. It is clear that the ICA is not able reproduce the 3D RT effects, namely the cloud side illumination and the displacement of the shadow.

ICA concerns the diffuse radiation (e.g. scattered or emitted by a cloud) which is confined to its own column (see fig. 1.1).

Recent studies have shown that 3D RT — currently neglected by all atmospheric models because of the associated high computational cost — may have considerable impact on cloud formation and precipitation. Guan et al. [1997] studied the influence of thermal RT on the evolution of cumulus clouds and found thermal cooling to increase the liquid water content. Klinger [2015] inspected the influence of thermal 3D radiative heating rates on the evolution of single convective plumes and shallow cumulus clouds.

O'Hirok and Gautier [2005] applied a 3D RT model in a 2D model setup and studied differences in cloud dynamics due to solar atmospheric- and surface heating rates. Schumann et al. [2002] parametrized the displacement of the cloud's shadow on the surface and studied the influence of this asymmetry on the structure and evolution of the boundary layer dynamics and turbulence. Wapler [2007] applied the "Tilted Independent Pixel Approximation" (TIPA, see section 1.4) to numerical experiments with a cloud resolving model and examined the influence of displaced shadows in a more rigorous, physically correct way. She found that the differential solar surface heating induces an asymmetry in the circulation and leads to differences in cloud lifetimes and the production of turbulent kinetic energy. Frame et al. [2009] described differences between IPA and TIPA computations for deep convective thunderstorm simulations but refrained from drawing conclusions upon the role of 3D RT.

In any case, those studies were either limited to very short times, limited to thermal or solar radiative transfer only or accounted only for changes in surface fluxes. It remains to be shown what the effects are when we consider 3D RT in the atmosphere as well as on the surface, in the solar as well as in the thermal spectral range.

The goal of this dissertation is to answer the corresponding question:

Do effects of three-dimensional radiative transfer have an influence on the development and evolution of clouds and if so, how?

Currently available 3D RT solvers (Monte Carlo based (e.g. Mayer [2009]) or SHDOM (Evans [1998])) are cumbersome to use because of their extraordinary computational burden. As a consequence, the first step of this work is to develop a three-dimensional solver, which is able to compute realistic atmospheric heating rates, yet is fast enough to run in high resolution models. The second step will be to implement this RT solver into a cloud resolving model and finally conduct numerical experiments to analyze the effects of 3D RT on the evolution of clouds.

Section 1.2 will give a very brief introduction into the wonderful world of radiative transfer modeling, followed by a short introduction to atmospheric cloud- and surface models (section 1.3). This will give the necessary background to understand the concepts of the new RT method and the interpretation of the simulation results. The new RT method is described in detail in chapter 2, followed by a description and interpretation of the simulation results in chapter 3. Chapter 4 will give a summary of this dissertation, conclusions of the key findings of this work and an outlook for further research.

1.2 Radiative transfer in the Atmosphere

Mmmmhhhh...
...Radiation

Homer Simpson

The goal of this sections is to provide the interested radiative transfer novice with just enough knowledge about atmospheric radiative transfer so that he may follow the discussion of the TenStream solver in chapter 2.

The aspiring RT modeler will undoubtedly long for a more thorough introduction to radiative transfer theory. Zdunkowski et al. [2007] provides an excellent insight into general RT concepts including modern applications. Another work that I found to be an invaluable resource for information on three-dimensional radiative transfer is the book of Marshak and Davis [2005]. Regarding Monte Carlo methods to compute the RT in complex atmospheres, I would like to promote the vivid work of Mayer [2009].

Let's start with the holy-grail of radiative transfer, the radiative transfer equation (RTE). We can write the RTE for monochromatic light in its differential form as

$$\frac{\mathrm{d}L}{k_{\text{ext}} \cdot \mathrm{ds}} = -L + \frac{\omega_0}{4\pi} \int_{4\pi} \underbrace{p(\Omega', \Omega)\, L(\Omega')}_{\text{scattering}} \, \mathrm{d}\Omega' + (1-\omega_0) \underbrace{B_{\text{Planck}}(T)}_{\text{emission}} \tag{1.1}$$

where it describes the change of radiance L along a path ds. L is defined as the energy Q per time t, per unit angle Ω and per projected area $A \cos\theta$ and is given in units of [W sr^{-1} m^{-2}]:

$$L = \frac{\delta Q}{\delta t \, \delta\Omega \, \delta A \cos\theta} \tag{1.2}$$

The first component of the RTE expresses the change of radiance due to extinction (removal of radiation from the given path). The extinction coefficient k_{ext} $[m^{-1}]$ is the sum of the respective coefficients for absorption (k_{abs}) and scattering (k_{sca}). The second term describes the in-scattering of radiation into the direction Ω currently considered. In other words, along the path ds we consider all photons which initially travel to different directions $\Omega^{'}$ and change their direction into Ω. The probability function $p(\Omega^{'}, \Omega)$ is called the scattering phase function and primarily depends on the shape and size of the scattering particle. The coefficient ω_0 is termed "single scattering albedo" and defines the ratio of scattering compared to the extinction, i.e.

$$\omega_0 = \frac{k_{\text{sca}}}{k_{\text{ext}}}$$

The last term of the RTE describes the emission of radiation according to Planck's Law (black body emission at temperature T), where the pre-factor $(1 - \omega_0)$ denotes the absorption coefficient of the medium (Kirchhoff's law of thermal radiation states that emission equals the absorption).

The integral in the second term is what makes the RTE an integro-differential equation and also what makes it so difficult to solve. The fact that radiation, incident from all directions, may contribute to the local radiance makes it necessary to solve the radiative transfer for all angles at once. Very often, in remote sensing applications, we are indeed interested in particular radiances, however for the application of heating rates we are usually quite content to get the flux through a horizontal plane (e.g. the surface). For that let's introduce the upward and downward radiant flux or irradiance E,

$$\vec{E}_{\uparrow} = \int_0^{2\pi} \mathrm{d}\phi \int_0^1 \mu \vec{L}(+\mu, \phi) \mathrm{d}\mu \tag{1.3}$$

$$\vec{E}_{\downarrow} = \int_0^{2\pi} \mathrm{d}\phi \int_0^1 \mu \vec{L}(-\mu, \phi) \mathrm{d}\mu \tag{1.4}$$

, where μ is the cosine of the zenith angle, and ϕ the azimuth. Note here, that the irradiance is just the mean radiance at the considered plane, weighted by the cosine of the angle between the plane normal and the beam direction. Irradiance can then be used to derive the absorbed energy Q (divergence of radiation) in a volume by using the Gauss's divergence theorem that states that the divergence in a volume can be written as the normal flux through the boundary of that volume.

$$\frac{\mathrm{d}Q}{\mathrm{d}t} = \iiint_V \boldsymbol{\nabla} \vec{E} \, dV = \oiint_S \vec{E} \cdot \vec{n} \, dS \tag{1.5}$$

I will not go into the details of various methods how to solve the RTE but name-dropping the most widely used methods may be instrumental for a quick start into the literature. The following list will introduce the most-widely used one-dimensional methods in atmospheric models and remote sensing applications:

Schwarzschild Neglecting the scattering term in the RTE (eq. (1.1)) yields the so called Schwarzschild equation. This reduces the problem to an ordinary inhomoge-

neous partial differential equation with the solution:

$$L(\tau, \mu, \phi) = L(\mu, \phi) \exp(-\tau/\mu) + B_{\text{Planck}}(T)(1 - \exp(-\tau/\mu))$$

where $\exp(-\tau/\mu)$ is the transmission through the layer, according to Lambert-Beer's law with $\tau = k_{\text{abs}} * \text{dz}$. Omitting the scattering term is only a good approximation in the thermal spectral range. There, because of a generally low single-scattering albedo values (absorption dominating the optical depth), we find the schwarzschild method to be surprisingly accurate. If the integral in eq. (1.4) is furthermore evaluated with only one representative zenith angle μ, the schwarzschild method reduces to two exponential function evaluations per layer and is thus extremely efficient computationally.

DISORT The DIScrete-Ordinate-method for Radiative Transfer expands the phase function p in eq. (1.1) in a series of Legendre polynomials and the intensity in Fourier terms. Further mathematical wizardry leads to a set of independent integro-differential equations which may be solved numerically. The accuracy of DISORT depends on the size N of the expansions, termed the "number of streams". A common number of streams for the accurate computation of fluxes is $N = 16$. See Chandrasekhar [2013] for the method or Stamnes et al. [1988, 2000] for an implementation.

Twostream The Twostream method is a special case of the DISORT algorithm for $N = 1$, i.e. one upward and one downward stream. The error for heating rates is usually less than 10 % compared to more accurate DISORT computations. Twostream solvers are by far the most widely used radiative transfer solvers in current atmospheric models. More details are given later in section 2.1.1.

Further along we also have the three-dimensional methods which are generally not used in atmospheric model, owed to the fact that they are extraordinarily demanding computationally. To my knowledge, there exist only two methods to solve the RTE in three-dimensions with arbitrary precision:

SHDOM The Spherical-Harmonics-Dicrete-Ordinate-Method (Evans [1998], Evans and Wiscombe [2003])[1], is an iterative method to solve the RTE. First, the source function is determined in a spherical harmonics expansion, then multiple scattering is solved in the discrete ordinate representation, and finally the new source functions are computed. A recent version is MPI-parallelized and supports adaptive mesh-refinement in terms of grid cells as well as the truncation of spherical harmonics terms. Pincus and Evans [2009] found that SHDOM is favorable compared to Monte Carlo methods in terms of computational efficiency, when we are interested in the full field of radiances in scenes with low optical depth. SHDOM needs the cell optical depth to be smaller than one and thus may adaptively split the mesh unfeasibly often in case of high optical thicknesses. For heating rates, SHDOM is found to be comparable in terms of computation efficiency as Monte Carlo solvers.

[1] the name "SHDOM" describes the method and at the same time also the name of the code — there is only one code base

Monte Carlo Monte Carlo methods are probably the most versatile and, given the computational resources, also the most accurate ones. The principal idea of Monte Carlo radiative transfer is to not explicitly solve the radiative transfer equation, but rather to model the underlying processes i.e. absorption and scattering. Statistical sampling of individual photon paths yields the desired solution to the radiative transfer equation. In other words, we start plenty of photons at the source, e.g. the sun shining at top of the atmosphere, and then trace the individual photons through the atmosphere. When a photon is for example scattered on a cloud, we throw the dice according to the phase function and we set a new direction for the photon. To know for example how much radiation reaches the surface, we merely have to count the number of photons that are traced there.

As a final remark, I'd like to point out that lab experiments as well as passive and active measurements through the atmosphere give every reason to believe that radiative transfer theory works. Mayer et al. [2005] and Emde et al. [2016] include a list of studies where the solvers used in this work are compared to other implementations as well as comparisons to field measurements.

At the same time, atmospheric radiative divergence or heating rates are notoriously difficult to measure directly. One attempt for such measurement was done by Gerber et al. [2014] within the aircraft field campaign termed POST (Physics of Stratocumulus Top). Figure 1.2a shows the measured heating rates and a pink line with a single column radiative transfer computation using averaged atmospheric conditions during the campaign. In an attempt to explain the measured data (personal correspondence), I performed a simulation of a stratus cloud, notably not specifically attuned to the campaign, with the UCLA–LES and the TenStream radiative transfer solver. One notable difference to the measurements (fig. 1.2b) is the variable cloud top height in the UCLA–LES simulation, which leads to a range of thermal cooling rates. The fact that the simulation of heating rates are otherwise in such a good agreement gives confidence that we understand the principal physics that determine radiative heating in the atmosphere.

1.3 Cloud modeling with Large Eddy Simulations

A trusted tool to further our understanding in atmospheric science is to use numerical models to study earth's atmosphere. The basis of these models is a set of equations called the Navier-Stokes equations. The Navier-Stokes equations describe the motion of a fluid and its properties such as pressure and density. Solving the full Navier-Stokes equations is however a daunting task. Atmospheric motions range over a wide range of spatial scales. Resolving the smallest eddies in numerical models needs excessively fine meshes and is therefore unfeasibly expensive computationally. Models that resolve all eddies directly are so called direct numerical simulations (DNS) and recent advances in computer technology allow to solve domains with grid sizes of several centimeters. For now however, we have to accept some approximations if we want to numerically simulate the weather.

An enormously successful approach was proposed by Smagorinsky [1963] called Large-Eddy-Simulations (LES). The key idea is to resolve only the large

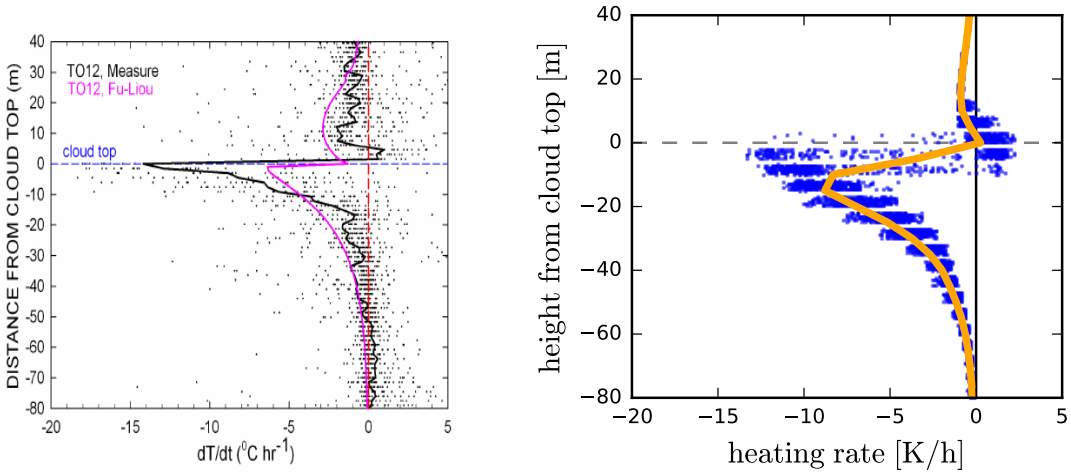

(a) (b)

Figure 1.2: (a) measurement data from the POST campaign (picture taken from Gerber et al. [2014]). The pink line is a single column radiative transfer calculation for averaged conditions during the campaign. (b) thermal heating rates derived from a high resolution ($\Delta x = 5m$) simulation with UCLA–LES and the TenStream solver. Cloud top in the simulation is around 880 m.

eddies of the flow while the computationally more expensive small eddies are parametrized. In our case for example, if we are interested in boundary layer processes we would surely like to resolve eddies of tens of meters to kilometers whereas we may be able to live with the fact that turbulent mixing and diffusion is not explicitly resolved. I recommend the review article of Zhiyin [2015] for more detailed information on the current state of LES and its implementations. LES have been successfully used to study boundary layer structure as well as shallow and deep convective systems. While the Navier-Stokes equations govern the dynamical evolution of the fluid flow, there are of course many more physical processes that have to be accounted for. One important aspect is of course the radiative transfer which will be handled in this thesis extensively. Another one is for example the microphysics scheme which parametrizes phase changes of water, modeling droplet growth rates and evaporation to form clouds or precipitate them. Additional processes include the exchange at the lower boundary, i.e. with a surface- or ocean-model. All parameterizations beyond the "dynamical core" (Navier-Stokes) are usually called "model physics".

The basic flow of an atmospheric model run is to start the simulation with initial conditions and the governing equations will compute the tendencies (rate of change) for variables such as moisture or temperature. These tendencies will then be applied for a certain timestep. Given the updated state of the atmosphere, the model then computes new tendencies. Consecutively looping through timesteps integrates the simulation forward in time. Physics parameterizations are applied at each timestep to further update variable tendencies. Radiative heating for example acts on the temperature tendency at the surface and in the atmosphere.

The model used in this study is the University of California Los Angeles — Large-Eddy Simulation (UCLA-LES). A description and details of the UCLA-LES model can be found in Stevens et al. [2005] and Savic-Jovcic and Stevens [2008]. To satisfy the technically affectionate reader we should briefly point out the key aspects of the model. The prognostic variables in the UCLA-LES are the wind $u_{x,y,z}$, the liquid-water potential temperature θ_l, and the total water mixing ratio q_t. Time stepping is based on a third order Runge-Kutta method allowing for adaptive timesteps (controlled by CFL criteria). The numerical grid is a doubly periodic (what goes out on the right, comes in to the left) Arakawa-C grid and the parallel domain decomposition is done in 2D. Advection uses fourth-order central differences (two ghost cells) and the pressure term is solved with a 2D Fast-Fourier transform.

The here presented introduction to temperature variables and atmospheric stratification should give the reader just enough tools to follow the discussions in chapter 3. For a more details on atmospheric dynamics, I recommend the introductory chapters in Holton and Hakim [2012] and the work of Vallis [2006].

The meteorologist likes to think of an "air parcel" as an abstract container of air which can be moved around but does not exchange energy or substance with its environment. It is therefore subject to adiabatic transformations, e.g. if an air parcel is lifted it will expand due to lower surrounding pressure and thus lower its temperature. If the air parcel is still warmer than the surrounding air it will continue to rise. This is expressed with the dry adiabatic lapse rate

$$\Gamma = -g/c_{p,dry} = -9.76\,\mathrm{K\,km^{-1}}$$

with g =9.81 m s^{-2} being the gravitational acceleration and the specific heat capacity of dry air at constant pressure $c_{\mathrm{p,dry}}$ =1004 J kg^{-1} K^{-1}.

To discuss the stability of the atmosphere it is convenient to compare temperatures at different heights directly. For that, meteorologists often use the potential temperature as

$$\theta = T\left(\frac{p_0}{p}\right)^{\frac{R_L}{c_{p,dry}}} \tag{1.6}$$

where $\mathrm{R_L}$=287 J kg^{-1} K^{-1} is the specific gas constant of dry air. The potential temperature is the temperature the air parcel would have if the parcel is adiabatically moved from pressure environment p to the reference pressure p_0, e.g. to the surface. With that, we can easily compare the temperatures of different air parcels from different heights. One handy extension is the liquid water potential temperature θ_l which further incorporates a term to describe the evaporation of liquid water droplets.

$$\theta_l = \theta - r_l \frac{L_v}{c_{p,dry}} \tag{1.7}$$

where L_{v} =2400 kJ kg^{-1} is the latent heat release of evaporation and r_l the liquid water mixing ratio. In other words, we may have a cloudy air parcel and ask what temperature would it have if we were to evaporate all the liquid water inside.

Figure 1.3 depicts the three possible states for stratification in the atmosphere. The potential temperature easily allows to determine if an air parcel will rise or not. If the vertical gradient is zero the air can effortlessly move up and down adiabatically and will always have the same temperature as the surrounding air. In contrast, if the lower air is warmer than the air above, we have an unstable situation and the air will tend to rise upwards. In the provided example, we can see that the near surface air, with it's temperature at 302 K will rise up to a height where the environment is warmer than itself, here approximately 1.8 km. Convective motion will basically sort the potential temperature into a monotonously increasing profile.

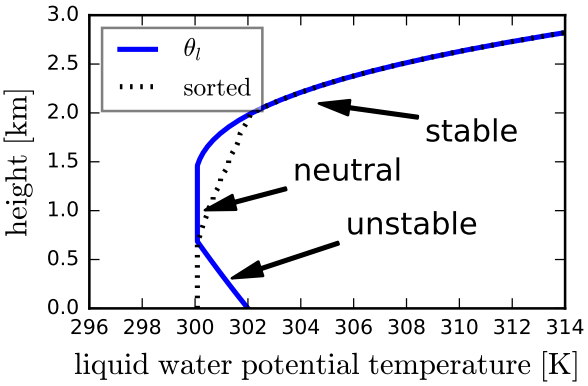

Figure 1.3: Possible configurations for the atmospheric stratification. Stable layers are in equilibrium with respect to vertical adiabatic displacements. Unstable air will rise up to a point where the environment is warmer. The dynamics will tend to rearrange the atmosphere (sort) so that the potential temperature is monotonically increasing with height (dashed line).

The up or downward acceleration of an air parcel is given by its local temperature gradient with respect to its surrounding air. The buoyancy B of air parcels can be written as:

$$B = g\frac{T_v - T_{v0}}{T_{v0}} \tag{1.8}$$

where T_v is the virtual temperature with respect to water vapor r_v and liquid water mixing ratio r_l:

$$T_v = T(1 + \epsilon\, r_v - r_l)$$

The ϵ is the ratio of the specific gas constants of dry air and of water vapor

$$\epsilon = R_{dry}/R_v = 0.61$$

Using the virtual temperature allows to use the definitions with the specific gas constant of dry air also for moist conditions.

The last quantity that we may use to characterize the stability of the atmosphere is the equivalent potential temperature. The definition is as in eq. (1.7) with the equivalent temperature T_e. The equivalent temperature is the temperature an air parcel would have if we condensed all water vapor and use the released latent energy to heat the air.

$$T_e = T + q\frac{L_v}{c_{p,dry}} \tag{1.9}$$

where q is the total water vapor. The equivalent potential temperature is a conserver quantity if we assume no mixing of air parcels. This comes in handy to study entrainment processes where we can use it as a scalar tracer.

The lower boundary, Land-Surface-Models One important part in numerical simulations is the treatment of boundary conditions, particularly the lower boundary. We generally want to determine the latent (surface evaporation) F_{latent} and sensible heat $F_{sensible}$ fluxes between the ground and the adjacent airmass. A simple but effective parametrization is to just use fixed fluxes. According to Wild et al. [2013], the globally averaged surface fluxes are about $F_{\text{latent}} = 85\,\text{W}\,\text{m}^{-2}$ and $F_{\text{sensible}} = 20\,\text{W}\,\text{m}^{-2}$. This does however not allow for any variability or feedback with the atmosphere. A common approach to couple a more realistic ocean surface to the dynamics model is to use a bulk-model with a fixed sea surface temperature. Latent and sensible heat flux are determined using the local wind and the temperature gradient between sea- and air-temperature. For our purposes, i.e. to study the immediate effects of radiative heating at the surface, both these approaches are inadequate. We need a more detailed coupling to solve the energy exchange between the surface, the atmosphere and radiation. The Land-Surface-Model (LSM) that is implemented in the UCLA–LES is adopted from the Dutch Atmospheric LES (DALES, see Heus et al. [2010]). To learn more about the implementation of the LSM in UCLA–LES, I highly recommend the work of Rieck et al. [2015]

The energy balance equation at the surface describes the rate of change of the surface temperature and can be written as

$$c_{srfc}\frac{dT_{srfc}}{dt} = Q_{net} - F_{latent} - F_{sensible} - F_{soil} \tag{1.10}$$

where c_{srfc} is the heat capacity and Q_{net} the net radiative flux at the surface (solar and thermal). The energy flux F_{soil} describes the exchange of heat with the underlying ground layers. The solution process can be subdivided into two parts. First, one solves the surface energy balance equation for a so called skin layer. The skin layer is a virtual layer that has either no heat capacity or takes the heat capacity of the vegetation. Sensible and latent heat fluxes are related to the atmospheric state above the surface, i.e. linking them to air temperature, wind speed and surface roughness through a resistance formulation (see Rieck et al. [2014] for details). A second step determines the subsurface energy exchange between multiple soil layers.

1.4 A brief review on 3D RT approximations

The goal of this section is to give a historic introduction to the available approximations for three-dimensional radiate transfer. This will provide a rationale as to why I think we need a fresh approach and yet another radiative transfer solver.

In the past the modeling community has put a significant amount of work into the development of fast parameterizations to incorporate first order three dimensional effects into radiative transfer computations while retaining the computational speed of one dimensional solvers. Zuidema and Evans [1998] introduced the " **T**ilted **I**ndependent **P**ixel **A**pproximation " (TIPA), which is sometimes also called " **T**ilted **I**ndependent **C**olumn **A**pproximation " (TICA).[2] The idea of the TIPA is to

[2] As a side note, it is quite common to see literature use both, "Pixel" and "Column" interchangeably

Figure 1.4: Clouds come in many shapes and forms with unique ways of interacting with radiation.

calculate the direct solar beam on a slanted path through the atmosphere whereas the diffuse radiation is still computed on the vertical grid. Varnai and Davies [1999] proposed an alternative realization of the TIPA where they compute the direct beam and the diffuse radiation along the tilted path. Both methods greatly improve the representation of the direct radiation but still do not account for horizontal diffuse radiative transfer. Marshak et al. [1998] introduced the "**N**on-local **I**ndependent **P**ixel **A**pproximation" (NIPA) where they proposed to use a two-dimensional convolution of the surface fluxes to account for radiative smoothing.

The TIPA and NIPA promised to overcome the limitations of one-dimensional radiative transfer at low computational cost [Schumann et al., 2002, Wapler and Mayer, 2008]. However, it turns out that the TIPA introduces unphysical high peaks along cloud edges and needs to be used in conjunction with NIPA. At the same time, the NIPA needed some prior knowledge about the width of the convolution kernel that is usually not readily available. Wissmeier et al. [2013] parametrized the kernel width as a function of the distance to the nearest cloud and successfully developed a standalone algorithm (paNTICA) to compute vastly improved surface fluxes.

Jakub [2013] extended the idea of paNTICA to compute radiative fluxes also in the atmosphere. The resulting algorithm Ξ TIPA was implemented in the numerical weather prediction model, COSMO. While the approach considerably reduced errors in radiative fluxes, it turned out that the unphysical decoupling and smoothing of individual fluxes made the calculation of flux divergence (heating rates) difficult. The resulting heating rates did not show to be as accurate as we hoped for.

At the same time it became clear that as we went to higher resolutions (well be-

low 1 km) and ever higher parallelized compute architectures, we would run into problems. The smoothing operator (convolution) meant trouble concerning the parallel scaling efficiency and the algorithm did not promise to retain high accuracy for very high resolutions below 100 m. The idea that we can use well-tested one-dimensional solvers and account for three-dimensional effects in a post-processing step indeed sounds appealing, however, to me it seemed to be a dead-end.

This was when I decided that we needed a new, rigorous, and physically sound mechanism to couple radiative transfer horizontally. Figure 1.5 schematically compares the accuracy and computational complexity of the above mentioned solvers. It is clear that selecting the right radiative transfer solver for a given simulation will always be a compromise between speed and precision. One approach often taken is to use the most sophisticated algorithm there is and from there, deduce which simplifications do not affect the results. This shows to be difficult in the case of radiative transfer methods because simulating realistic scenarios with accurate and fully three-dimensional solvers such as SHDOM or MonteCarlo are too demanding computationally. That being said we have to keep in mind, that even if we were able to use a "perfect" solver there always remain uncertainties in other aspects of the radiative transfer calculations. For example, the use of analytic, simplified scattering phase functions for water droplets (e.g. Henyey-Greenstein in contrast to Mie tables) introduces relative errors in heating rates on the order of 10 %. So if we were to put up a wish list for a radiative transfer solver to drive large-eddy simulations with resolutions of about 100 m we want it to reproduce first order three dimensional effects with an accuracy of approximately 10 % to 20 % with a computational efficiency close to existing one-dimensional solvers.

Chapter 2 will present a fresh approach that allows to compute three-dimensional solar- and thermal radiative heating rates, scales well on highly parallel machines, and is flexible enough to attain high accuracy given the computational resources.

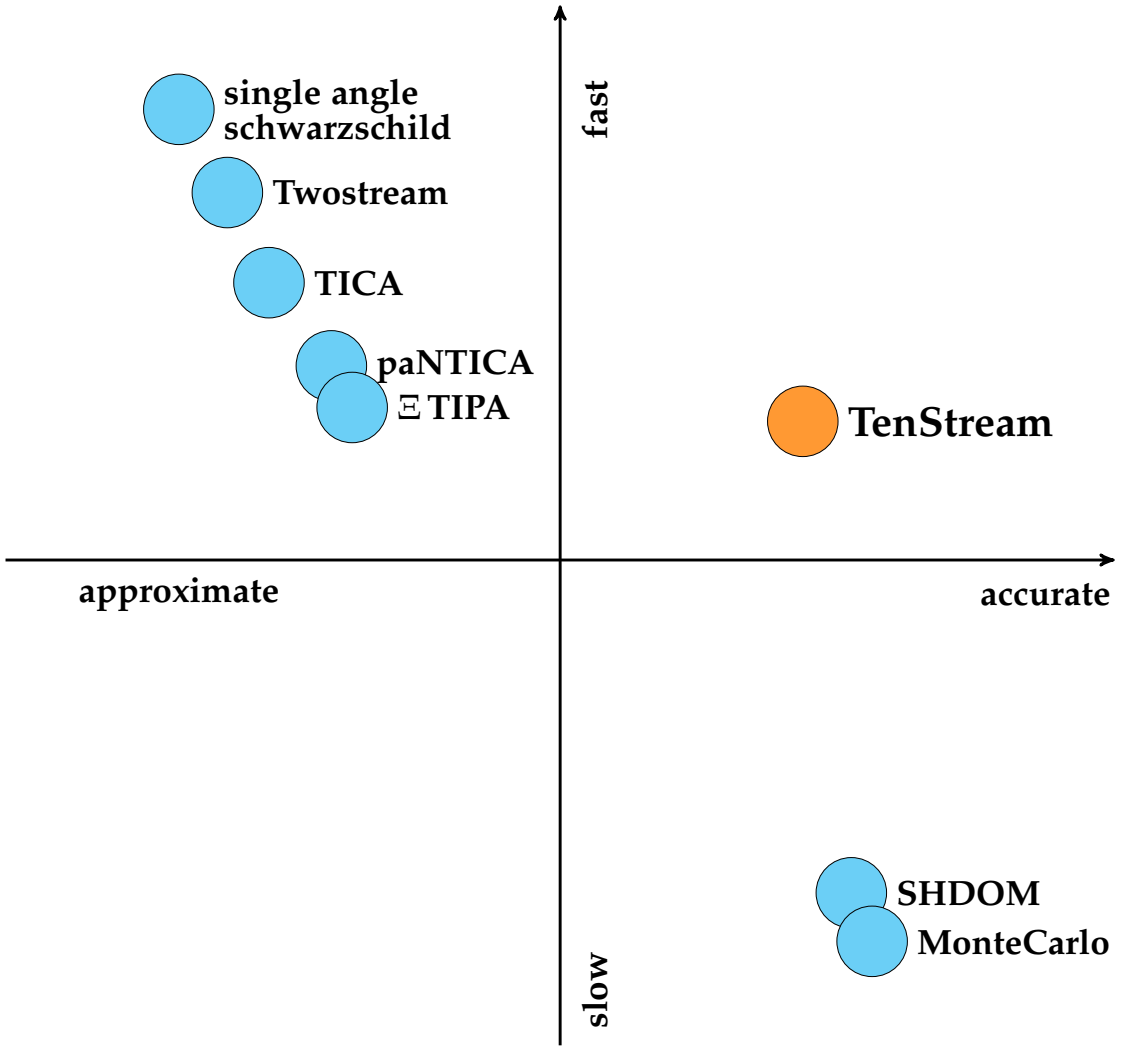

Figure 1.5: Schematic performance overview of usually employed radiative transfer solvers and three-dimensional approximations. Rigorous three-dimensional solvers such as SHDOM or Monte Carlo solvers are four to five orders of magnitude slower than one-dimensional solvers such as the Twostream. The TenStream solver is explained in detail in chapter 2.

Chapter 2

Methods to Study the Impact of Radiative Heating Rates on the Evolution of Clouds

The following chapter will present a new method to compute three-dimensional heating rates in atmospheric models, in particular high resolution numerical weather prediction models and large eddy simulations. The new method is named TenStream and extends the well-known one-dimensional Twostream theory to ten streams in three dimensions. The first part of this chapter will focus on the method and its comparison to benchmark simulations. The description of the method in the upcoming section 2.1 resembles the published version in Jakub and Mayer [2015] except of some trimming in the introductory part and the outlook.

The second part, section 2.2 follows the work published in Jakub and Mayer [2016] and discusses various aspects of the technical challenges when coupling the TenStream solver to a Large-Eddy-Simulation. We compare the runtime of the TenStream solver to one-dimensional radiative transfer and specifically discuss the choice of matrix preconditioners and the associated parallel weak- and strong-scaling efficiency.

2.1 A Three-Dimensional Parallel Radiative Transfer Model for Atmospheric Heating Rates for use in Cloud Resolving Models — the TenStream solver[1]

As mentioned earlier, currently available 3D RT solvers (Monte Carlo based (e.g. Mayer [2009]) or SHDOM [Evans, 1998]) are cumbersome to use because of their extraordinary computational burden. The purpose of this work is to develop a new, three-dimensional solver, which is able to compute realistic atmospheric heating rates, yet is fast enough to run in high resolution models. In Section 2.1.1 we will introduce the basic concept of a finite volume solver, in close analogy to the well

[1] Jakub and Mayer [2015], doi:10.1016/j.jqsrt.2015.05.003

established Twostream approximation Meador and Weaver [1980] and expand it to 10-streams in three dimensions. The new algorithm will then be compared to a 3D Monte Carlo solver for a variety of cloud scenarios with varying horizontal resolution and meteorological situations in section 2.1.2.
Section 2.1.3 will discuss the advantages and drawbacks of the developed method and its applicability for NWP models and large eddy simulations.

2.1.1 Method

The general outline of any finite volume algorithm such as the Twostream solver is straightforward. The first step is to solve the radiative transfer inside a single volume (horizontal layer in 1D, box in 3D). As a second step, the individual volumes have to be coupled to one another. In the following we will revisit the Twostream formulation and note the key components. Twostream solutions give the up- and downward fluxes $E_\uparrow$ and $E_\downarrow$ for a horizontally infinite and homogeneous layer and can be written as:

$$\begin{aligned} E_\uparrow^T &= \gamma_1 E_\uparrow^B + \gamma_2 E_\downarrow^T + \beta_0 S^T \\ E_\downarrow^B &= \gamma_2 E_\uparrow^B + \gamma_1 E_\downarrow^T + \beta_1 S^T \end{aligned} \tag{2.1}$$

where the superscript ^{T} and ^{B} denote the upper and lower bound of the layer.

The source term S in the solar spectral region is the direct irradiance which is calculated as follows:

$$S^B = \alpha\, S^T \tag{2.2}$$

α is the transmission of direct irradiance which can be expressed by Lambert-Beer's law:

$$\alpha = \exp\left(-\int k_{ext}\, ds\right) = \exp\left(-\frac{\tau}{\mu_0}\right) \tag{2.3}$$

where k_{ext} is the extinction coefficient, τ is the vertical optical thickness of the layer, and μ_0 the cosine of the solar zenith angle.

The individual transport coefficients in a Twostream solver describe the following processes:

- Direct radiation (S) is the part of the radiation which has not yet interacted with the medium; its transmission is described by (α).
- Direct radiation, after scattering, is the source of diffuse radiation, either scattered into the upper (β_0) or the lower (β_1) hemisphere.
- Diffuse radiation (E) is subject to absorption and scattering. The coefficients γ_1 and γ_2 describe diffuse transmission and reflection.

The transport coefficients β and γ are obtained by solving a simplified radiative transfer equation for a homogeneous layer. E.g. the delta-Eddington approximation assumes that the radiance is a linear function of the polar angle. Here we don't look into the details of the derivation of Twostream solutions. Interested readers may

refer to Meador and Weaver [1980].
For calculations in a vertically inhomogeneous atmosphere, the atmosphere is usually split into a number of homogeneous layers. For each of those homogeneous layers, the coefficients α, β, and γ are calculated as outlined above. To obtain a solution for the inhomogeneous atmosphere, the individual layers are coupled by substituting the incoming flux at the upper or lower boundaries by the outgoing fluxes at the adjacent layers. This results in an equation system which, considering boundary conditions at the lowermost and uppermost levels, allows for the solution of a vertically inhomogeneous atmosphere (details in section 2.1.1.4).

2.1.1.1 Concept for a new solver

Two streams only allow for energy transport along a single axis. Consequently, two are certainly not enough for a reasonable 3D approximation. Well, how many streams are needed and how many can we afford computationally? To answer this question, we developed a flexible framework for studying a variety of discretizations.

The simplest discretization for the diffuse radiation on a rectangular grid would be six streams, namely two in the vertical, as it is the case in Twostream solvers ($E_\uparrow$,$E_\downarrow$), and additionally two streams for each horizontal direction. Additionally, direct radiation necessitates three streams, one in each direction (x,y,z), which we will denote as $S_\downarrow$, $S_\rightarrow$ and $S_\searrow$. It does, however, turn out that a single diffuse stream for each sideward direction fails to describe the 3D radiation field adequately which shows in only marginally improved results regarding atmospheric heating rates. The choice on the number of streams will always be a compromise between accuracy and speed — as many as needed but as few as possible. Section 2.1.2 discusses why we recommend to use ten streams for the diffuse and three streams for direct radiation for the use in LES or NWP models.

Setting up the equation system to couple individual homogeneous grid boxes for a TenStream system is analogous to the Twostream approach. However, our approach in calculating the transport coefficients differs significantly. Instead of an approximate analytic expression, we use Monte Carlo methods Mayer [2009] to compute the transport coefficients (see section 2.1.1.3). The advantage of the Monte Carlo method is that it does not need any simplifying assumptions and that the tedious integration of the radiative transfer equation over the grid box volume is avoided. Since Monte Carlo is computationally expensive, the coefficients are precomputed for a large set of atmospheric conditions and stored in a lookup-table.

2.1.1.2 Discretization of streams

This section defines the explicit discretization of the ten diffuse and three direct streams. For illustration purposes we present two dimensions and omit the third one (North-South) for reasons of clarity, which reduces the number of streams from ten to six diffuse streams and from three to two direct streams. Adding the third dimension is trivial.

In analogy to the Twostream formalism in eq. (2.1), we can write the transport

of incoming (right-hand side) to outgoing (left-hand side) radiation as follows:

$$\begin{bmatrix} E^{T}_{\uparrow} \\ E^{B}_{\downarrow} \\ E^{L}_{\swarrow} \\ E^{R}_{\searrow} \\ E^{L}_{\nwarrow} \\ E^{R}_{\nearrow} \\ S^{B}_{\downarrow} \\ S^{R}_{\rightarrow} \end{bmatrix} = \begin{bmatrix} \gamma_1 & \gamma_2 & \gamma_3 & \gamma_3 & \gamma_4 & \gamma_4 & \beta_{01} & \beta_{11} \\ \gamma_2 & \gamma_1 & \gamma_4 & \gamma_4 & \gamma_3 & \gamma_3 & \beta_{02} & \beta_{12} \\ \gamma_5 & \gamma_6 & \gamma_7 & \gamma_8 & \gamma_9 & \gamma_{10} & \beta_{03} & \beta_{13} \\ \gamma_5 & \gamma_6 & \gamma_8 & \gamma_7 & \gamma_{10} & \gamma_9 & \beta_{04} & \beta_{14} \\ \gamma_6 & \gamma_5 & \gamma_9 & \gamma_{10} & \gamma_7 & \gamma_8 & \beta_{05} & \beta_{15} \\ \gamma_6 & \gamma_5 & \gamma_{10} & \gamma_9 & \gamma_8 & \gamma_7 & \beta_{06} & \beta_{16} \\ 0 & 0 & 0 & 0 & 0 & 0 & \alpha_{00} & \alpha_{10} \\ 0 & 0 & 0 & 0 & 0 & 0 & \alpha_{01} & \alpha_{11} \end{bmatrix} \begin{bmatrix} E^{B}_{\uparrow} \\ E^{T}_{\downarrow} \\ E^{R}_{\swarrow} \\ E^{L}_{\searrow} \\ E^{R}_{\nwarrow} \\ E^{L}_{\nearrow} \\ S^{T}_{\downarrow} \\ S^{L}_{\rightarrow} \end{bmatrix} \tag{2.4}$$

The lower two rows of eq. (2.4), i.e. the α-coefficients, specify the transport of direct radiation through the box (see eq. (2.2) for reference to the Twostream formalism). As fig. 2.1a shows, $S^{T}_{\downarrow}$ is the incoming solar radiation through the top of the box and $S^{L}_{\rightarrow}$ through the side wall. For direct radiation the superscripts ^{L}and ^{R} are chosen for the sun shining from the left. If the sun is positioned on the opposite side, they may be switched. The α-coefficients are still calculated by Lambert-Beer's Law but the integral in eq. (2.2) is not a constant expression anymore. It rather has to be integrated over all possible paths a photon can travel through the box. Some coefficients may be zero, depending on the geometry. For example, α_{11} is zero unless the solar zenith angle is so high that direct radiation may enter at the left side and exit the box on the right.

The diffuse streams $E_{\uparrow}$ and $E_{\downarrow}$ are analogous to the Twostream formulation defined as the flux through the top and bottom of the box. Figure 2.1b also shows the two streams on each side wall, where $E_{\searrow}$ is the flux through the side wall into the lower hemisphere, whereas $E_{\nearrow}$ corresponds to the upper hemisphere. In the vertical, the superscripts ^{T}and ^{B} again denote the top and bottom of the box. In the horizontal direction, the left side is denoted with superscript ^{L} and the right side with ^{R}. The β-coefficients describe the conversion from direct to diffuse radiation, i.e. how direct light is scattered into one of the diffuse streams. Finally, the γ-coefficients characterize the energy transport between the various diffuse streams. Note that γ-coefficients in eq. (2.4) occur more than once. The reason for these symmetries are streams at opposing sides which are symmetric. This is already the case in the Twostream approximation for the up- and downward streams, and of course also holds true for sideward streams.

2.1.1.3 Calculating the Transport Coefficients

An analytic solution of a simplified radiative transfer equation, in analogy to the Twostream method would be rather tedious, if possible at all. And even if possible, it would only be approximate. We therefore decided to use a Monte Carlo method to derive the transport coefficients (eq. (2.4)) which is straightforward to implement and more accurate than any analytical approximation.
The principal idea of Monte Carlo radiative transfer is to not explicitly solve the radiative transfer equation, but rather to model the underlying processes i.e. absorption and scattering. Statistical sampling of individual photon paths yields the

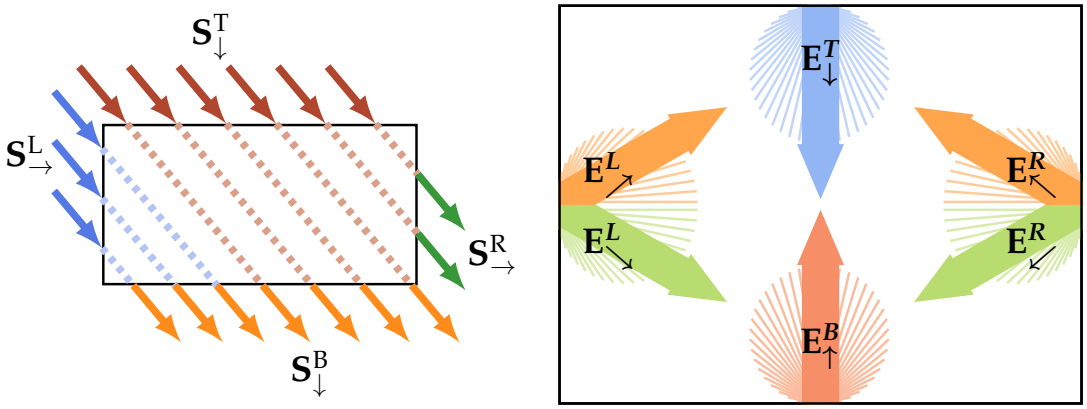

(a) direct streams (θ=40°) **(b)** diffuse streams

Figure 2.1: Discretization for three direct and ten diffuse streams (two and six in 2D respectively). Figure 2.1a shows incoming and outgoing direct radiation, traveling (dashed) through the box ($\boldsymbol{\alpha}$). In case that direct radiation is scattered (not depicted), radiation will be transferred to diffuse streams ($\boldsymbol{\beta}$). Figure 2.1b shows incoming diffuse radiation (γ). Diffuse outgoing streams (not depicted) are identical to incoming streams but with reversed directions.

desired solution to the radiative transfer equation, in particular the transport coefficients. The beauty of Monte Carlo methods lies in their flexibility and ease of use, which allows us to freely play around with a variety of streams. Also, there are no restrictions to geometry: triangular or hexagonal grids (as used by modern NWP models) may be implemented as easily as a rectangular grid.
For example, to calculate the direct radiation transport coefficients α_{00} and α_{01}, we have initialized photon packets uniformly distributed on the top of the box while the direction is fixed with the solar zenith and azimuth angle. After tracing a photon through the box and given that it is not scattered or absorbed, it ends up in either $S^{B}_{\downarrow}$ or $S^{R}_{\rightarrow}$ and consequently accounts for α_{00} or α_{01}. On the other hand, if the photon is scattered, it contributes to one of the diffuse streams and hence adds to a β-coefficient.
The same procedure is used for the diffuse γ-coefficients. For example, photons for the $E_{\downarrow}$ stream are initialized at the box top, assuming isotropic radiance that is uniformly distributed in space and the angles are chosen according to a lambertian surface.

At this point we should review the approximations just introduced. While the Monte Carlo methods are not using simplifications for the sub-grid radiative transfer, we do however limit the resolution of the radiance field spatially as well as angularly through assumptions made on the boundaries of a box. On one hand, the size of the boxes, i.e. the resolution of the grid determines the spatial resolution. On the other hand, we need to make an assumption about the angular distribution of incoming light and hence, the count and orientation of the streams define the angular resolution.
This study uses a simple forward Monte Carlo model that calculates the transport coefficients for one homogeneous box. Without looking into the details of the model, we should still briefly mention its key features. If not noted otherwise,

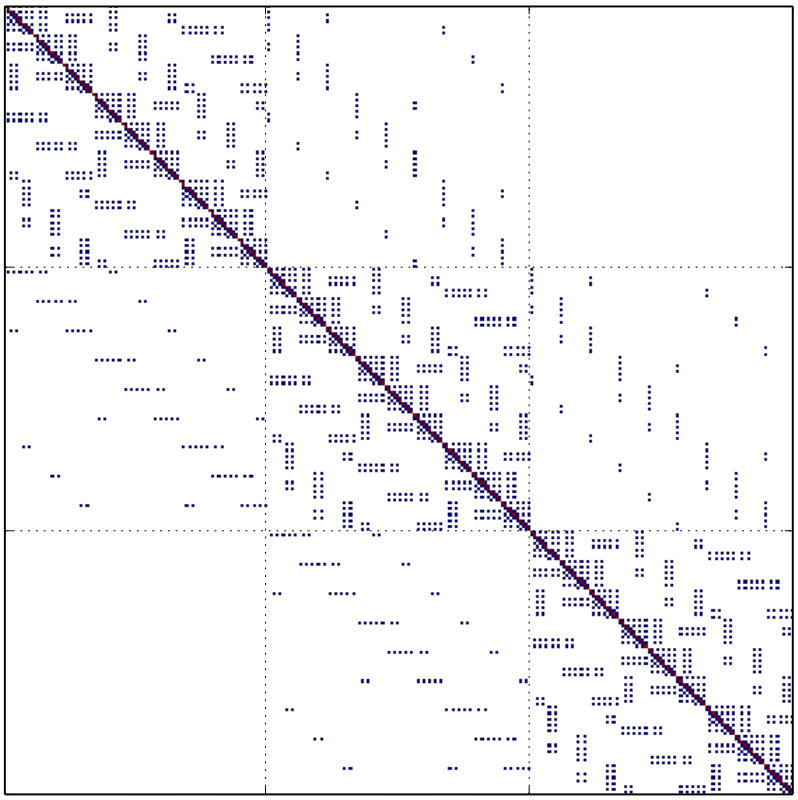

Figure 2.2: Nonzero pattern of a diffuse TenStream matrix with grid size being $3 \times 3 \times 3$. At a closer look, the 3 by 3 by 3 by 10 structure is evident.

please refer to Mayer [2009] for a detailed explanation. For cloud scattering we used the Henyey-Greenstein phase function Henyey and Greenstein [1941]. Absorption is accounted for by reducing the photon weight. The integration is performed until the absolute standard deviation is less than 10^{-3} and the relative standard deviation is smaller than 10%. To speed up the calculation in the case of high optical thicknesses we used Russian roulette as proposed by Iwabuchi [2006].

This calculation is accurate but too slow to be run online for every box, hence we pre-computed the coefficients and saved them in a lookup table. The dimensions of the look-up table are the box size and its optical properties, namely the scattering and absorption coefficient and the asymmetry parameter of the phase function. In addition, the coefficients for the direct radiation, α and β, depend on the solar zenith and azimuth angles.

2.1.1.4 Coupling boxes and solving the matrix equation

When the energy flow is described inside each box, the next step is to couple the individual boxes. The incoming flux at the upper boundary $E^T_{\downarrow}$ of one box equals the outgoing flux $E^B_{\downarrow}$ of the box above. The flux leaving one box to the right $E^R_{\searrow}$ enters the next box from the left $E^L_{\searrow}$. Substituting the expressions results in a set of coupled linear equations.

In order to solve this set of equations, one needs to know the boundary condi-

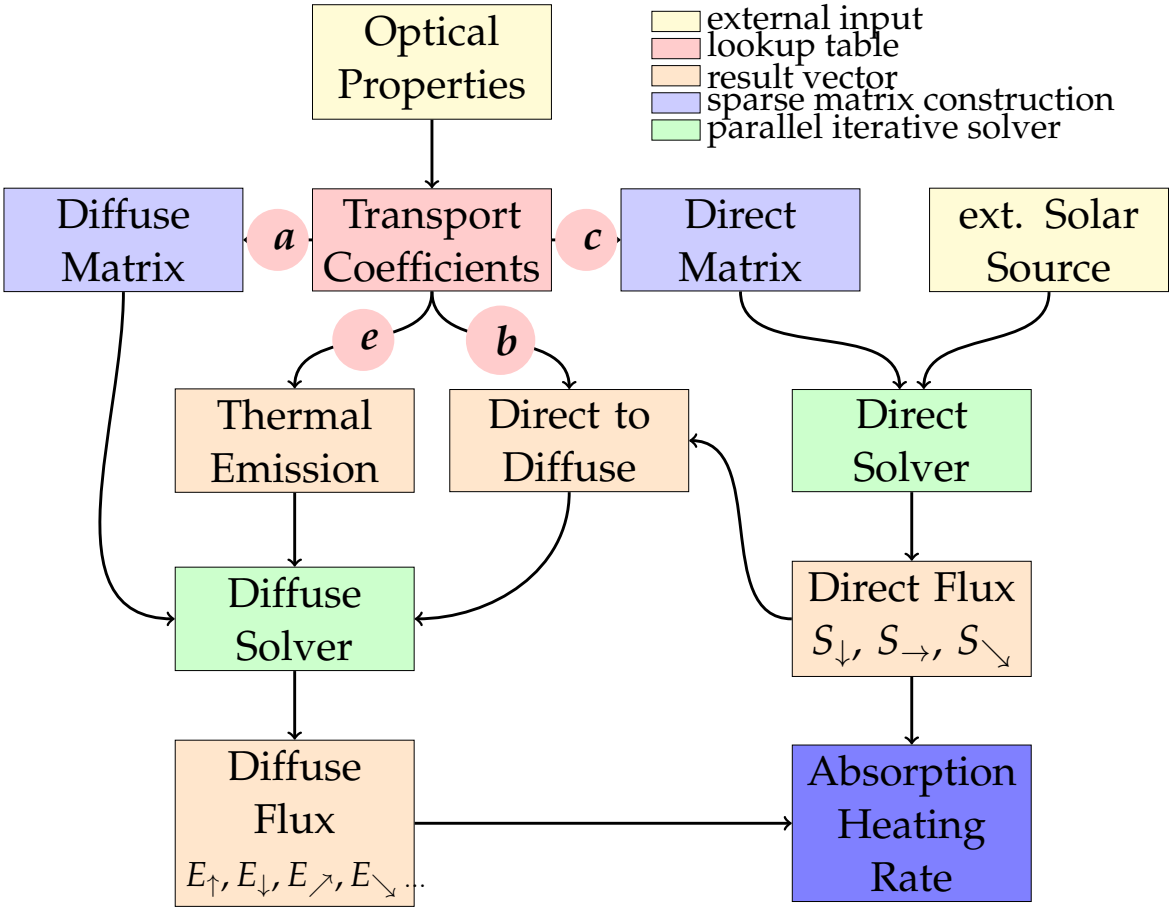

Figure 2.3: Flowchart for the conceptual steps of the solver. Input to the algorithm are optical properties and extraterrestrial incoming solar radiation. Output are the direct and diffuse fluxes as well as the absorption for each cell. Detailed description about the individual steps is given in section 2.1.1.5

tions. In the case of radiative transfer in the solar spectral region, this is the surface albedo and the extraterrestrial incoming radiation at top of atmosphere. In the one-dimensional case described for the Twostream solver, the matrix can furthermore be written in a compact banded matrix with five diagonal entries, which can be solved efficiently with any numerical linear algebra package (e.g. LAPACK).

However, in the case of 3D solvers, it is generally not possible to order the matrix rows in a way that the matrix reduces to a low bandwidth, banded structure. Due to the horizontal coupling, the matrix is of size $N_{streams} \times N_{levels} \times N_x \times N_y$ where N_x and N_y are the numbers of grid boxes in the horizontal directions — a huge, yet sparse matrix (most entries are zero, see fig. 2.2).

Efficiently solving big sparse matrices on parallel machines is a demanding undertaking on its own. Numerous algorithms exist to solve such systems, but it is practically not possible to estimate in advance which method is suited best. This is where the parallel linear algebra library PETSc Balay et al. [2014] comes into play. Using the PETSc Toolkit allowed a rapid development of the parallel algorithm and also allows the testing and comparison of a multitude of matrix solvers.

2.1.1.5 All the way to heating rates

With all the components in place, let us briefly summarize the outline of the RT model and the final steps to derive atmospheric heating rates. As shown in fig. 2.3, the input that needs to be provided externally are the optical properties of each grid box (absorption and scattering coefficient and asymmetry parameter) as well as the extraterrestrial solar source. It is clear from eq. (2.4) that direct radiation is not a function of the diffuse terms and can be solved prior to the diffuse radiation. In order to calculate the direct radiation we may set up the direct sub-matrix which consists only of α-coefficients. The α-coefficients are retrieved from the lookup table. Using the direct radiation together with β-coefficients, we set up the source term for the diffuse radiation. Assembling the diffuse matrix and solving it results in diffuse fluxes. Using Gauss's theorem, we calculate the absorbed power $\mathrm{d}Q$ (divergence of radiation) inside each box by integrating the energy flux density over the surface of the box:

$$\frac{\mathrm{d}\boldsymbol{Q}}{\mathrm{d}t} = \iiint_V \boldsymbol{\nabla}\vec{E}\, dV = \oiint_S \vec{E}\cdot\vec{n}\, dS \tag{2.5}$$

In our case the energy flux through the box's surface is the sum of the net flux for all streams.

The heating rate is simply

$$\frac{\mathrm{d}\boldsymbol{T}}{\mathrm{d}t} = \frac{1}{c_p\rho}\cdot\frac{\mathrm{d}\boldsymbol{Q}}{\mathrm{d}t} \tag{2.6}$$

, where ρ is the air density and c_p the specific heat capacity.

2.1.2 Results and Discussion

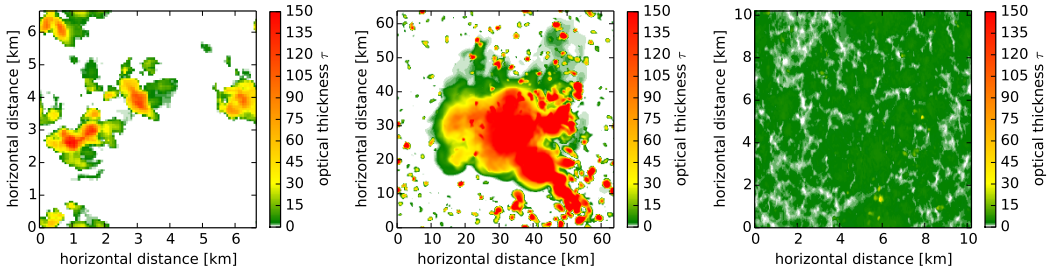

(a) I3RC **(b) Cb** **(c) astex**

Figure 2.4: Vertically integrated optical depth. Scattering and absorption optical depth spectrally integrated with correlated-k method of Kato et al. [1999]. Optical depth truncated for fig. 2.4b ($\tau_{\max} = 689$). Figure 2.4a depicts the scattered cumulus clouds with clear-sky regions in-between. Figure 2.4b shows the massive deep-convective cell, surrounded by small cumulus clouds. Lastly, fig. 2.4c shows the uniformly overcast stratus scenario.

		I3RC		**Cb**		**ASTEX**	
	θ	TwostrICA	Tenstr	TwostrICA	Tenstr	TwostrICA	Tenstr
Heating Rates in atmosphere	—	263 (-12.1)	85 (-1.2)	120 (-0.9)	65 (2.4)	100 (9.5)	75 (14.1)
	0	45 (-1.3)	16 (-0.7)	35 (-0.6)	19 (0.0)	11 (-1.0)	7 (-0.3)
	20	61 (-3.2)	20 (-0.5)	52 (-1.7)	20 (0.0)	14 (-1.4)	8 (-0.4)
	40	103 (-7.0)	23 (-0.5)	88 (-4.5)	22 (-0.1)	21 (-2.1)	12 (-0.2)
	60	176 (-12.8)	31 (-0.4)	138 (-9.3)	28 (-0.3)	40 (-1.1)	20 (2.0)
	80	389 (-17.0)	64 (1.8)	261 (-15.0)	48 (-0.2)	124 (-0.0)	33 (3.4)
Surface Heating	—	36 (6.5)	20 (-3.2)	28 (12.4)	11 (-2.4)	25 (-3.3)	14 (-12.3)
	0	20 (-2.3)	11 (-1.6)	24 (-4.3)	14 (-3.1)	10 (-0.6)	8 (-4.5)
	20	42 (-1.6)	14 (-1.7)	45 (-3.8)	15 (-3.0)	15 (-0.3)	9 (-4.1)
	40	55 (-0.1)	13 (-1.4)	66 (-2.5)	17 (-2.5)	15 (0.9)	9 (-2.4)
	60	62 (4.4)	18 (-1.0)	92 (1.1)	25 (-1.6)	16 (4.0)	11 (1.1)
	80	65 (24.2)	44 (0.4)	96 (27.6)	71 (-0.2)	18 (11.7)	10 (5.6)

Table 2.1: Relative RMSE and in parentheses the bias are given in percent for the surface heating (direct plus diffuse downward minus upward) as well as atmospheric heating rates. Two methods, namely a IPA delta eddington Twostream and the new Tenstream solver are compared to calculations of the 3D Monte-Carlo (MYSTIC) solver. Calculations for the three scenarios, **I3RC**, **Cb** and **astex** were performed for solar zenith angles $\theta = 0, 20, 40, 60, 80^\circ$ and a constant surface albedo of 5 percent.

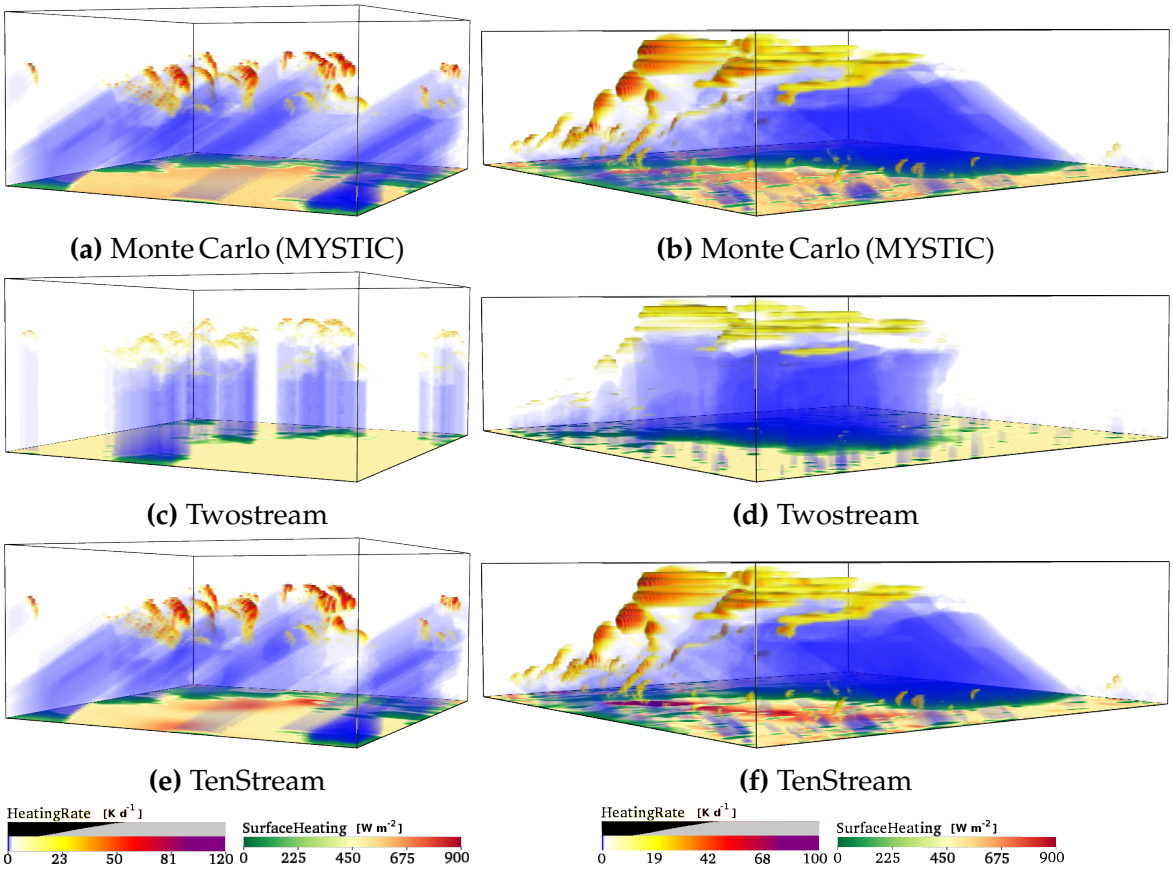

(a) Monte Carlo (MYSTIC) **(b)** Monte Carlo (MYSTIC)

(c) Twostream **(d)** Twostream

(e) TenStream **(f)** TenStream

Figure 2.5: Volume rendered perspective on atmospheric and surface heating rates (see section 2.1.2 for details). On the left side, scenario **I3RC** and on the right, scenario **Cb**. In the top row are benchmark 3D Monte Carlo MYSTIC calculations, in the mid row are delta-eddington Twostream results and in the bottom row are TenStream calculations. Surface heating is solar net radiation in $\mathrm{W\,m^{-2}}$ and atmospheric heating rate given in $\mathrm{K\,d^{-1}}$. It is clear that the ICA Twostream solver is not able reproduce the 3D RT effects, namely the cloud side illumination and the displacement of the shadows. In contrast, the TenStream solver realistically models the 3D effects. The only notable differences between the 3D MYSTIC calculations and the TenStream approximation are the local maxima in the surface heating. While the total surface heating is not biased (table 2.1), this suggests, that the TenStream is less 'diffusive' than the benchmark Monte Carlo solver.

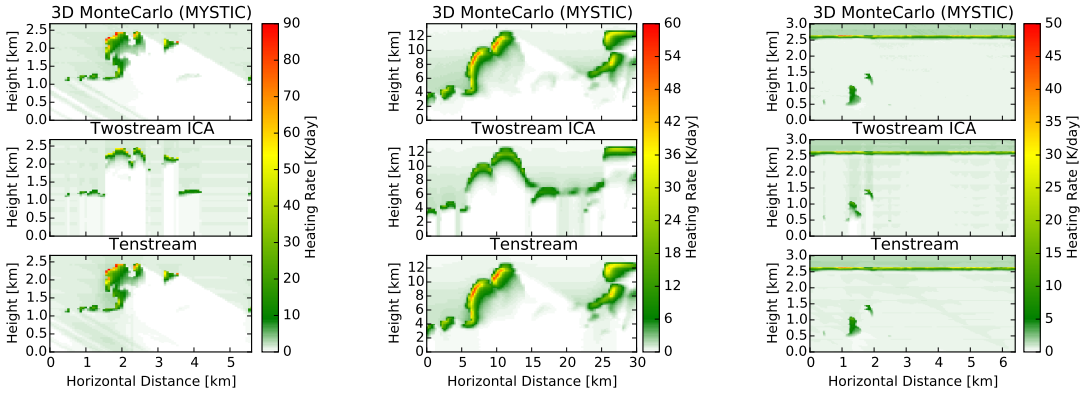

(a) I3RC (b) Cb (c) astex

Figure 2.6: Vertical cross-sections for heating rate profiles. Solar zenith angle $\theta = 60°$

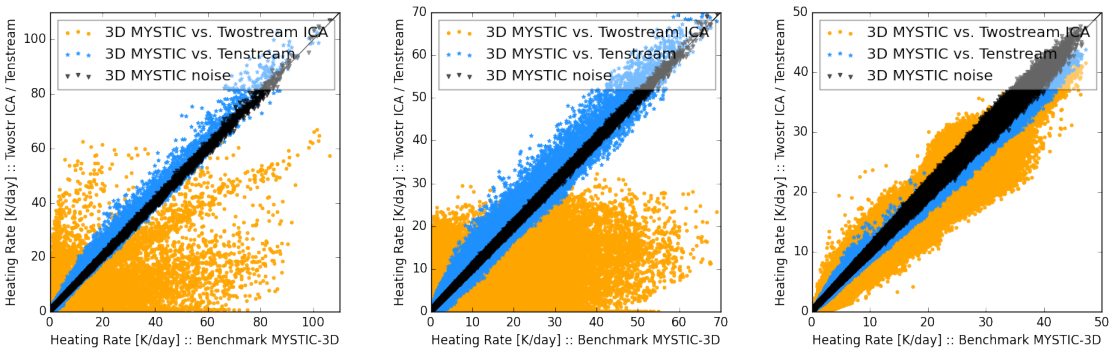

(a) I3RC (b) Cb (c) astex

Figure 2.7: Comparison of atmospheric heating rates to benchmark MYSTIC calculations. The black markers show the difference to an independent MYSTIC calculation with the same number of photons (Monte Carlo noise). The blue markers show the difference to the TenStream calculation and orange markers to an ICA Twostream calculation. Solar zenith angle $\theta = 60°$. The TenStream solver is able to reproduce the higher heating rates and also at the correct position. Due to the horizontal homogeneity in the **astex** scenario the ICA is an adequate approximation.

	I3RC	Cb	astex
Δx,Δy (m)	70	250	40
min. Δz (m)	40	200	20
domain size (km^2)	6.7×6.7	64×64	10×10
cloud type	Cu	Cb	St
cloud phase	water	water&ice	water
cloud base (km)	1.0	3	2.4
cloud top (km)	2.4	16	2.5

Table 2.2: Details on cloud scenarios that were used to demonstrate algorithm performance. Each cloud scenario is described by the horizontal resolution Δx and Δy, the minimum vertical extent of a layer Δz (grid is stretched towards top of atmosphere), the total domain size, and cloud classifications. See fig. 2.4 for the horizontal distribution of clouds.

In order to evaluate the results of the new solver, we compare the output to a full 3D Monte Carlo model, which serves as benchmark. MYSTIC (Monte Carlo code for the physically correct tracing of photons in cloudy atmospheres Mayer [2009]) has been developed as part of the radiative transfer library LibRadTran Mayer et al. [2005]. The code has been extensively validated in the Intercomparison of 3D Radiation Codes (I3RC, Cahalan et al. [2005]). To compare the performance of the new solver with the widely used independent column approximation, we also calculated heating rates column by column for the given scenarios with a delta-eddington Twostream solver, also included in LibRadTran.

As O'Hirok and Gautier [2005] noted, the ICA is expected to perform worst for vertically extended cloud fields at low sun angles. Radiative forcing is however suspected to be of most importance in shallow convective systems. For this reason we present results for both strongly and weakly forced situations and show that the algorithm performs well in both cases.

Details about the three cloud scenarios are given in table 2.2. Figures 2.4a to 2.4c show the respective vertically integrated optical depth. The '**Cb**'-scenario (fig. 2.4b) from the Goddard Cumulus Cloud Ensemble Zinner et al. [2008] includes a cumulonimbus topped with an ice anvil and surrounded by smaller convective clouds. The '**I3RC**'-scenario (fig. 2.4a) is a cumulus field from experiment-7 of the Intercomparison of 3-Dimensional Radiation Codes Cahalan et al. [2005]. The '**astex**'-scenario (fig. 2.4c) is a stratocumulus cloud field Albrecht et al. [1995] with a homogeneous stratus layer and sporadic convective cells.

We compare the surface heating (direct irradiance $S_\downarrow$ plus net diffuse irradiance $E_\downarrow - E_\uparrow$) and atmospheric heating rates. The error is given by the relative root mean square error and the relative bias:

$$\begin{aligned} rel.\ \mathbf{RMSE} &= \frac{\sqrt{\overline{(y-x)^2}}}{\bar{x}} \cdot 100\% \\ \mathbf{bias} &= \left(\frac{\bar{y}}{\bar{x}} - 1\right) \cdot 100\% \end{aligned} \tag{2.7}$$

where y is either the IPA Twostream calculation or the TenStream method. We treat

the Monte Carlo result as truth and hence x stands for the 3D MYSTIC calculation and $\bar{x}$ for its arithmetic mean.

All calculations were performed using a constant surface albedo of 5 %. Integrated solar fluxes were calculated with the correlated-k method by Kato et al. [1999]. We used 10^4 photons per pixel for the Monte Carlo calculations. The noise (standard deviation) of atmospheric heating rates is approximately 7 % in the case of **I3RC**, 4.5 % for **Cb** and 4 % for the **astex**-scenario. Likewise, for the surface heating, 3.6 %, 1.6 % and 4 %, respectively.

A qualitative look at fig. 2.5 visualizes the differences between the ICA Twostream and TenStream solver. The slanted path of the direct radiation is clearly visible, which leads to strong heating at the cloud side, to elongated and displaced shadowing and generally higher heating rates in the atmosphere.
Figure 2.6 shows a cross-section through the **I3RC**-scenario and allows a quantitative comparison between the solvers. Three dimensional RT calculations lead to higher heating rates at sunlit cloud sides than in ICA calculations. Figure 2.7a not only shows that the TenStream solver is able to produce the higher heating rates, but also that the spatial correlation is better than in the Twostream case. Furthermore, the TenStream solver considerably reduces the RMSE for all scenarios independent of solar zenith angle (see table 2.1).

Regarding the surface heating, the performance of the algorithm deteriorates for large solar zenith angles. This is mainly caused by numerical diffusion. Figure 2.8 shows the difference in downwelling radiation between a Monte Carlo and a TenStream calculation. Note that numerical diffusion of direct radiation leads to a smoothing of the cloud shadow. Obviously, the longer the shadow *travels* through the atmosphere, the bigger the diffusion. A possible solution is to use more streams for the spatial discretization for the direct radiation. However, considering that numerical diffusion has the strongest impact for long "ray-paths" i.e. large solar zenith angles, we have to keep in mind that surface heating is weakest in these cases. I therefore think that the use of more direct streams is not required.

Concerning the number of diffuse streams, we stated earlier in section 2.1.1.1 that six streams led only to minor improvements in atmospheric heating rates. The vertical splitting of sideward diffuse radiation significantly improved the results. While we do not have a straightforward explanation as to why it is beneficial to have a preferential vertical discretization We may certainly hypothesize that the atmosphere has significantly stronger gradients in the vertical than in the horizontal. This is especially true for thermal radiative transfer calculations where horizontal temperature gradients are small and level horizontal energy transfer does therefore not change the results. A vertical gradient however does. At the same time, it is clear from e.g. fig. 2.5 that ten streams still does not yet capture the full three-dimensional radiance field. However, a sensitivity study showed, that alone the use of the Henyey-Greenstein phase function instead of more accurate Mie-tables introduces errors in heating rates of about 10 %. If we consider that there are additional uncertainties in ice particle shapes and aerosol properties we may argue that relative errors of 10 % to 20 % are tolerable. We therefore argue that the TenStream solver is a reasonable tradeoff between accuracy and speed for the application of calculating atmospheric heating rates.

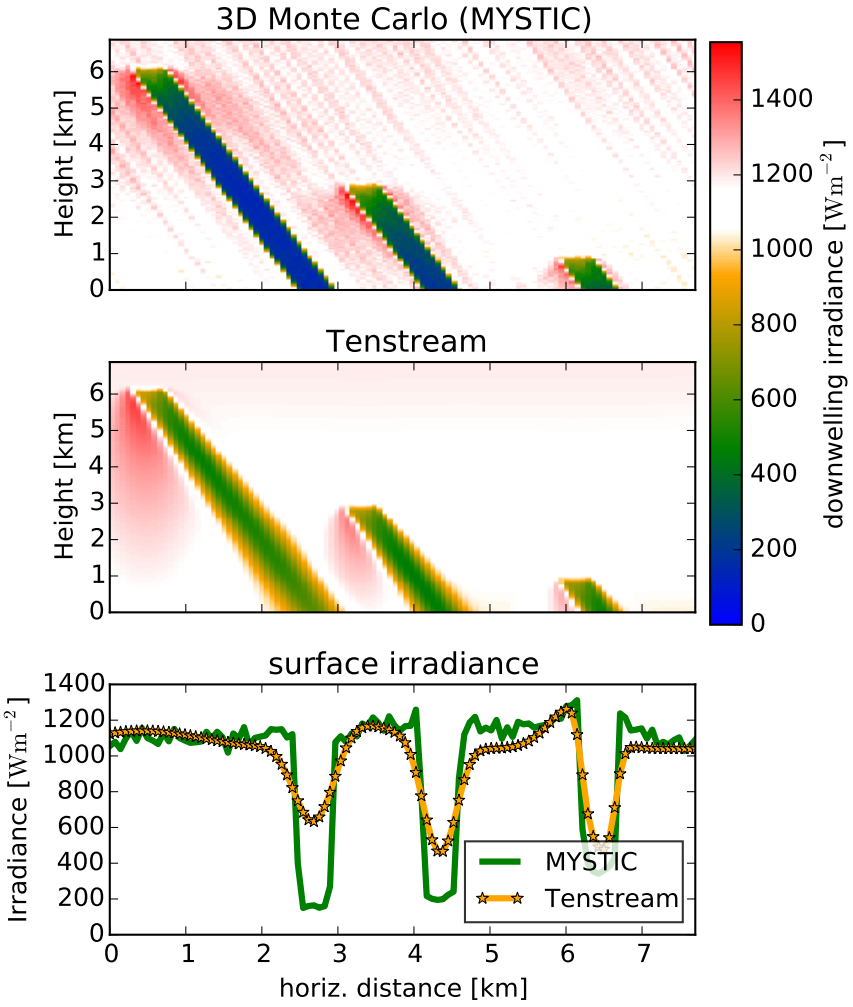

Figure 2.8: Downward radiation (direct plus diffuse downward) for three rectangular cubic clouds at different heights. 3D MonteCarlo (MYSTIC) calculation at top, Tenstream in the center, and below, the corresponding surface irradiance. Solar zenith angle $\theta = 20°$. Numerical diffusion in the TenStream solver results in smoothed shadows.

Computational speed One important consideration is the computational speed of the new solver. The major part of the algorithm runtime is spent solving the sparse matrix equation. Big sparse matrices are usually solved with iterative methods and the time needed to converge highly depends on the choice of matrix preconditioning and on which solver is used. The PETSc library allows the testing of a variety of different solvers, however such analysis is beyond the scope of this study and is therefore left for future research.

The matrix is positive definite and non-symmetric. For first test results, we used a stabilized bi-conjugate gradient iterative solver (BCGS) and an incomplete LU factorization preconditioning Balay et al. [1997]. Compared to the ICA Twostream solver (using band-matrix LAPACK routines), the TenStream solver needed approximately 15 times longer. This value may decrease by using better matrix preconditioning and general code optimizations. One specifically interesting aspect in an atmospheric model is the reuse of the last solver call to supply the initial guess for the iterative solver which may significantly speed up the convergence. An increase by a factor of 15 for the radiative transfer calculations would typically increase the total runtime of an atmospheric model by roughly a factor of three. While this may prohibit the operational use on todays computers, it certainly allows for extensive experimental studies on cloud-radiation interactions. The TenStream solver presents a good approximation to the benchmark results, yet is orders of magnitude faster than Monte Carlo methods if the same accuracy is demanded.

2.1.3 Summary and Conclusions

We presented a methodology to extend the one dimensional Twostream theory to N-streams in three dimensions. The use of Monte Carlo methods to derive the transport coefficients allows the development of radiative transfer codes for any grid geometries, which was a special concern in perspective to the irregular grid of the new ICON-Model Dipankar et al. [2015]. Surface flux and atmospheric heating rates were compared to ICA and full 3D Monte Carlo benchmark results. The algorithm outperforms the ICA solver in all of the studied scenarios.

The TenStream solver, compared to the ICA, considerably reduces the error. In the case of the solar zenith angle $\theta = 60^\circ$ the RMSE of atmospheric heating rates is reduced from 171% to 31% for the **I3RC** scenario. Similarly, for the **Cb** scenario the error is reduced from 158% to 30%. The TenStream solver therefore furnishes a sound parametrization to drive high resolution models with realistic radiative heating rates.

Earlier studies, which used 3D Monte Carlo radiative transfer calculations to drive the model OHirok et al. [2005], Petters [2009] were limited because of the overwhelming computational complexity: computation times of full 3D RT models require three orders of magnitude more time than Twostream solvers. In contrast, the TenStream solver yields realistic heating rates while increasing the computational cost only by a factor of 15. A detailed analysis of the runtime characteristics, when coupled to a Large-Eddy-Simulation, will be given in section 2.2.

2.2 Three-Dimensional Radiative Transfer in Large-Eddy Simulations — Experiences coupling the TenStream solver to the UCLA–LES [2]

The following section is based on the publication Jakub and Mayer [2016] and describes the necessary steps to couple the TenStream solver to the Large-Eddy-Simulation UCLA–LES.

While radiative transfer is probably the best understood physical process in atmospheric models it is extraordinarily expensive (computationally) to use fully three dimensional radiative transfer solvers in LES models.

One reason for the computational complexity involved in radiative transfer calculations is the fact that solvers are not only called once per time step but the radiative transfer has to be integrated over the solar and thermal spectral ranges. A canonical approach for the spectral integration are so called "correlated-k" approximations [Fu and Liou, 1992, Mlawer et al., 1997] where instead of even more expensive line-by-line calculations, the spectral integration is done with typically one to two hundred spectral bands.

However, even when using simplistic 1D radiative transfer solvers and correlated-k methods for the spectral integration the computation of radiative heating rates is very demanding. As a consequence, radiation is usually not calculated at each time step but rather updated infrequently. This is problematic, in particular in the presence of rapidly changing clouds. Further strategies are needed to render the radiative transfer calculations computationally feasible.

One such strategy was proposed by Pincus and Stevens [2009] who state that thinning out the calling frequency temporally is equivalent to a sparse sampling of spectral intervals. They proposed not to calculate all spectral bands at each and every time step but rather to pick one spectral band randomly. The error that is introduced by the random sampling is assumed to be unbiased and uncorrelated in space and time and should not change the overall course of the simulation. Their algorithm is known as Monte-Carlo-Spectral-Integration and is implemented in the UCLA–LES. For each time step and for each vertical column, a spectral band is chosen randomly. This has important consequences for the application of a 3D solver where every column is coupled to its neighbors. Calculating a particular spectral-band in one column and a different one in the neighboring column would erroneously imply that the light changes its frequency going from column to column. Instead, in the case of a 3D solver, we need to use one spectral band for the entire domain. Hence, in order to couple the TenStream solver to the UCLA–LES we need to revisit the Monte-Carlo-Spectral-Integration and check if it is still valid if used with three dimensional solvers.

In this paper we document the steps which were taken to couple the TenStream solver to the UCLA–LES which permits us to drive atmospheric simulations with realistic 3D radiative heating rates.

[2] Jakub and Mayer [2016],doi:10.5194/gmd-9-1413-2016

Section 2.2.1 introduces the UCLA–LES model and briefly recapitulates the technical aspects of the TenStream solver. In section 2.2.1.3 follows a description of two choices of matrix solvers and preconditioners which primarily determine the performance of the TenStream solver.

In section 2.2.2 we repeated simulations according to the "Second Dynamics and Chemistry of Marine Stratocumulus field study " (DYCOMS II) to check the validity of the Monte-Carlo-Spectral-Integration. Section 2.2.3 presents an analysis of the weak- and strong-scaling behavior of the TenStream solver and section 2.2.4 discusses the applicability of the model setup for extended cloud-radiation interaction studies.

2.2.1 Description of models and core components

2.2.1.1 LES model

The LES that we coupled the TenStream solver to is the UCLA–LES model. A description and details of the LES model can be found in Stevens et al. [2005]. The model already supports a 1D δ-scaled four-stream solver to compute radiative heating rates. The spectral integration is performed following the correlated-k method of Fu and Liou [1992]. We should briefly mention the changes to the model code which were necessary to support a three-dimensional solver.

In the case of three dimensional radiative transfer we need to solve the entire domain for one spectral band at once. This is in contrast to one dimensional radiative transfer solvers where the heating rate $H(x, y, \lambda, z)$ is a function of the pixel (x, y), integrated over spectral bands (λ) and solved for one vertical column (z) at a time. We therefore need to rearrange the loop structures from

$$H(x, y, \lambda, z) \rightarrow H(\lambda, x, y, z)$$

so that the spectral integration over λ is the outermost loop. The fact that we couple the entire domain, and hence need to select the same spectral band for all columns is different from what Pincus and Stevens [2009] did and may weaken the validity of the Monte-Carlo-Spectral-Integration. We will discuss this in section 2.2.2. The rearrangement also changes some vectors from 1D to 3D and may thereby introduce copies or caching issues. We find that the change roughly adds a 6 % speed penalty compared to the original single column code (no code optimizations considered). In this paper, calculations are exclusively done using the modified loop structures.

2.2.1.2 TenStream RT model

The TenStream radiative transfer model is a parallel approximate solver for the full 3D radiative transfer equation [Jakub and Mayer, 2015]. In analogy to a Twostream solver, the TenStream solver computes the radiative transfer coefficients for up- and downward fluxes and additionally for sideward streams. These transfer coefficients determine the propagation of energy through one box. The coupling of individual boxes leads to a linear equation system which may be written as a sparse matrix equation which is solved using parallel iterative methods. It is difficult to predict

the performance of a specific choice of iterative solver or preconditioner beforehand. For that reason, we chose to use the "Portable, Extensible Toolkit for Scientific Computation", PETSc [Balay et al., 2014] framework which offers a wide range of pluggable iterative solvers and matrix preconditioners. Jakub and Mayer [2015] found that the average increase in runtime compared to 1D Twostream solvers is about a factor of 15. One specifically interesting detail about the use of iterative solvers in the context of fluid dynamics simulations is the fact that we can use the solution at the last time step as an initial guess and thereby speed up the convergence of the solver. Section 2.2.3 presents detailed runtime comparisons on various computer architectures and simulation scenarios.

2.2.1.3 Matrix solver

The coupling of radiative fluxes in the TenStream solver can be written as a huge but sparse matrix (i.e. most entries are zero). The TenStream matrix is positive definite (strictly diagonal dominant) and asymmetric. Equation systems with sparse matrices are usually solved using iterative methods because direct methods such as Gaussian-elimination or LU-factorization usually exceed memory limitations. The PETSc library includes several solvers and preconditioners to choose from.

Iterative solvers For three dimensional systems of partial differential equations with many degrees of freedom, iterative methods are often more efficient computationally and memory-wise. The three biggest classes in use today are Conjugate Gradient (CG), Generalized Minimal Residual Method (GMRES) and BiConjugate-Gradient methods [Saad, 2003]. Given that CG is only suitable for symmetric matrices we will focus on the latter two. In the following we will use the flexible version of GMRES [Saad, 1993] and the "stabilized version of BiConjugate-Gradient-Squared" [Van der Vorst, 1992].

Preconditioner Perhaps even more important than the selection of a suitable solver is the choice of matrix preconditioning. In order to improve the rate of convergence, we try to find a transformation for the matrix that increases the efficiency of the main iterative solver. We can use a preconditioner $\mathcal{P}$ on the initial matrix equation so that it writes:

$$\mathcal{P}\mathcal{A} \cdot x = \mathcal{P}b$$

We can easily see that if $\mathcal{P}$ is close to the inverse of $\mathcal{A}$ the left hand side operator reduces to unity and the effort to solve the system is zero. Of course we cannot cheaply find the inverse of $\mathcal{A}$ but we might find something that resembles $\mathcal{A}^{-1}$ to a certain degree. Obviously for a good cost/efficiency tradeoff the preconditioner should be computationally cheap to apply and considerably reduce the number of iterations the solver needs to converge.

This study suggests two preconditioners for the TenStream solver. We are fully aware that our choices are probably not an optimal solution but they give reasonable results.

The first setup uses a so called stabilized BiConjugate-Gradient solver with incomplete LU factorization (ILU). Direct LU factorizations tend to fill up the zero-

entries (sparsity pattern) of the matrix and quickly become exceedingly expensive memory-wise. A workaround is to only fill the preconditioner matrix until a certain threshold of filled entries are reached. A fill level factor of zero prescribes that the preconditioner matrix has the same number of non-zeros as the original matrix. The ILU preconditioner is only available sequentially and in the case of parallelized simulations, each processor applies the preconditioner independently (called "block-jacobi"). Consequently, the preconditioner can not propagate information beyond its local part and we will see in section 2.2.3 that this weakens the preconditioner for highly parallel simulations.

The second setup uses a flexible GMRES with geometric algebraic multigrid preconditioning (GAMG). Traditional iterative solvers like Gauss-Seidel or Block-Jacobi are very efficient in reducing local residuals at adjacent entries (often termed high frequency errors). This is why they are called "smoothers". However, long range (low frequency) residuals, e.g. a reflection at a distant location, are dampened only slowly. The general idea of multigrid is to solve the problem on several, coarser grids simultaneously. This way, the smoother is used optimally in the sense that on each grid representation the residual which is targeted is rather high frequency error. This coarsening is done until ultimately the problem size is small enough to solve it with direct methods. Considerable effort has been put into the development of black-box multigrid preconditioners. Black-box means in this context that the user, in this case the TenStream solver, does not have to supply the coarse grid representation. Rather, the coarse grids are constructed directly from the matrix representation. The PETSc solvers are commonly configured via command-line parameters (see listing 4.1 for ILU-preconditioning or listing 4.2 for multigrid preconditioning).

2.2.2 Monte Carlo Spectral Integration

There are two reasons why radiative transfer is so expensive computationally. On one hand, a single monochromatic calculation is already quite complex. On the other hand, radiative transfer calculations have to be integrated over a wide spectral range. Even if correlated-k methods are used, the number of radiative transfer calculations is on the order of a hundred. As a result, it becomes unacceptable to perform a full spectral integration at every dynamical time step, even with simple 1D Twostream solvers. This means that in most models, radiative transfer is performed at a lower rate than other physical processes. Pincus and Stevens [2009] proposed that instead of calculating radiative transfer spectrally dense and temporally sparse, one may sample only one spectral band at every model time step. The argument is that the error which is introduced by the coarse spectral sampling is averaged out over time and remains random and uncorrelated in space and time. As we mentioned in section 2.2.1.1, the three dimensional radiative transfer necessitates to compute the entire domain for one and the same spectral band instead of individual bands for each vertical column. In the following we will refer to the adapted version as uniform Monte-Carlo-Spectral-Integration. The uniform sampling relaxes the assumption that the errors are uncorrelated in space and it is therefore not clear whether it is still valid. We repeated the numerical experiment in close resemblance

to the original paper of Pincus and Stevens [2009] and examine the results to validate the applicability of the uniform Monte-Carlo-Spectral-Integration.

There, they used the model setup for the DYCOMS-II simulation (details in Stevens et al. [2005]). They show results for nocturnal simulations. In contrast, here we show results with a constant zenith angle $\theta = 45^\circ$. Radiative transfer is computed with a 1D δ-Eddington Twostream solver. The simulation is started with Monte-Carlo-Spectral-Integration and from 2.5 hours on, also calculated with the full spectral integration and the uniform Monte-Carlo-Spectral-Integration. Note, the good agreement between the full spectral sampling simulation and the one with the original Monte-Carlo-Spectral-Integration in fig. 2.9. The uniform formulation of Monte-Carlo-Spectral-Integration leads to high frequency changes in the average liquid water content (LWC). These fluctuation in LWC do however not lead to major differences in the evolution of the boundary layer clouds or turbulent kinetic energy. To put the changes in LWC into perspective, we ran the simulation again with a random perturbation on the boundary layer temperature field. The perturbation is randomly drawn from the interval between $-.5$ and .5 K. We find that the temperature perturbation induces similar differences to the flow as does the Monte-Carlo-Spectral-Integration. Furthermore, we additional ran the simulation with the δ-four-stream solver [Liou et al., 1988]. While arguably both are good radiative transfer solvers, the choice of the solver leads to bigger differences than the uniform Monte-Carlo-Spectral-Integration and even introduces a bias in the evolution of the cloud height. We therefore conclude, that while the uniform Monte-Carlo-Spectral-Integration may very well introduce considerable small scale errors, it nevertheless seems to be a viable approximation for this kind of simulations. Additionally, we repeated the same kind of experiment for several other scenarios (broken cumulus and deep convection), all confirming the applicability of the uniform Monte-Carlo-Spectral-Integration.

2.2.3 Performance Statistics

To determine the parallel scaling behavior when using an increasing number of processors, one usually conducts two experiments: First, a so called "strong-scaling" experiment where the problem size stays constant while the number of processors is gradually increased. We speak of linear strong-scaling behavior if the time needed to solve the problem is reduced proportional to the number of used processors. Secondly, a "weak-scaling" experiment where the problem size and the number of processors are increased linearly, i.e. the workload per processor is fixed. Linear weak-scaling efficiency implies that the time-to-solution remains constant.

2.2.3.1 Strong scaling

We hypothesized earlier (section 2.2.1.2) that a good initial guess for the iterative solver results in a faster convergence rate. To test this assumption we performed two strong scaling (problem size stays the same) simulations. One "clear-sky" experiment without clouds in which the difference between radiation calls is minimal and a "warm-bubble" case with a strong cloud deformation and displacement in

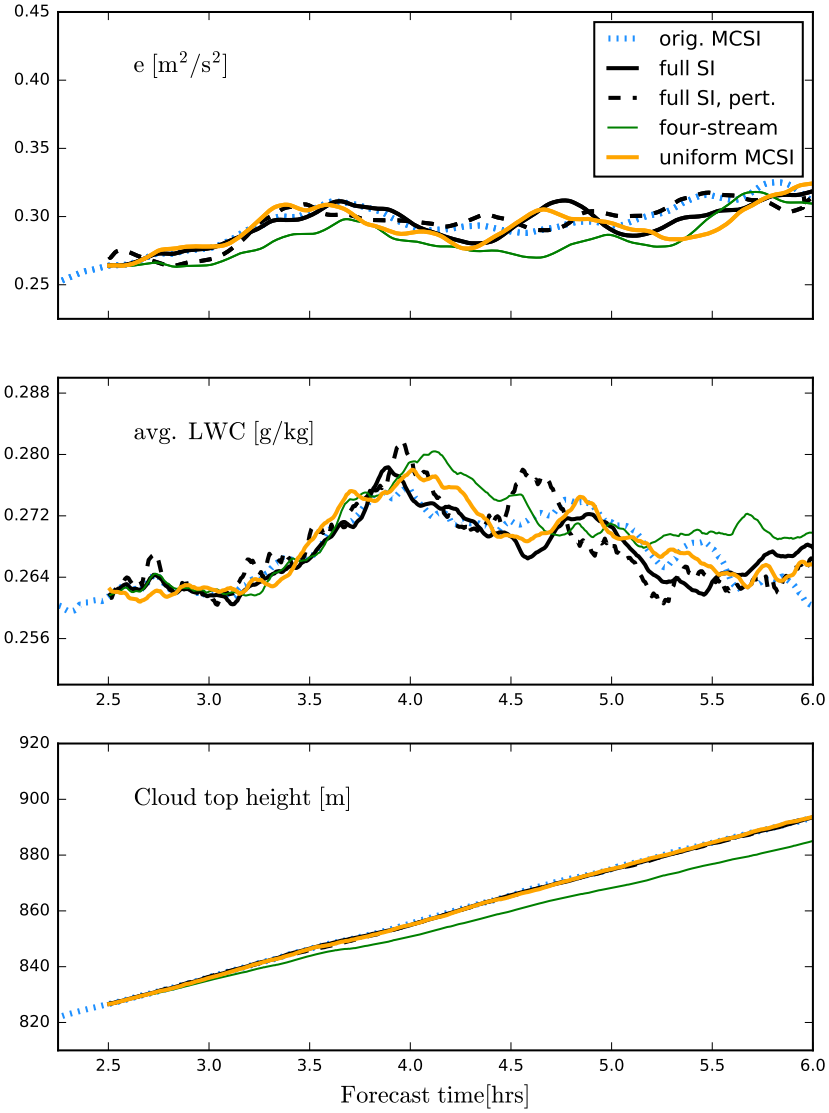

Figure 2.9: Intercomparison of the DYCOMS II simulation, once forced with the full radiation (solid line), with the original Monte-Carlo-Spectral-Integration (dotted) and with the uniform version (dashed). The dash-dotted line is a calculation with full spectral integration but with the four-stream solver instead of the Twostream solver. On the top panel, the vertically integrated turbulent kinetic energy, in the middle the mean liquid water content (conditionally sampled and weighted by physical height) and in the bottom panel the mean cloud top height.

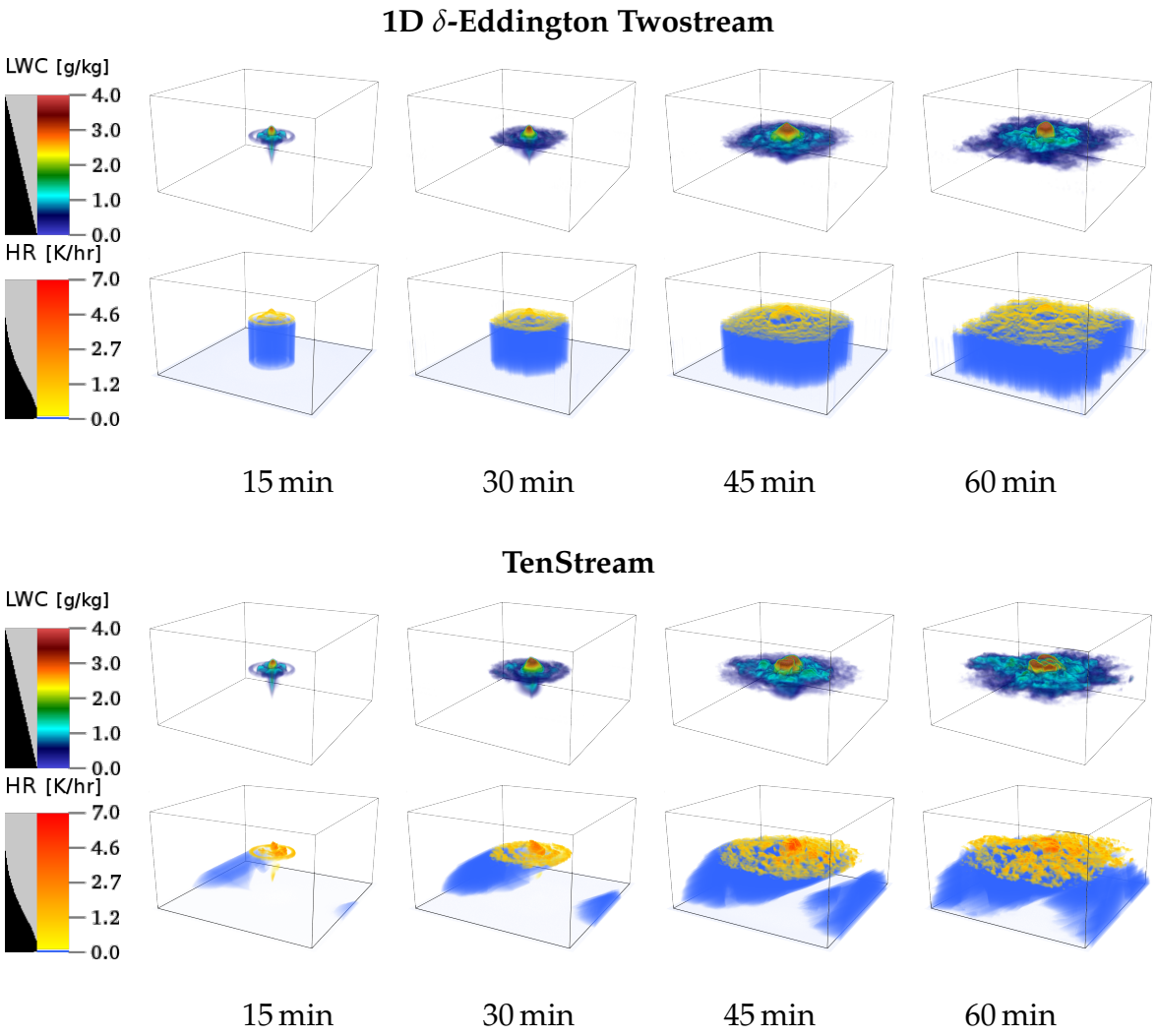

Figure 2.10: Volume rendered perspective on liquid water content and solar atmospheric heating rates of the warm-bubble experiment (initialized without horizontal wind). The two upper panels depict a simulation which was driven by 1D radiative transfer and the two lower panels show a simulation where radiative transfer is computed with the TenStream solver (solar zenith angle $\theta = 60°$; const. surface fluxes). Three-dimensional effects in atmospheric heating rates introduce anisotropy which in turn has a feedback on cloud evolution. Domain dimensions are 12.8 km $\times$ 12.8 km horizontally and 5 km vertically at a resolution of 50 m in each direction. See section 4.3 for simulation parameters. Gray bar in the legend determines the transparency of the individual colors for the volume renderer.

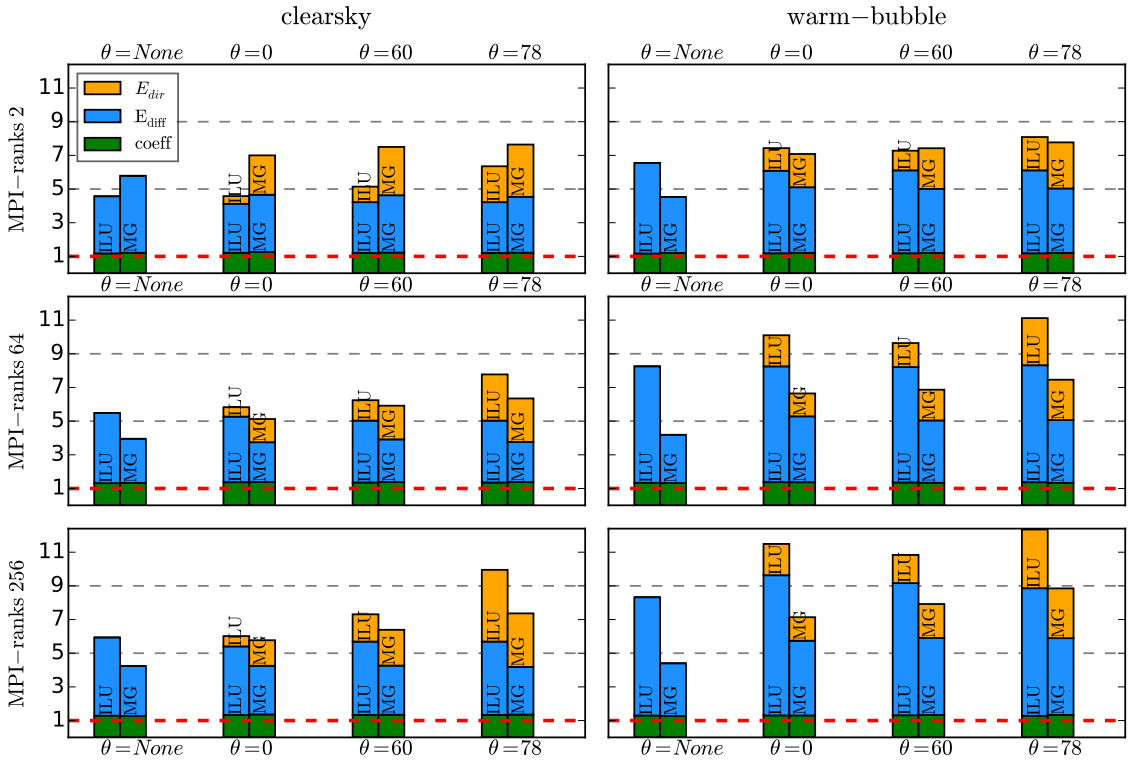

Figure 2.11: Two strong scaling tests for a clear-sky and a strongly forced scenario. Vertical axis is the increase of computational time normalized to a delta-eddington Twostream calculation (solvers only). Horizontal axis is for different solar zenith angles ($\theta = None$ means thermal only, no solar radiation). The stacked bars denoting time used for the individual components of the solver. "Coeff" meaning the time needed to retrieve and interpolate the transport coefficients. E_{diff} is the elapsed time that was used to set up the source term and solve for the diffuse radiation; the same for the direct radiation in E_{dir}. The bars are labeled with the corresponding matrix preconditioning.

between time steps. These two situations enclose what the solver may be used for and are hence the extreme cases with respect to the computational effort.

Both scenarios have principally the same setup with a domain length of 10 km at a horizontal resolution of 100 m. The model domain is divided into 50 vertical layers with 70 m resolution at the surface and a vertical grid stretching of 2 %. The atmosphere is moist and neutrally stable (see section 4.3 for namelist parameters). Simulations are performed with warm cloud microphysics, a constant surface temperature, without Monte-Carlo-Spectral-Integration and a dynamic timestep of about 2 s.

Both scenarios are run forward in time for an hour for different solar zenith angles and with varying matrix solvers and preconditioners (presented in section 2.2.1.3). The difference between the first and the second simulation is the external forcing that was applied. The "clear-sky"-case is initialized with less moisture, weaker initial wind and no temperature perturbation. No clouds develop in the course of the simulation. In contrast, the second case is initialized with a saturated moisture profile, a strong wind field and a positive, bell shaped, temperature perturbation in the lower atmosphere. The temperature perturbation leads to a rising warm bubble which leads to a cloud shortly after. The initial forcing and latent heat release leads to strong updrafts up to $19\,\mathrm{m\,s^{-1}}$ while the horizontal wind with up to $15\,\mathrm{m\,s^{-1}}$ quickly displaces the cloud sidewards. This strong deformation should give an upper bound on the dissimilarity between calls to the radiation scheme and therefore reduce the quality of the initial guess. To illustrate the general behavior of the strong- and weak scaling experiments, fig. 2.10 depicts the warm bubble simulation (for the purpose of visualization without initial horizontal wind) – once driven by 1D radiative transfer and once more with the TenStream solver.

Figure 2.11 presents the increase in runtime of the TenStream solver compared to a 1D calculation. All timings are taken as a best of three and simulations were performed on the IBM Power6 "Blizzard" at DKRZ (Deutsches Klimarechenzentrum), Hamburg in SMT mode[3]. To solve for the direct and diffuse fluxes, the matrix coefficients for the radiation propagation (stored in a 6-dim look-up table) need to be determined for given local optical properties. Retrieving the transport coefficients from the look-up table and the respective linear interpolation (green bar) takes about as long as the 1D radiative transfer calculation alone and is expectedly independent of parallelization and the initial guess of the solution. For larger zenith angles, i.e. lower sun angles, the calculation of direct radiation becomes more and more expensive because of the increasing communication between processors. Note that the computational effort also increases in case of single core runs – the iterative solver needs more iterations because of its treatment of cyclic boundary conditions. The "clear-sky" simulations are computationally cheaper than the more challenging cloud producing "warm-bubble" simulations. In the former, the solver often converges in just one iteration where as in the latter, rather complex case, more iterations are needed. Note that the ILU preconditioning weakens if more processors are used. The ILU is a serial preconditioner and in the case of parallel computations, it is applied to each sub-domain independently. The ILU-preconditioner hence can not propagate information between processors.

[3]SMT – Simultaneous Multithreading (2 ranks/core)

	Ranks / Node	Cores	Memory-Bandwidth
Mistral	24	2x12@2.5 GHz	112 GB s^{-1}
Blizzard	64	4x 8@4.7 GHz	37 GB s^{-1}
Thunder	16	2x 8@2.6 GHz	76 GB s^{-1}

Table 2.3: Details on the computers used in this work. Mistral and Blizzard are Intel-Haswell and IBM Power6 supercomputers at DKRZ, Hamburg, respectively. Thunder denotes a Linux Cluster at ZMAW, Hamburg. Columns are the number of MPI ranks used per compute node, the number of sockets and cores, and the maximum memory-bandwidth per node as measured by the streams [McCalpin, 1995] benchmark.

The performance of Multi-Grid preconditioning (GAMG) is less affected by parallelization. The number of iterations until converged stays close to constant (independent of the number of processors). The GAMG preconditioning outperforms the ILU preconditioning for many-core systems whereas the setup cost of the coarse grids as well as the interpolation and restriction operators are more expensive if the problem is solved on a few cores only. In summary, we expect the increase in runtime compared to traditionally employed 1D Twostream solvers to be in the range between five to ten times.

2.2.3.2 Weak scaling

We examine the weak-scaling behavior using the earlier presented simulation (see section 2.2.3.1) but run it only for 10 min. The experiment uses multigrid preconditioning and only performs calculations in the thermal spectral range. The number of grid points is chosen to be 16 by 16 per MPI-rank ($\approx 10^5$ unknown fluxes or $\approx 10^6$ transfer coefficients per processor). The simulations were performed at three different machines/networks (see table 2.3). Please note that the simulations for Mistral (see table 2.3) do not fill up the entire nodes (24 cores) since UCLA–LES can currently only run on a number of cores which is a power of two.

Figure 2.12 presents the weak-scaling efficiency f, defined by:

$$f = \frac{t_{single\,core}}{t_{multi\,core}} \cdot 100\%$$

The scaling behavior can be separated into two regimes: the efficiency on one compute node and the efficiency of the network communication. As long as we stick to one node (section 2.2.3.2), the loss of scaling concerns the 3D TenStream solver as well as the 1D Twostream solver. Reasons for the reduced efficiency may be cache-issues, hyper-threading or memory-bus saturation. The scaling behavior for more than one node (section 2.2.3.2) shows a close to linear scaling for the 1D Twostream solver and a decrease in performance in the case of the TenStream solver. The limiting factor here is network latency and throughput.

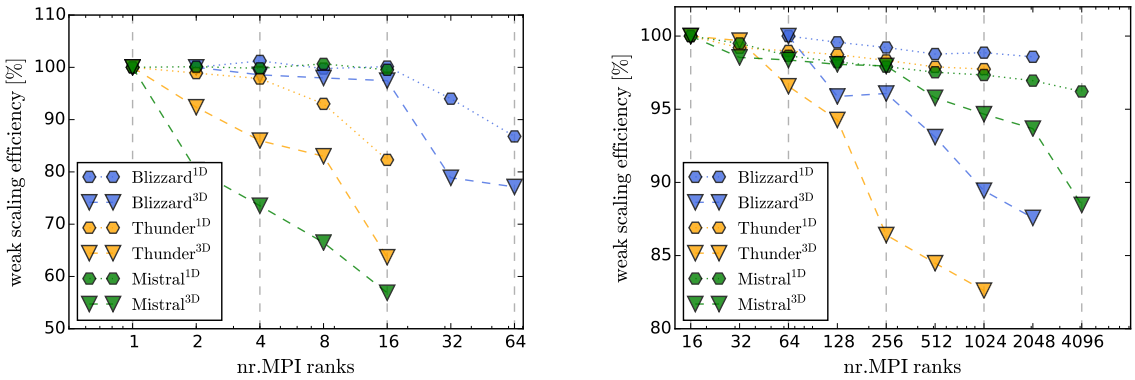

(a) single node **(b)** multiple nodes

Figure 2.12: Weak scaling efficiency running UCLA–LES with interactive radiation schemes. Experiments measure the time for the radiation solvers only (i.e. no dynamics or computation of optical properties). Timings are given as a best of 10 runs. Weak scaling efficiency is given for the TenStream solver (triangle markers) as well as for a Twostream solver (hexagonal markers). (Left) scaling behavior compared to single core computations (remaining on one compute node). (Right) Compute node parallel scaling (normalized against a single node). The individually colored lines correspond to different machines (see table 2.3 for details) and calculations once done with the δ-eddington Twostream solver (hexagons) and once with the TenStream solver (triangles).

2.2.4 Conclusions

We described the necessary steps to couple the 3D TenStream radiation solver to the UCLA–LES model. From a technical perspective, this involved the reorganization of the loop structure, i.e. first calculate the optical properties for the entire domain and then solve the radiative transfer.

It was not obvious that the Monte-Carlo-Spectral-Integration would still be valid for 3D radiative transfer. To that end, we conducted numerical experiments (DYCOMS II) in close resemblance to the work of Pincus and Stevens [2009] and find that the Monte-Carlo-Spectral-Integration holds true, even in case of horizontally coupled radiative transfer where the same spectral band is used for the entire domain.

The convergence rate of iterative solvers is highly dependent on the applied matrix-preconditioner. In this work, we tested two different matrix-preconditioners for the TenStream solver: First, an incomplete LU decomposition and secondly the algebraic multigrid-preconditioner, GAMG.We found hat the GAMG preconditioning is superior to the ILU in most cases and especially so for highly parallel simulations.

The increase in runtime is dependent on the complexity of the simulation (how much the atmosphere changes between radiation calls) and the solar zenith angle. We evaluated the performance of the TenStream solver in a weak and strong scaling experiment and presented runtime comparisons to a 1D δ-eddington Twostream

solver. The increase in runtime for the radiation calculations ranges from a factor of five up to ten. The total runtime of the LES simulation increased roughly by a factor of two to three. A only twofold increase in runtime allows extensive studies concerning the impact of three dimensional radiative heating on cloud evolution and organization.

This chapter aimed at documenting the performance and applicability of the TenStream solver in the context of high-resolution modeling. The subsequent chapter 3 will quantify the impact of three dimensional radiative heating rates on the dynamics of the model.

Chapter 3

Results on the Evolution of Clouds in the Presence of Radiative Heating

With the right tools at hand we are ready to address the questions we started with, namely if and how three dimensional radiative transfer has an influence on the evolution of clouds. In this chapter we interactively couple the TenStream solver to the UCLA–LES and examine the model behavior compared to simulations with one dimensional radiative transfer or none at all. The aim of this chapter is to disentangle the various cloud-radiative feedbacks, i.e. the influence of cloud side illumination and the differential and displaced surface shadow.

This is not the first study of its kind: Earlier studies, e.g. Schumann et al. [2002] parameterized the surface fluxes either directly beneath the cloud or shifted horizontally, accounting for the displaced cloud shadows that we find in realistic three dimensional radiative transfer. Wapler [2007] extended this approach and computed direct radiation along tilted paths (TICA, see section 1.4) through the atmosphere which allowed to consider the horizontal displacement of a cloud's shadow in a direct, interactive manner. Frame et al. [2009] applies the same idea of the TICA to high reaching cumulonimbus environments. Guan et al. [1997] examines the role of thermal radiative cooling on a small cumulus clouds. Klinger [2015] studies the impact of three dimensional effects of atmospheric heating rates on nocturnal (thermal radiation only) LES simulations. Petters [2009] examined cloud radiative interaction in the marine (strato)-cumulus regime. Interestingly, to my knowledge, he was the first one to couple a fully three-dimensional Monte Carlo model to an LES for an extended period of time. However, Petters [2009] states:

> *We emphasize both the tentativeness of this conclusion*[1] *and the need for further testing. Furthermore we suggest testing the impact of the ICA on the modeling of other cloud systems.*

It is clear that examining cloud-radiative interaction under all atmospheric conditions is a huge undertaking and can not be the goal of this thesis. Nevertheless, I think it is an interesting opportunity that, for the first time, we can run high-resolution LES with interactive three-dimensional radiation on unprecedented large domains and periods of time.

[1] Effects of three-dimensional radiative-transfer on the diurnal evolution of the Strato-Cumulus-Topped-Boundary-Layer

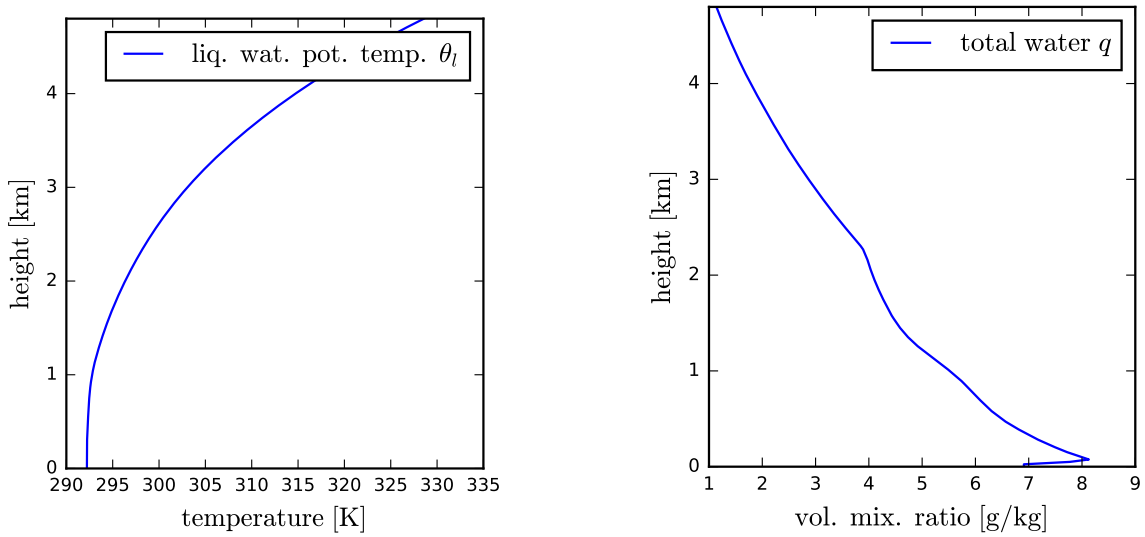

Figure 3.1: Initial vertical profiles of liquid water potential temperature (left) and the total water content (right) for the warm-bubble experiments.

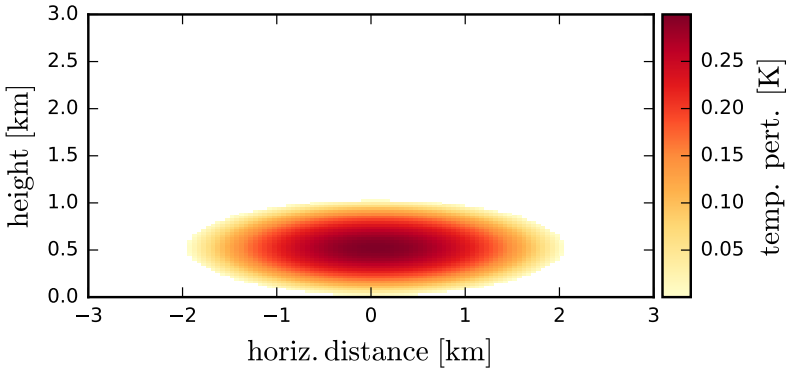

Figure 3.2: Vertical cross section of initial temperature perturbation at domain center.

The path to disentangle some aspects of the intricate relationship between radiative heating and cloud dynamics, leads us to the following experiments: first, a study on one isolated convective plume (section 3.1) — a so called warm-bubble experiment, and second, a moderately sized domain (50 km $\times$ 50 km) where we study the evolution of a shallow cumulus cloud field (section 3.2).

The general aim of this approach is that we may learn the important mechanisms of cloud-radiative interaction when we closely examine an idealized and isolated cloud. This will hopefully give us a hint on what to focus when dealing with a more involved setup with multiple clouds in larger domains.

3.1 On the Evolution of a Single Convective Cloud — A Warm-Bubble Experiment

To begin with, we start with arguably the most basic situation in which to study cloud-radiative interaction — a single, artificially forced convective plume. The simulation is initiated with a warm temperature perturbation in the lower atmosphere, the "warm-bubble", which starts an uprising motion and ultimately leads to the formation of a cloud.

The background profiles of the simulation were adopted from profiles of a long running radiative convective equilibrium state of the model with a superimposed temperature inversion. As we can see in the potential temperature in fig. 3.1, the lower atmosphere is close to neutrally stable. From 1 km on, the atmosphere becomes more and more stably stratified. There is in fact a strong inversion above 2 km and beyond.

Figure 3.2 shows the initial 0.3 K temperature perturbation that is applied at t=0 h. The simulations are performed with a horizontal resolution of $\delta x = 50\,m$ and a vertical resolution of $\delta z = 25\,m$. The total domain size is 12.8 km $\times$ 12.8 km with 256 pixels along each horizontal axis with cyclic boundary conditions and goes up to 5 km with 140 pixels in the vertical. The average time-step is approximately 2 s and the model is integrated forward in time for 1 h. The simulations use only warm micro-physics without rain. Radiative transfer is either switched off or calculated with a δ-eddington Twostream or the TenStream solver. The solar zenith angle is held constant at 40°. The radiative transfer calculations use the full correlated-k spectral integration because Monte-Carlo-Spectral-Integration is (a) not suitable when examining a single cloud in detail (because we want to interpret instant heating rates) and (b) should not be used in conjunction with an interactive surface model [Bozzo et al., 2014].

For the sake of reproducibility, the simulation input parameters are provided in the appendix (section 4.3).

This section is further subdivided considering different aspects of the cloud-radiative coupling. We expect that three-dimensional asymmetric solar radiative heating introduces an asymmetry in the evolution of the cloud. The first experiment will only consider atmospheric radiative heating while the surface fluxes for latent and sensible heat flux are prescribed.

However, it is clear that one of the first order effects of three-dimensional radiative transfer compared to one-dimensional radiative transfer is the displacement of the shadow in case of low sun. It therefore seems natural to examine the effect of asymmetric surface heating in more detail. Consequently, the subsequent second experiment in this section is to examine the influence that radiative transfer solvers have if the surface fluxes are coupled interactively.

In nature, a horizontal wind will usually shift clouds and thereby smooth the influence of surface radiative heating. For that reason, we will examine the role of a horizontal mean wind and how it interacts with radiative transfer, the surface, and the evolution of the cloud. Finally, we will close this section with a discussion and summary about the interactions between radiative heating and the evolution of one individual cumulus cloud.

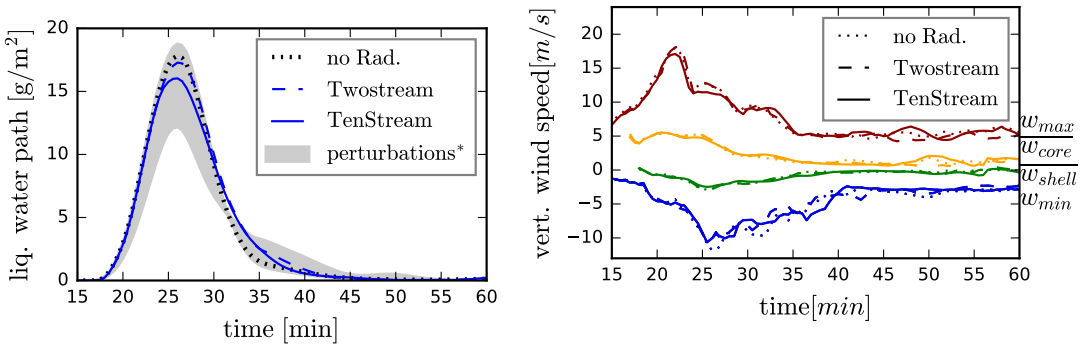

(a) liquid water path

(b) min, max, mean core and mean shell vertical wind speed (see below for definition)

Figure 3.3: Time-series for the warm-bubble experiment. Gray shaded area in liquid water path gives bounds of minimum and maximum values of five "no-radiation" simulations with varying initial temperature perturbations in the lower boundary layer ($\Delta T = .05$ K). Mean "core" and "shell" vertical velocities are conditionally sampled mean values, sampled at liquid water content, $LWC > 0$ and vertical velocity $w > .5$ or $w < .5$ respectively. Wind averages are done over a horizontal square area from -2 km to 2 km and weighted by physical height.

3.1.1 Influence of Atmospheric Radiative Heating

The above mentioned positive temperature perturbation is applied at the initialization stage of the model setup. As a consequence, the now warmer than its surrounding air is accelerated in an upward direction. At about 18 min into the simulation, the rising plume of air reaches the cloud condensation level at about 1 km. Due to the excess free energy from the latent heat release by condensation, the upward motion is further enhanced. The maximum vertical velocity is reached at 22 min with a mean core updraft wind speed of 6 m s^{-1} and with maximum values of up to 18 m s^{-1} (see fig. 3.3b). Figure 3.3a shows the liquid water path peaking at about 25 min. The clouds further growth is inhibited by the surrounding stably stratified air. The inertia of the uprising air allows the plume to penetrate into the dry and potentially warmer air. Figure 3.4 presents vertical cross-sections of the buoyancy, computed following eq. (1.8). If we examine the buoyancy situation at 25 min we see that the cloud has reached regions above 2.5 km where the surrounding air is warmer than the cloud. The cloud's negative buoyancy induces a downward acceleration. The corresponding subsequent downward circulation leads to peak minimum vertical velocities at about 26 min with downward velocities as low as -10 m s^{-1}. The cloud then dissolves during the next 25 min.

All the while, radiative heating acts on the individual air volumes. Figure 3.5 depicts the corresponding radiative heating rates during the evolution of the cloud (sun shines from the left). The general effects in the thermal spectral range are a modest heating at the cloud bottom because the warmer surface emits more radiation than the cloud and a cooling at cloud top and side faces because of the emission of radiation to space. If we closely examine the exterior surface of the cloud we can see that the superposition of the thermal and solar radiative heating leads to sharp gradients in heating rates. This is especially evident at the top of

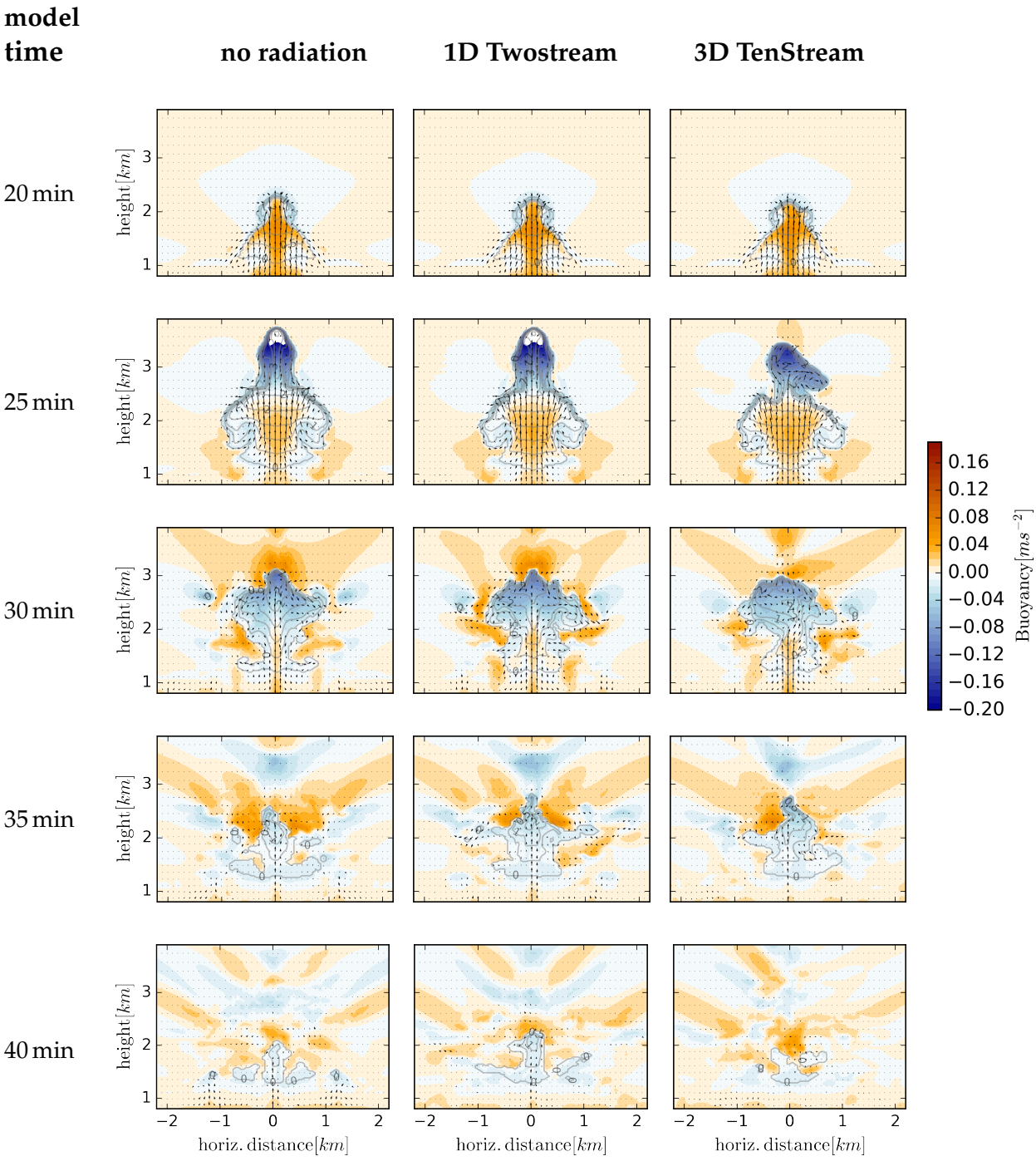

Figure 3.4: Warm-bubble experiment: south to north vertical cross section at the center of the initial temperature perturbation. Shown are liquid water content in [g kg^{-1}] (by contour lines), buoyancy (colormap shading) and wind arrows.

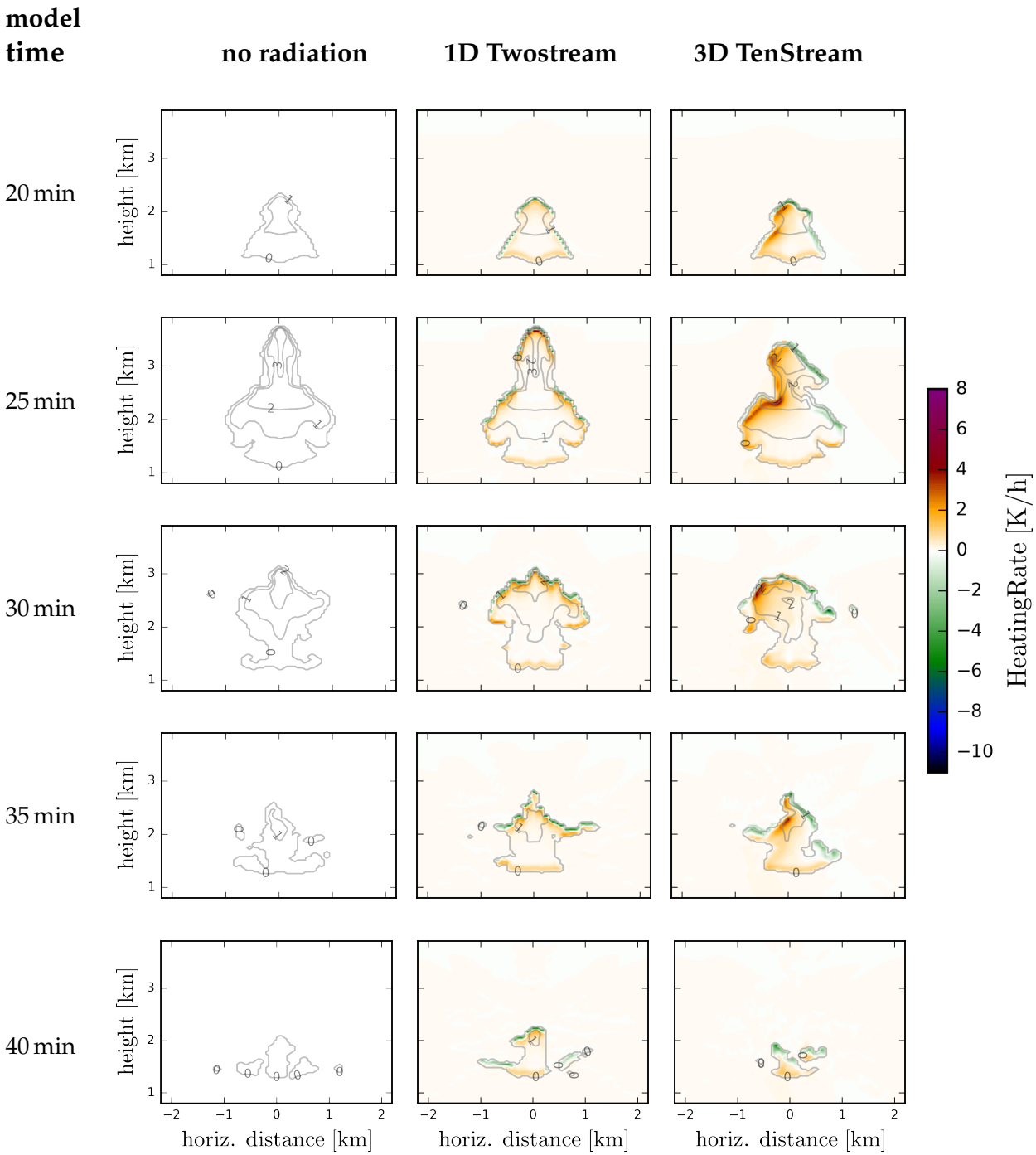

Figure 3.5: Warm-bubble experiment: south to north vertical cross section at the center of the initial temperature perturbation. Shown are liquid water content in $[\mathrm{g\,kg^{-1}}]$ (contour lines) and net radiative heating (colormap shading). Sun is in the south (left)

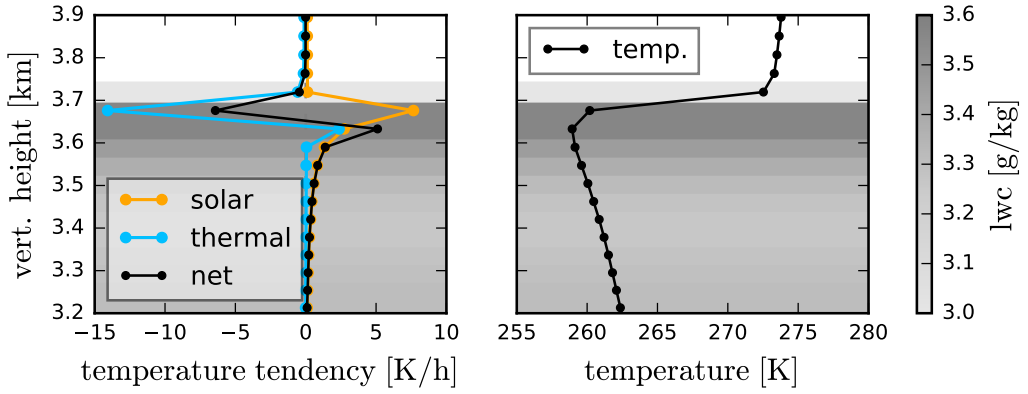

Figure 3.6: Vertical radiative heating profile for the warm-bubble experiment with the Twostream solver at the time 25 min. On the left, the vertical profile of radiative heating at cloud top, on the pixel where the cloud reaches highest. Thermal radiative heating shows a strong cooling at cloud top but with limited penetration into the cloud. Solar heating also happens deeper inside the cloud. On the right, the vertical temperature profile. The gray shaded areas illustrates the liquid water content.

the cloud where we find a particular sharp gradient from cooling to heating. Figure 3.6 displays the vertical heating profile for the Twostream simulation on the center pixel. Long-wave cooling only takes place in the outermost shell because of large absorption optical depths, i.e. cooling usually acts unto a depth from meters to tens of meters. The interior of the cloud is in thermal radiative equilibrium. The thermal warming below the cooled layer may be surprising but is explained with a sharp temperature gradient at the top of the cloud. The uppermost layers of the cloud, are warmer than the layer below, which may be due to entrained warmer air from above. The cloud shell therefore cools to space but also warms the interior of the cloud.

Solar radiation on the other hand, is scattered further into the cloud and thus also heats the interior of the cloud. The combined effect of solar and thermal radiative heating shows to mostly cancel out in the clear sky next to the cloud. Then, we find a sharp layer of strong thermal cooling and, further inside the cloud, solar heating prevails.

Let's compare the evolution for the three cases: without radiative heating, with the one-dimensional Twostream solver and with the three-dimensional TenStream solver. In fig. 3.3a, we find that the "no-radiation" simulation produces the highest amount of liquid water in the initial phase of the rising plume. This is accompanied by a slightly higher maximum cloud height (100 m, not shown) as well as slightly higher vertical velocities (5 %). These changes are however subtle. Usually, in LES simulations, one initially perturbs the temperature field to break symmetries so as to speed up the generation of the turbulence spectrum. However, for the here presented particular warm bubble experiments, no initial perturbation was introduced to specifically examine the influence of the directional heating in the case of 3D RT. That said, I performed several "no-radiation" simulations with a random, unbiased initial temperature perturbations below 100 m, with a magnitude of 0.05 K. The

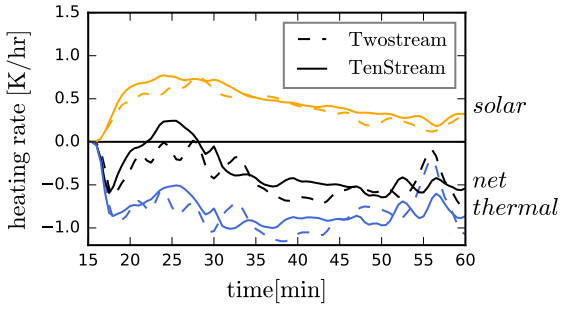

(a) Conditionally sampled radiative heating and cooling rate

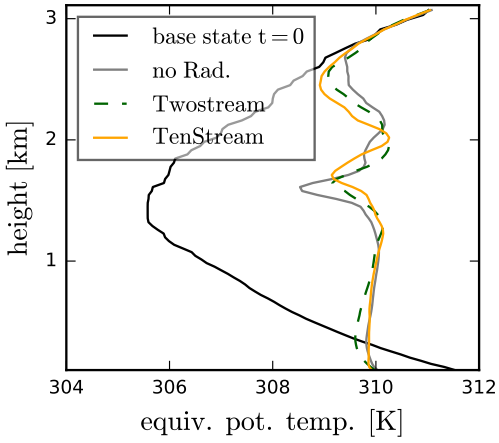

(b) Equivalent potential temperature θ_e profiles.

Figure 3.7: Warm-bubble experiment: (left) time-series of mean radiative heating and cooling rates, sampled at cloudy voxels only (LWC>0), and (right) the vertical profiles of equivalent potential temperature, averaged from minute 50 to 60 over a horizontal square area from -2 km to 2 km.

spread of the liquid water path in the perturbed simulations is shown as a shaded area and shows bigger differences than the different radiative transfer solvers. We should therefore refrain from over-interpreting the results in the initial phase of the warm-bubble. I think it can nevertheless be of value to discuss the differences in the net radiative forcing between the simulations and highlight possible implications.

If we look at the heating rates at 20 and 25 min in fig. 3.5 it is clear that the TenStream solver introduces an asymmetric heating to the cloud system. This enhanced heating at the south face (left) compared to the stronger cooling at the north face (right) leads to an early change in the evolution of the cloud. The asymmetric heating introduces an overturning of the updraft motion and subsequently leads to a reduced cloud height and a diminished liquid water path.

Figure 3.7a shows the time-series of thermal and solar radiative heating rates inside the cloud. The overall radiative forcing on the clouds shows a warming of approximately 0.5 K h^{-1} due to solar heating and about 1 K h^{-1} cooling due to thermal emission. The three-dimensional TenStream solver leads to an average increase in solar warming by 48 % compared to the Twostream solver. It may be surprising to see that the TenStream leads to weaker thermal radiative cooling than the one dimensional solver. On average, we find that the TenStream produces 7 % less cooling. We would generally expect larger cooling rates from a three-dimensional radiative transfer solver and indeed, offline radiative transfer computations (not shown here) at several timesteps of the warm-bubble simulations show that the TenStream solver produces consistently larger cooling rates. Following these results, we can deduce that the diminished cooling in the TenStream case is a consequence of the more compact shape of the cloud.

Figure 3.8 shows the net radiative heating rates in the atmosphere during the simulations and it is clear that this radiative warming and cooling should directly

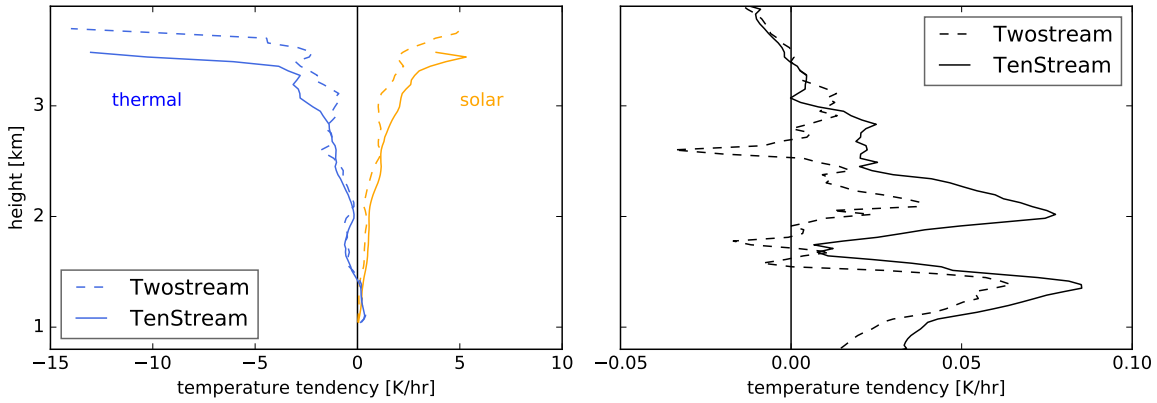

Figure 3.8: On the left, vertical profiles of mean warming and cooling rates, conditionally sampled at cloudy voxels only (LWC>0). On the right, mean radiative heating profiles averaged over a horizontal square area from -2 km to 2 km.

influence the vertical temperature profile. That said, we should note that while the mean radiative forcing during the simulation reaches significant levels at cloudy voxels (left side of fig. 3.8), the net change on the temperature distribution averaged over cloudy and clear-sky regions (right hand side panel) is less than 0.1 K.

To get a feeling for the magnitude of the radiative forcing compared to the dynamical influence we may have a look at the equivalent potential temperature θ_e (see eq. (1.9)) before and after the warm-bubble occurred (fig. 3.7b). The equivalent potential temperature is strictly speaking only a conserved quantity in moist-adiabatic processes. Radiative transfer is of course a direct violation of this assumption but if we take a look at the various simulations, we may recognize that the differences between them are about one order of magnitude bigger than the net influence of radiative heating. Differences in the vertical profile of θ_e show magnitudes of about 0.5 K whereas net radiative heating accumulates only to 0.05 K h^{-1} as shown in the right panel of fig. 3.8. Neglecting radiative processes, we may treat the equivalent potential temperature as a conserved quantity and any changes are thus an indicator for mixing processes. Comparing the initial distribution of equivalent temperature and the change over the course of the simulation, we see that the convective motion of the warm bubble considerably stabilizes the atmosphere. A close look at the distribution of equivalent temperature above 2 km reveals that, compared to the TenStream run, the "no radiation" and the Twostream run lead to an enhanced stabilization of the atmosphere. The reduced gradient in the upper part of the atmosphere suggests that the "no-radiation" run is most efficient in vertically mixing the atmosphere. This may be explained by the deeper penetration into the inversion and thus an enhanced mixing with drier and relatively warmer air.

3.1.2 Coupling to an Interactive Surface Model

Arguably the most prominent feature of three-dimensional radiative transfer is the slanted propagation of radiation emitted by the sun. This is especially pronounced at the surface where local differences in solar absorbed energy are very well on

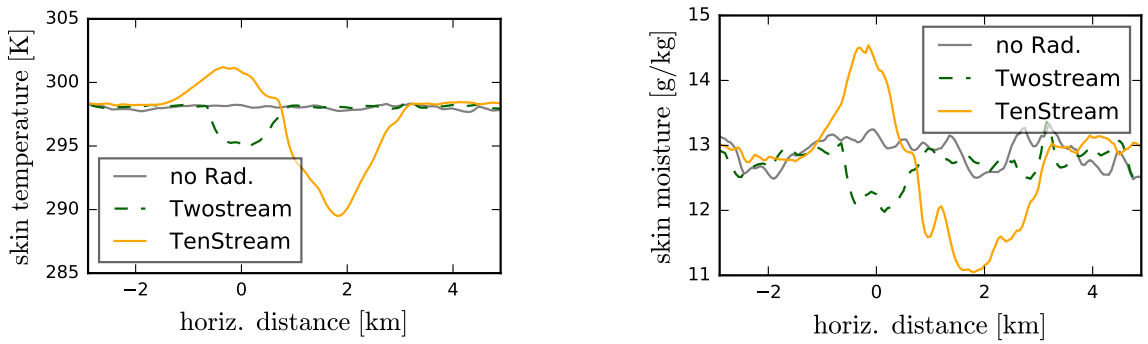

(a) surface temperature

(b) skin humidity volume mixing ratio

Figure 3.9: Warm-Bubble experiment with interactively coupled surface model: Skin temperature and humidity values are averaged over a north to south strip from -2 km to 2 km as well as over a timespan from 35 min to 40 min. Sun is shining with a zenith angle of 40° from the south (left)

the order of several hundred W m^{-2}. Let's have a look at three new warm-bubble experiments: again one simulation with "no radiation", one with the Twostream solver and one using the TenStream radiative transfer solver. However, in contrast to the preceding simulations, we now couple the incident radiative fluxes at the surface interactively to a surface model (as described in section 1.3). The soil model consists of four interactive layers with a skin layer to exchange fluxes from the atmosphere to the soil model and vice versa. The model parameters are chosen to mimic grasslands supported by a moist loamy ground, characteristic for pasture landscapes in Europe (see section 4.3 for detailed namelist parameters). In the case where no interactive radiation is computed, the net surface flux is fixated to the average incoming radiation of the Twostream run (582.5 W m^{-2}).

Figure 3.10 depicts again the atmospheric heating rates during the simulation for the three simulations. In addition we see the net surface flux below the cloud. While the radiative surface flux is constant in the case of "no-radiation" we find that the net surface flux is greatly diminished below the cloud in the case of the Twostream simulation. In contrast to the one-dimensional solver, we can see that the TenStream solver displaces the cloud's shadow horizontally to the north (right). Furthermore, we find a distinctly higher surface flux beneath the illuminated side of the cloud. This local maximum is composed of the slanted direct radiation, the diffuse radiation reflected by the cloud as well as thermal radiation emitted from cloud base.

One distinct feature is the asymmetry in the shape of the cloud, irrespective of the radiative transfer method. Why does the interactive surface model introduce asymmetries in the flow if it is not perturbed asymmetrically? To understand the asymmetries, we should have a look at the surface skin temperature in fig. 3.13. Like in a hot frying pan, we can clearly see the evolution of Bénard cells. These convective cells lead to anisotropic conditions for the evolution of the warm bubble. If we homogenize the latent and sensible heat flux (not shown), we regain the symmetry for the "no-radiation" and Twostream simulations.

The liquid water path in fig. 3.12a shows that the cloud deceases quickest in

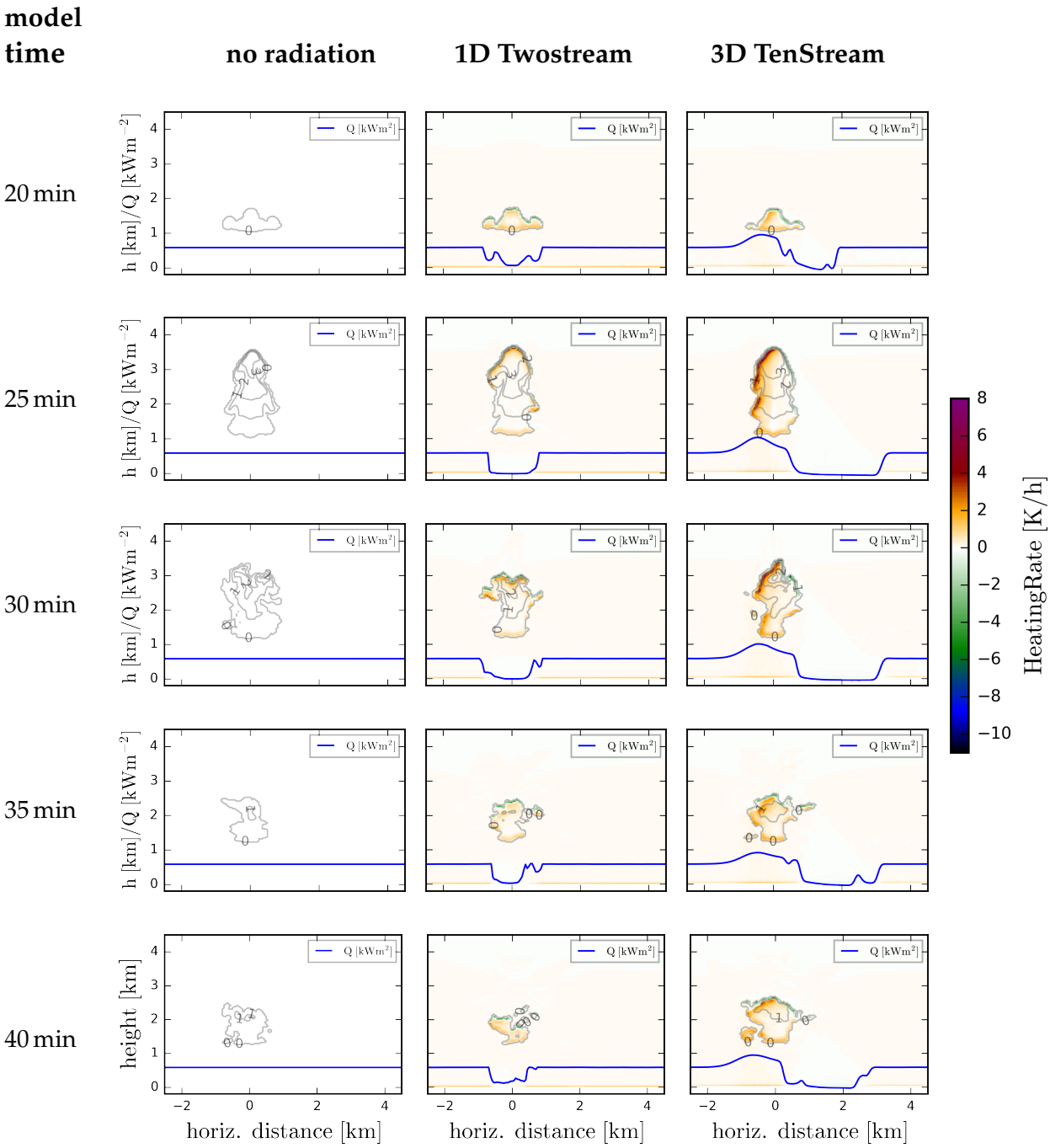

Figure 3.10: Warm-bubble experiment with interactive surface model: south to north vertical cross section at the center of the initial temperature perturbation. Shown are liquid water content as g kg^{-1} by contour lines and net radiative heating (colormap shading). Line plot denotes net surface heating in kW m^{-2}.

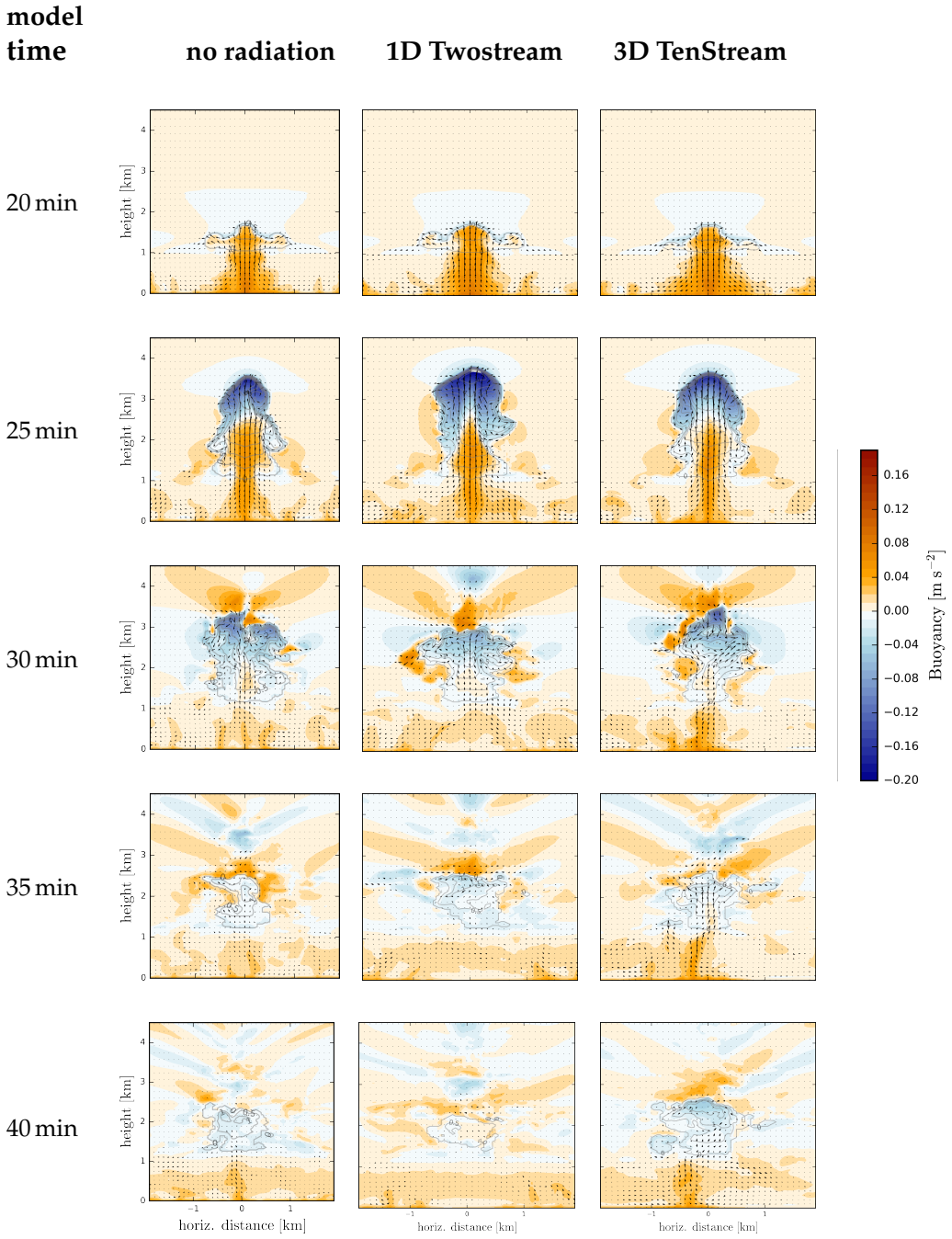

Figure 3.11: Warm-bubble experiment with interactive surface model: south to north vertical cross section at the center of the initial temperature perturbation. Shown are liquid water content as $\mathrm{g\,kg^{-1}}$ by contour lines, buoyancy (colormap shading) and wind arrows.

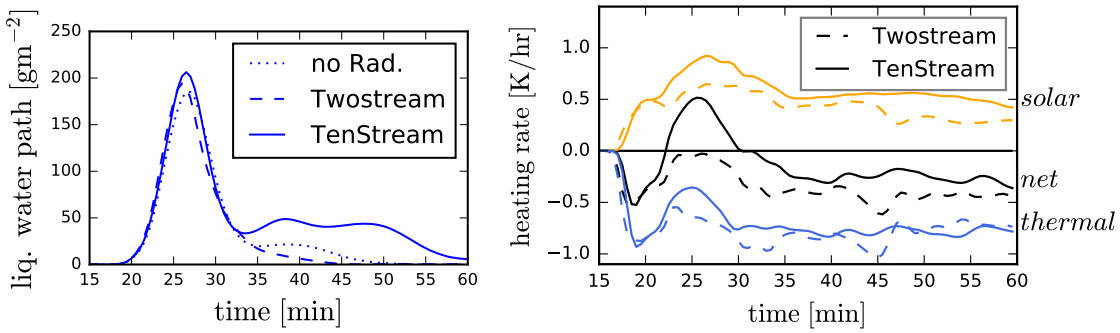

(a) liq. water path

(b) cond. sampled mean heating rate

Figure 3.12: Warm-bubble experiment with interactive surface model: timeseries of (a) liquid water path (averaged over time and a horizontal square area from -2 km to 2 km) and (b) the mean radiative heating rates conditionally sampled at cloudy voxels only (LWC>0). All averages are weighted by physical height.

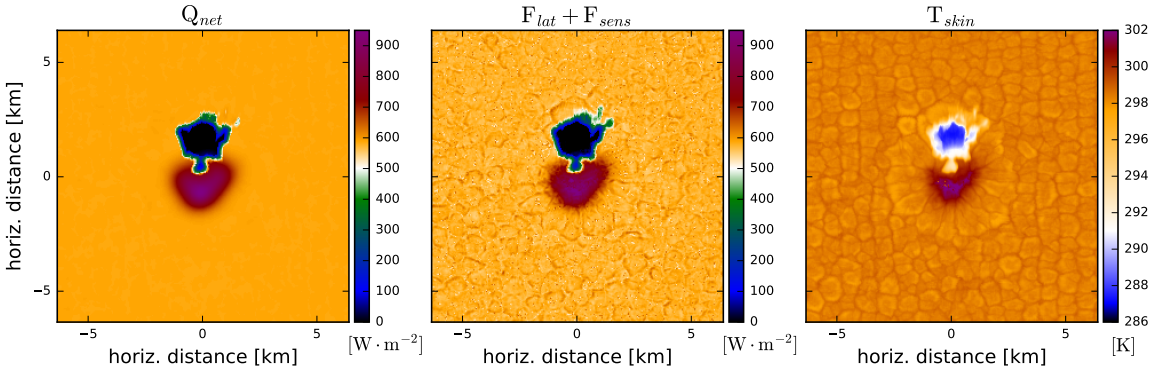

Figure 3.13: Net radiative flux Q, latent and sensible heat flux ($F_{latent} + F_{sensible}$) and surface skin temperature at $t = 40$ min for the TenStream run. Notable features are the shadowy region and the evident Bénard cells.

the case with one-dimensional radiation. This diminished cloud activity is a consequence of the shadow that is cast directly beneath. The decrease in solar incident energy decreases the surface fluxes in the updraft region and in turn reduces the cloud development.

As it was mentioned earlier, with three-dimensional radiative transfer, the cloud does not cast a shadow directly below itself. The increased and continuous net radiative surface flux leads to a higher surface skin temperature (fig. 3.9a) and consequently to larger latent and sensible heat fluxes as well as an increase in evaporation (fig. 3.9b). The continued support with warm and moist air from below the cloud is also evident in the buoyancy plots in fig. 3.13. Or, put it the other way around, note the absence of buoyant air near the surface in the Twostream simulation (e.g. at $t = 40$ min.). In the TenStream case, we find the cloud development to be strengthened and the lifetime of the cloud is increased by approximately 20 min.

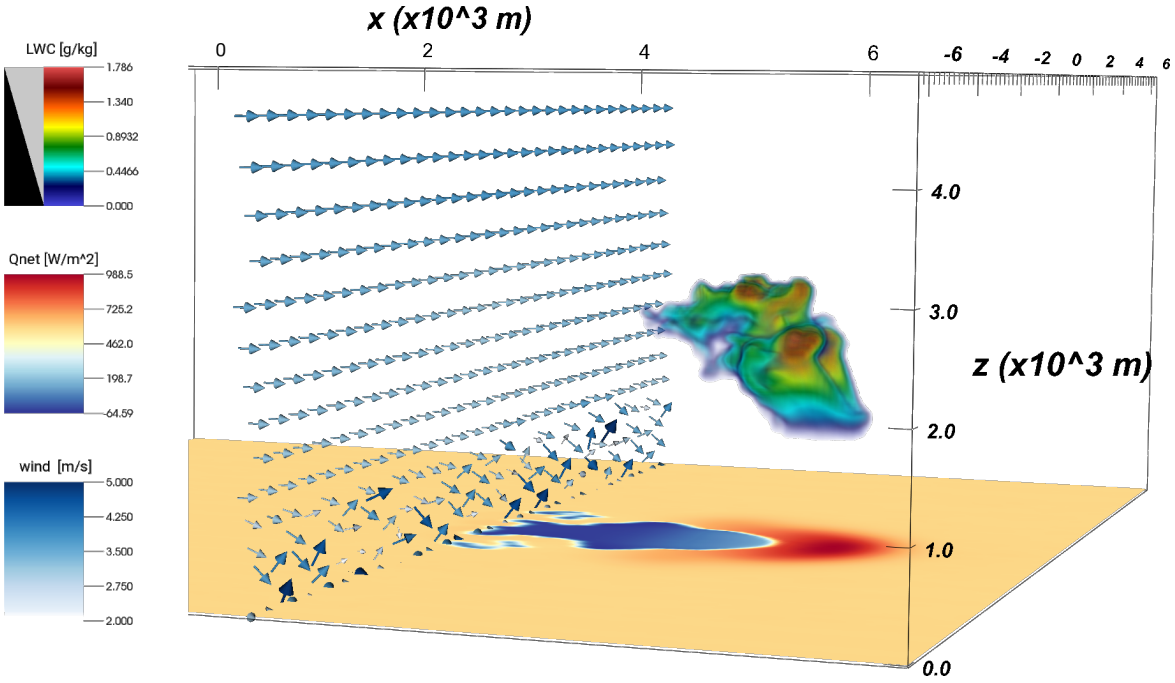

Figure 3.14: Volume rendered perspective on liquid water content of the warm-bubble simulation with interactive surface and a horizontal wind profile. Shown are one cross-section of wind vectors, the radiative net surface flux (Q_{net}) and the liquid water content at time $t = 30$ min. The west-wind carries the cloud to the right, while the sun is situated in the east at a zenith angle of 40° and illuminates the "front-side".

3.1.3 Influence of a Horizontal Wind

As we have seen in the preceding section above, the local surface fluxes may dramatically change the evolution and lifetime of a cloud. However, in nature, we will commonly find a horizontal wind that will displace the cloud. This motion of the cloud's shadow of course smooths the radiative impact on the surface. Accordingly, let's consider a new set of warm-bubble experiments. Like in the previous setup we use an initial temperature perturbation in the lower atmosphere to trigger a convective motion. Radiative fluxes at the surface are coupled to an interactive surface model and now we additionally introduce an initial horizontal wind profile.

The following experiments will shed some light on the interplay of radiative heating, cloud dynamics and surface fluxes. The horizontal westerly wind u is set according to a power law, which is representative for open land surfaces [Peterson and Hennessey, 1978]:

$$u(z) = \left(\frac{z}{1km}\right)^{1/7} \cdot 3\,\frac{m}{s}$$

which results in a wind speed of $3\,\mathrm{m\,s^{-1}}$ to $4\,\mathrm{m\,s^{-1}}$ between cloud base and top. Apart from the horizontal wind, the setup of the simulations is the same as before in section 3.1.3. The sun zenith angle is still constant at 40° but we conduct four sets of simulations where the sun's azimuth is picked so that the light is shining from each cardinal direction (N, E, S, W).

The horizontal wind leads to a preferred cloud formation with the cloud base

being further "ahead" than the cloud top. Figure 3.14 shows a volume rendered perspective of the cloud, depicting the horizontal westerly wind as well as the incident radiative surface fluxes for the case that the sun is shining from the east. This tilt of the cloud shape leads to differences in the projected area of the cloud that is illuminated by the sun and depends on the solar azimuth angle. Figure 3.15 shows the average radiative heating of the cloud over time. Due to the symmetric nature of the north (N) or south (S) simulations, it is no surprise that they show the same solar warming. Accordingly we find a non-symmetric behavior in the west (W) and east (E) case. The presented case in fig. 3.14 with the sun in the east, maximizes the projected area of the cloud. Figure 3.16a shows differences in soil temperature variability, presenting a measure for the distribution of surface fluxes during the simulations. For one, it is clear that a bigger cloud projected area leads to an enlarged shadow at the surface and hence less energy input at the surface. This net radiative bias is however not wholly responsible for the differences in surface temperature variability. It is also the interplay between near surface winds and the location of the shadowy region. The western sun (casting the shadow forward, along track) indeed counteracts the dynamically induced temperature field variability, while the other sun positions show to enhance the variability.

That said, while we find measurable differences in the net radiative heating, the liquid water path as shown in fig. 3.16b is statistically indistinguishable between the various TenStream solutions. In the earlier experiment with a stationary cloud we found that the location of the cloud's shadow and hence the localization of surface fluxes influences the cloud's lifetime. Here, however, in the presence of a background wind field, we find that the horizontal displacement seems to soften the impact that local surface flux variability has on the evolution of the cloud. This also applies to the effects of one-dimensional radiative transfer: in the preceding stationary cloud experiment, we had a reduced cloud development because of "self-shadowing" whereas we now find that this effect is mitigated by the horizontal displacement.

In conclusion, we find that the horizontal wind mitigates the effects of radiative transfer. Having said this, we see that the surface model retains some "temperature-memory" beyond the time scale of a single cloud. These local differences in temperature may yet influence the point in time and the location where the next plumes rise (section 3.2 will follow up on this assumption). It is specifically noteworthy that the influence of radiative transfer depends on the angle between the sun's azimuth and the wind direction.

3.1.4 Discussion

The preceding section examines the cloud-radiative feedback mechanism for a single convective plume that is artificially triggered through a positive temperature perturbation at the beginning of the simulation. The first experiment examines the influence of radiative heating, only considering heating rates in the atmosphere. The second setup introduces a coupling to an interactive surface model which shows to be particularly important to study first order three-dimensional effects such as the displaced shadow at the surface. The third experiment further intro-

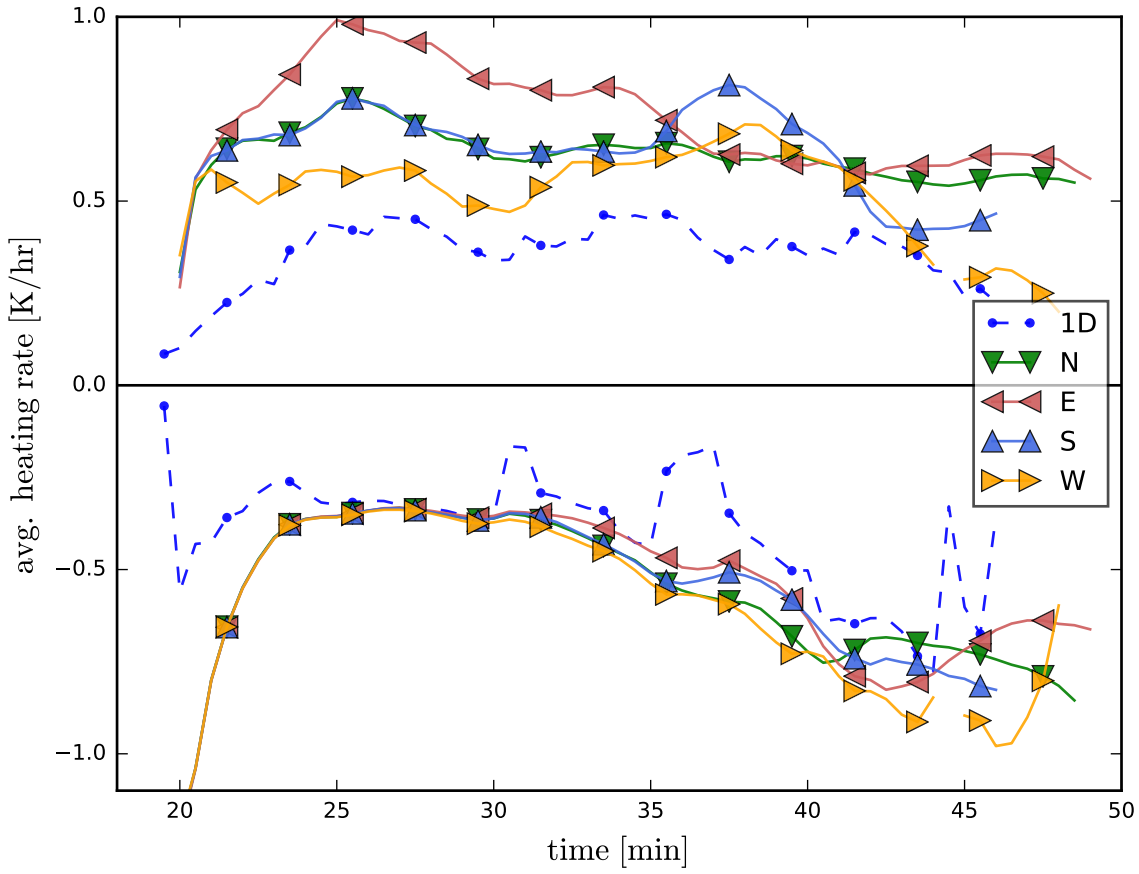

Figure 3.15: Solar (top) and thermal (bottom) mean radiative heating and cooling rate, conditionally sampled at cloudy voxels only (LWC>0). N, E, S, W denote the cardinal position of the sun (azimuth angle), which is located at a zenith angle of 40°

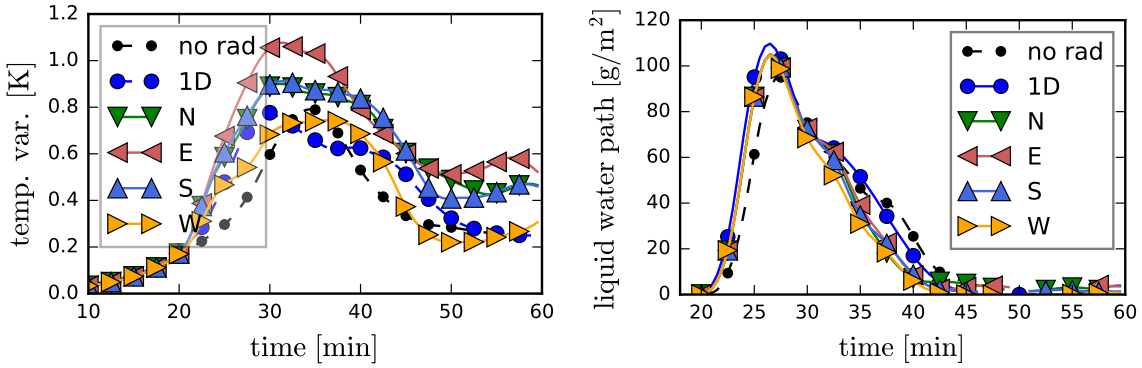

(a) skin temperature variance **(b)** mean liquid water path

Figure 3.16: Warm-bubble experiment with an interactive surface model and including a horizontal wind profile. Shown are time-series of (a) the horizontal variance of the skin layer temperature and (b) the liquid water path (weighted by physical height). Both variables averaged over a horizontal square area from -2 km to 2 km around the cloud center.

duces a horizontal wind profile to examine if three-dimensional radiative transfer effects persist beyond a time scale of a single convective plume. Let's summarize the key findings:

Warm bubble experiment with radiative heating only in the atmosphere:

- The choice of the radiative transfer solver does not change the cloud's lifetime or the mean liquid water path in a significant manner, i.e. perturbations of the initial conditions lead to bigger differences than those accountable to the radiative transfer.
- Three dimensional solar radiative heating at the illuminated cloud side introduces an asymmetry in an otherwise symmetric setup. This asymmetry induces an overturning of the updraft motion and subsequently changes the shape of the cloud.
- The net radiative heating of the TenStream solver is warmer than in the case of the Twostream run. Besides an increase in solar heating due to cloud side illumination, we also find a diminished thermal cooling which is a result of the altered and more compact cloud shape.

Warm bubble experiment with radiation interactively heating the surface:

- One dimensional radiative transfer casts the shadow onto its own updraft region. The resulting lack of warm and moist air supply from below reduces the growth of the cloud compared to simulations with fixed surface fluxes.
- Three dimensional radiative transfer on the other hand leads to a local maximum of surface fluxes right beneath the cloud. This maximum is comprised of thermal emission from cloud base, the absence of the cloud's shadow (which is displaced sidewards) and the diffuse reflection on the cloud side. As a consequence we find an increase in surface temperature and evaporation (and hence increased latent and sensible heat fluxes) beneath the cloud. This constant supply of moist and warm air stabilizes the updraft and in turn as much as doubles the cloud's lifetime.

Warm bubble experiment with an interactive surface model and an initial horizontal wind profile:

- The horizontal wind smooths the influence of differential surface heating. The cloud inhibiting effect of "self-shadowing" that was apparent with one-dimensional solvers as well as the increase of a cloud's lifetime due to an increase in surface fluxes in the case of the TenStream solver is diminished through the horizontal displacement (non-stationarity).
- Three-dimensional radiative heating shows to be dependent on the direction of the sun and the wind. The horizontal wind tilts the cloud and, as a consequence results in a dependence of the "sun-lit" projected area on the angle

between the wind direction and the solar azimuth and zenith angle. This directionality leads to differences in atmospheric heating and surface temperatures. The surface model retains some "temperature-memory" beyond the time scale of the single cloud and the duration of the simulation.

To my knowledge, the here presented warm-bubble experiments are the first ones of its kind. Earlier studies considered either only solar or only thermal radiative transfer or no three-dimensional radiative transfer at all.

Guan et al. [1997] and Klinger [2015] for example, examined a warm-bubble cloud and the influence of thermal radiative transfer. Both found that thermal cooling at cloud edges increases a cloud's liquid water content which increased condensation. Guan et al. [1997] also attributed the increase in the cloud's water content to a secondary circulation at the cloud edges that enhanced local horizontal buoyancy gradients and led to an enhanced cloud growth.

If we were to compare their results to the here conducted experiments, we should consider the simulations without an interactive surface model as in section 3.1.1. The here presented setup however seems not to allow for such detailed analysis as the effects of the various radiative transfer methods do not show differences in the liquid water path that are statistically significant, i.e. they are smaller than the sensitivity on the initial conditions. Even if we were to perform a direct comparison it would not be surprising if we drew different conclusions, considering that maximum updraft velocities in both their studies reach only approximately $1\,\mathrm{m\,s^{-1}}$ whereas the simulations in this work are subject to way stronger upward motions with vertical winds of about $5\,\mathrm{m\,s^{-1}}$.

Wapler [2007] studied the influence of a displaced cloud shadow on the evolution of a warm-bubble simulation and also found that the displacement introduces an asymmetry in the flow. In contrast to the experiment here, she found that the consideration of the shadow displacement leads to a diminished evolution of the warm-bubble cloud. It is again difficult to directly compare the results because of fundamental differences in the setup of the simulation. In her experiments, the cloud condensation level was already at 200 m at a 30° solar zenith angle which means that the shadowy area is much closer to the updraft region of the cloud compared to the here conducted experiments. This may be furthermore important because, instead of an interactive surface model, she used the net radiative flux to instantaneously update the surface fluxes. Further notable differences are the weak vertical velocities of maximally $2\,\mathrm{m\,s^{-1}}$ and the neglect of thermal radiative transfer.

In conclusion of the here presented warm-bubble experiments, we should record that the evolution of the cloud is predominantly controlled by the dynamical forcing. Radiative heating in the atmosphere shows to have a minor effect on the course of the simulation. At the same time, we should keep in mind, that numerical noise and the sensitivity on the initial conditions renders this type of analysis questionable. It may prove essential to run an ensemble of numerical experiments with varying initial conditions to fully comprehend the consequences of one- or three-dimensional radiative transfer effects.

An ensemble for the here presented simulations would have been overly costly computationally and is not in the scope of this work. However, in a way, we will

study an ensemble of single convective clouds in the upcoming section 3.2.

Apart from that, if we consider the radiative surface fluxes to be coupled interactively to a surface model, we find that the displacement of the cloud's shadow triggers a strong change in the evolution of the simulations, even on short time scales of a single plume.

3.2 Immediate Influence of Radiative Heating on Local Weather Evolution

In the preceding section 3.1.4 we discuss the influence of radiative heating on the evolution of a single convective cloud. We do not only find differences between simulation without radiation computations and the ones with one-dimensional radiative transfer but there are particularly interesting differences due to three-dimensional radiative transfer effects. This brings us to the question: when radiative transfer has an influence on a single cloud what are the effects on subsequent convective clouds? Do these effects accumulate or average out over time? What are the effects concerning the choice of the radiative transfer method with respect to timescales of several consecutive convective plumes?

To that end, I performed UCLA–LES simulations over a time period of several hours. The domain size was chosen to be 50 km $\times$ 50 km horizontally (512 grid points in each direction) at a horizontal resolution of 100 m. Vertically, the domain extends over 3.1 km with a vertical resolution of 50 m near the surface and vertically stretched by 1 % of the absolute height. The average time-step was 8 s and the simulations only consider warm microphysics without rain. The sun is positioned at a fixed azimuth angle (south) and a constant zenith angle of 60°. The simulations were done using the full spectral integration.

This study includes three experiments in close analogy to the warm-bubble experiments (preceding section 3.1). One set of simulations where radiative heating rates are only considered in the atmosphere (section 3.2.1) and a second set of simulations with an interactively coupled surface model (section 3.2.2). The third set of simulations in section 3.2.3 introduces a horizontal wind field to study the impact of the dynamical smoothing of the interaction between radiation and the surface.

3.2.1 Evolution of a Shallow Cumulus Cloud Field

A simulation without any radiation calculations is run forward for 6 h. This simulation is then used as a restart point for three additional runs. The three simulations run for an additional 6 h period: (a) without radiative transfer computations, (b) with the δ-eddington Twostream solver and (c) with the TenStream radiation code. Surface fluxes are computed using a bulk formulation using a fixed sea surface temperature of 295 K. No initial wind field is prescribed. Please refer to section 4.3 for further details on the input parameters of the simulation.

Figure 3.17 shows the initial profiles at t=6 h from which point the radiation runs are started. It is easy to see that the lower atmosphere is well mixed up to 700 m with an inversion above. Over the course of the simulation, the well mixed boundary layer deepens from 700 m at 6 h to 1.5 km at the end of the simulation at 12 h. The cloud condensation level rises from 540 m to 660 m. The simulations develop small shallow cumulus clouds with mean core updraft velocities of 1 m s^{-1} (see fig. 3.18) covering about 12 % of the domain (see fig. 3.19). Figure 3.20 gives an overview of the simulated cloud field at the end.

The simulations with radiation produce significantly more cloud water than the “no-radiation” simulation.

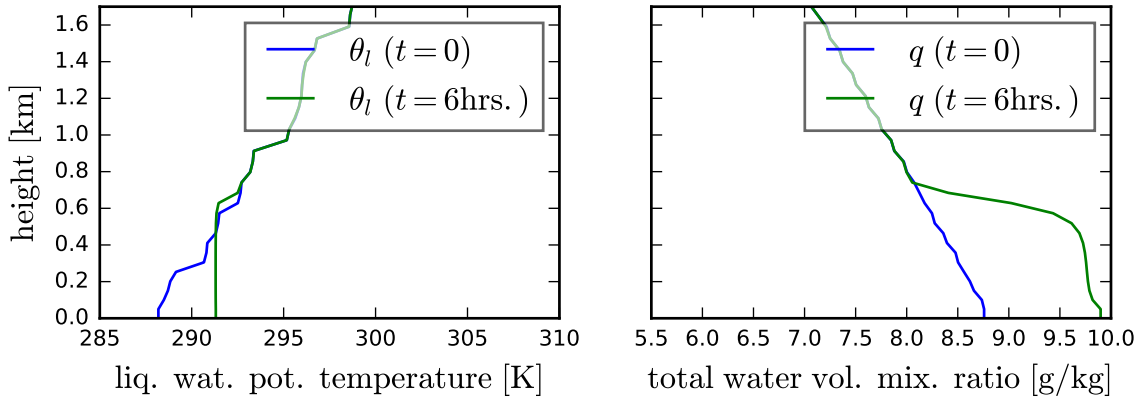

Figure 3.17: Initial vertical profiles of potential temperature and total water mixing ratio at time t=0 h where the "no-radiation" simulation is started and at t=6 h where the simulations with radiation are started from. During the first 6 h, the simulation develops a well mixed layer up to 700 m and the lower atmosphere is considerable moistened by surface evaporation.

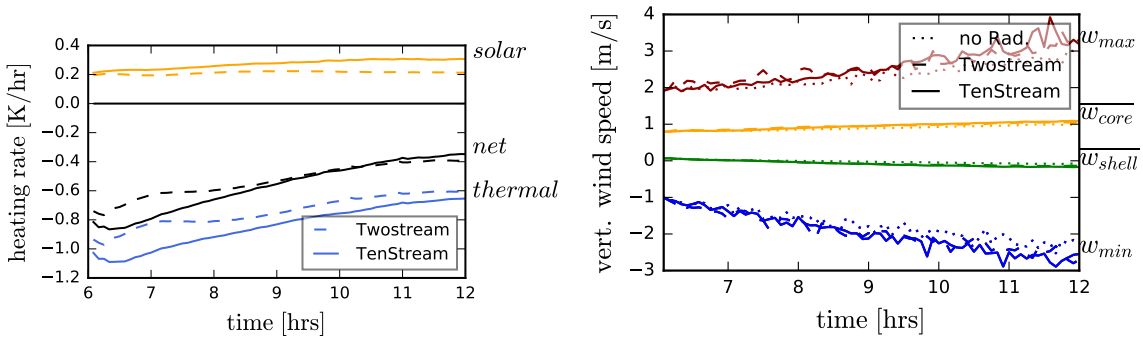

Figure 3.18: Conditionally sampled mean radiative heating rate at cloudy voxels on the left. On the right, the minimum and the maximum vertical velocities as well as the mean cloud core and cloud shell vertical wind speed. Three dimensional radiative transfer shows stronger solar heating and thermal cooling than in the one-dimensional case. Core and shell values are conditionally sampled according to LWC>0 and vertical velocity w $>$ .5 or w $<$ .5 respectively. Interactive radiation leads to slightly larger magnitudes in vertical velocities.

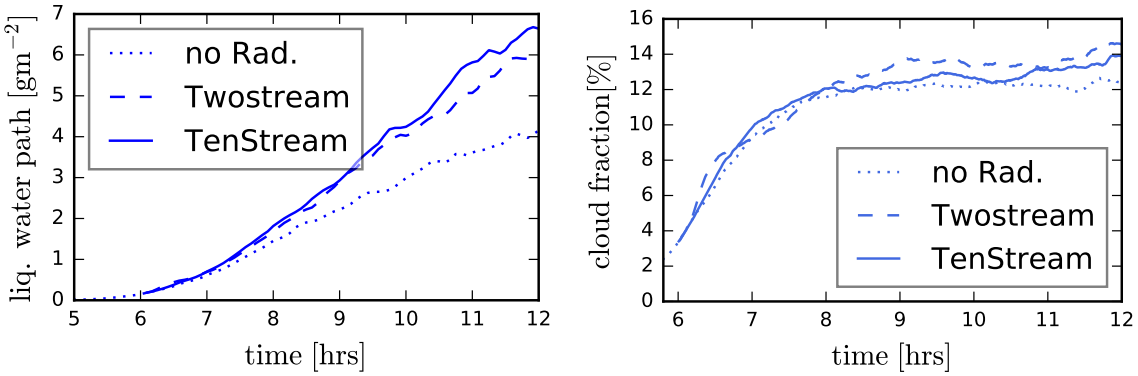

Figure 3.19: Shown on the left is a time-series of the liquid water path for the shallow cumulus cloud field simulations using three different radiation schemes. On the right, we find the domain average cloud fraction. The simulations with interactive radiation calculations develop twice as much liquid water while the average cloud fraction remains the same. This suggests the clouds to be either deeper or thicker.

As we already stated in the discussion of the warm-bubble experiments in section 3.1.4, we may recollect that Guan et al. [1997] and Klinger [2015] found thermal radiative cooling to enhance cloud growth in shallow cumulus conditions. Figure 3.18 also shows a net radiative cooling in the clouds so, naturally, it is not surprising to find the direct effect of thermal cooling leading to enhanced condensation. The conclusion of Guan et al. [1997] as to how radiation feeds back onto the cloud dynamics was that radiative cooling at the cloud top leads to stronger subsidence on the cloud edges, hence leads to a stronger horizontal buoyancy gradient and thus amplifies core updraft velocities. This process should be enhanced further in the case of three-dimensional thermal cooling on cloud side-edges. If we look at the mid panel of fig. 3.21 we find that the distribution of radiative heating supports this theory: radiative heating generally cools the outer edges of the cloud (shell region). At the same time solar warming actually heats the core updraft regions, further enhancing cloud growth. This is in compliance with the expectations and explains the accelerated cloud growth in our simulations with interactive radiation.

Wapler [2007] proposed that differential solar surface heating enhances the circulation as depicted in fig. 3.22. While we will later see that this circulation pattern is further amplified if surface shadowing is considered we find it already present even if we only consider heating rates in the atmosphere. In the case of three-dimensional radiative transfer, we find that the illuminated cloud side is subject to a stronger heating than the shadowy side of the cloud. The differential heating induces a rising motion at the illuminated cloud face and a descending motion on the side that is turned-away. The mean horizontal velocity (right panel of fig. 3.22) supports this theory. The wind profile clearly shows the radiatively induced horizontal wind: at the lower levels from north to south and in the upper cloud layers, the opposite direction, away from the sun.

Having about twice as much liquid water in the simulations with radiation we might wonder how do the individual clouds differ from each other? Interestingly,

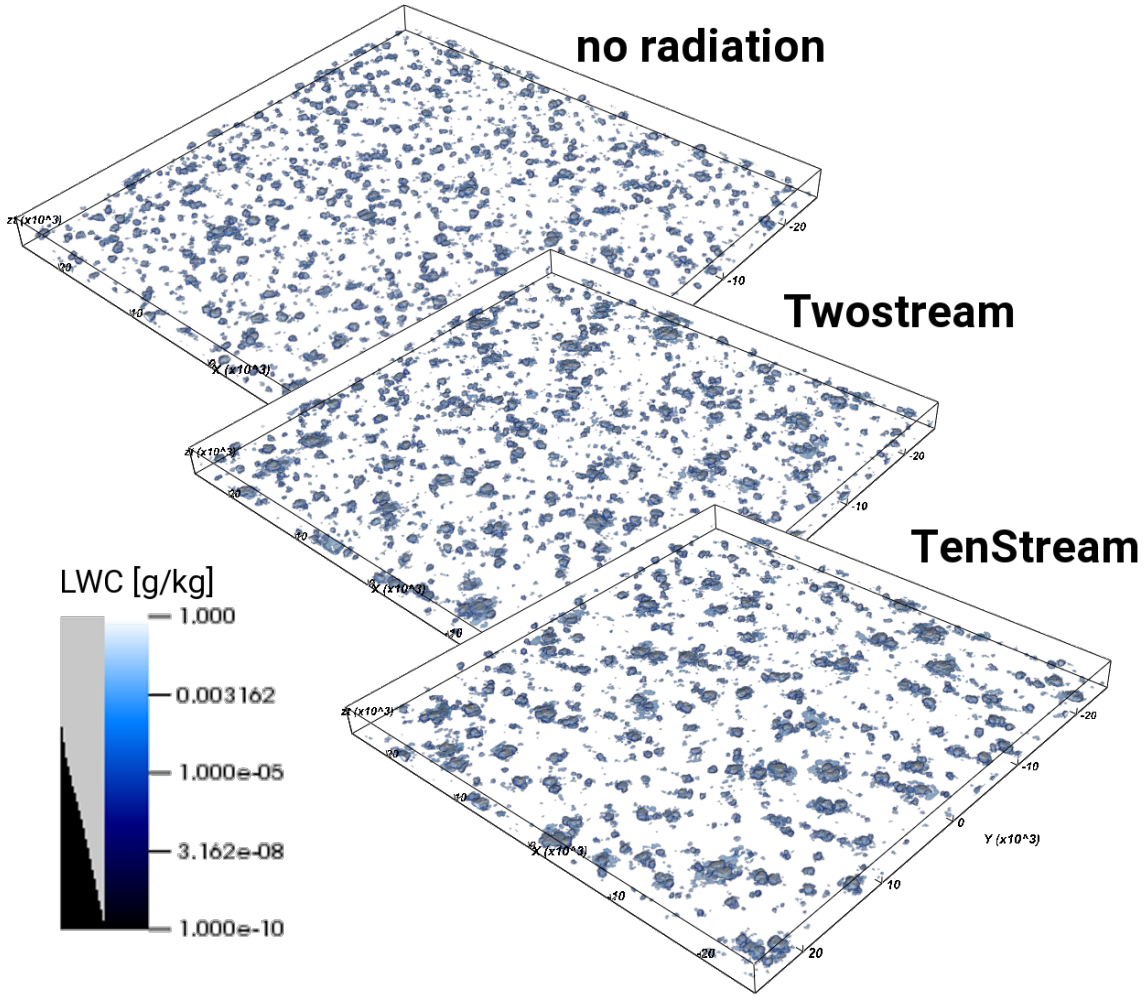

Figure 3.20: Volume rendered perspective on liquid water content at t=12 h. The simulations with interactive radiation develop deeper and slightly larger cloud patches. See fig. 3.24 for a quantitative analysis of cloud patches.

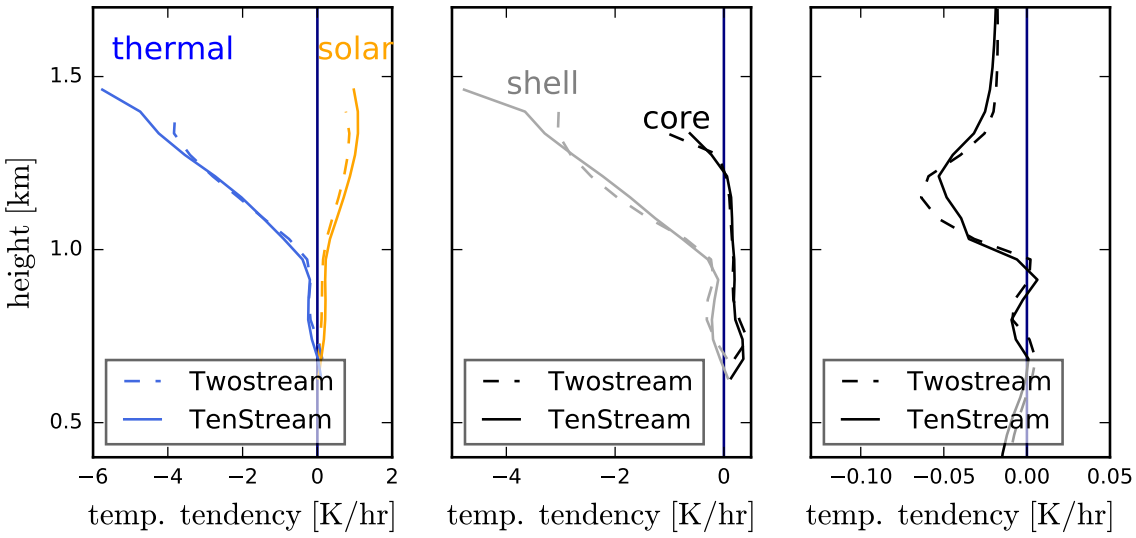

Figure 3.21: On the left, vertical profiles of heating and cooling rates, conditionally sampled at cloudy voxels only (LWC>0). In the center, the mean radiative heating profiles subdivided into cloud core (LWC $> 0; w > 0.5\,m\,s^{-1}$) and cloud shell regions (LWC $> 0; w < 0.5\,m\,s^{-1}$). On the right, the mean radiative heating profiles averaged horizontally over the whole domain (including clear-sky regions). All profiles are averaged over the time period from 11 h to 12 h. Three dimensional radiative transfer shows to bear stronger solar heating and thermal cooling at cloudy pixels compared to the one-dimensional case. The center panel shows the excess thermal cooling to be in the top part of the cloud's outer shell whereas the core updraft regions are subject to radiative heating.

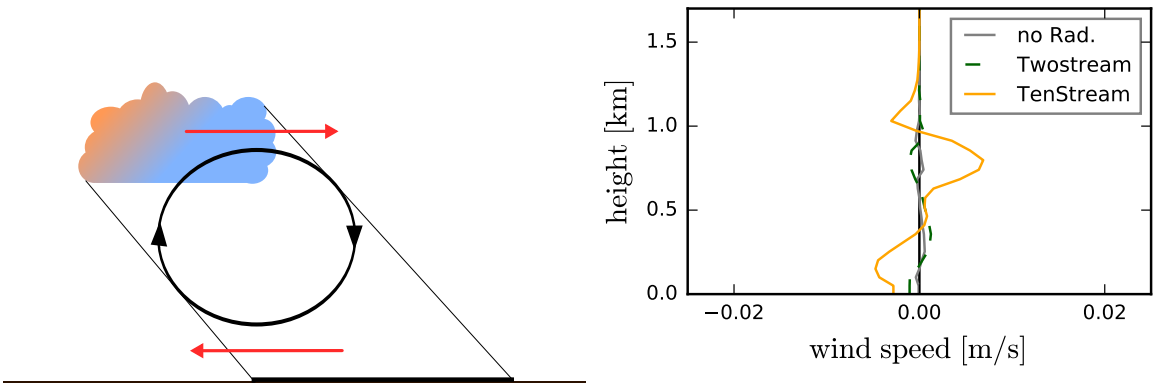

Figure 3.22: A schematic representation of a cloud circulation with solar heating. Depicted is the illuminated cloud side and the displaced surface shadow. The differential heating enhances the circulation that induces a horizontal wind shear. The panel on the right shows the averaged horizontal S-N wind component for the shallow cumulus cloud field simulation. Differential radiative heating induces a wind towards the sun at lower levels and away from the sun at the height of cloud.

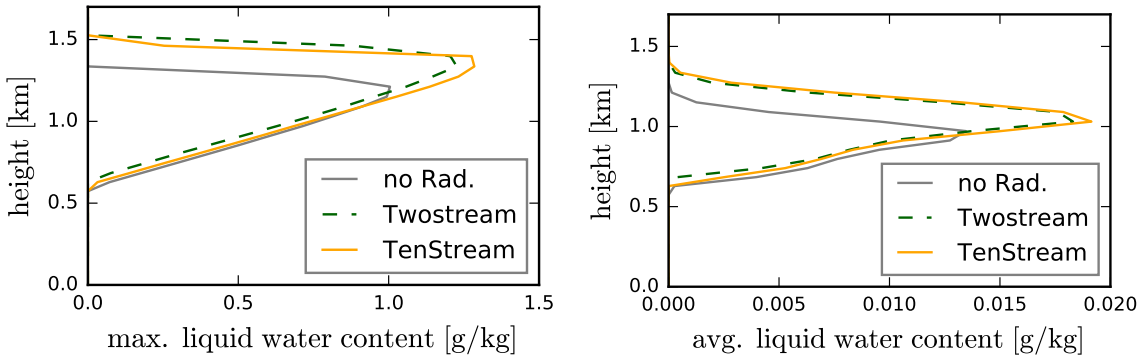

Figure 3.23: Vertical profiles, averaged over the time-period from 11 h to 12 h, for the maximum (left) and the mean liquid water content (right). Interactive radiation leads to thicker (higher liquid water content) clouds that also extend further vertically (deeper).

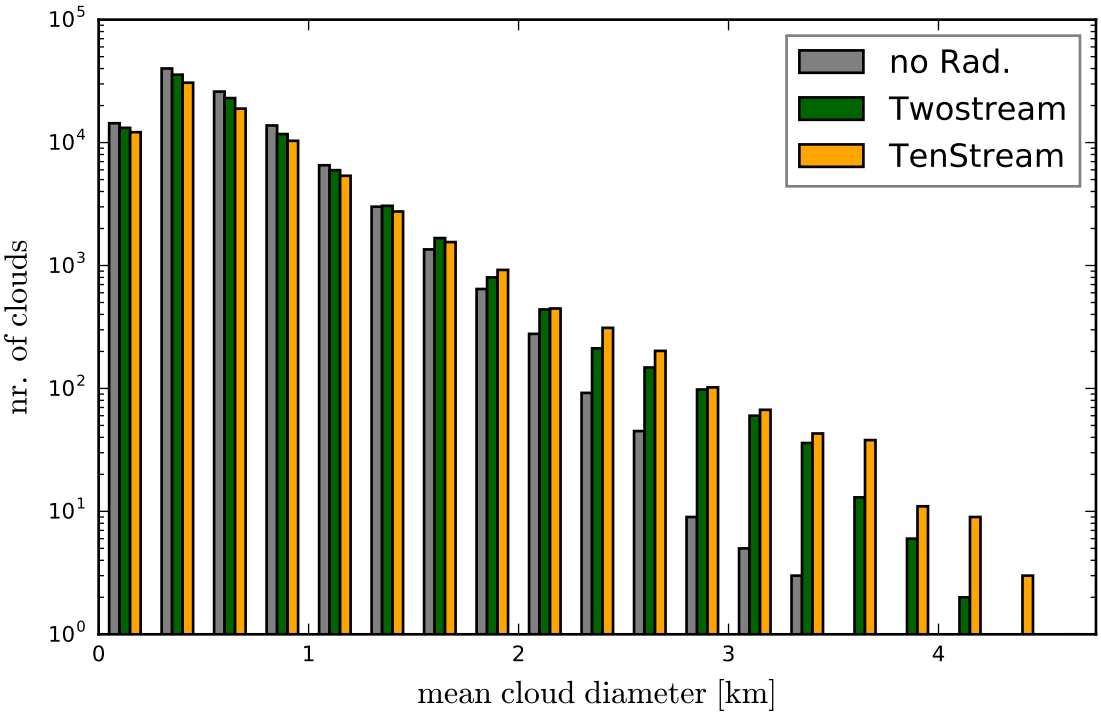

Figure 3.24: Cloud size statistics derived from liquid water path for the shallow cumulus cloud field simulations. Cloud distribution is computed every 5 min from 6 h to 12 h. Cloud clusters are uniquely labeled for all areas that are consecutively connected through a 5-point stencil. The simulation without radiation produces most small clouds whereas the simulations with interactive radiation calculations lead to larger cloud patches. Three dimensional radiative transfer shows to produce the largest clouds.

we do not find a significant change in the mean cloud cover (see fig. 3.19). That can only mean that the clouds are either thicker (higher liquid water content) or are deeper vertically. And indeed, as we can see in the vertical distribution of cloud liquid water (fig. 3.23), the clouds in the simulations with radiation are significantly deeper and also produce thicker clouds. Another interesting difference can be seen when we look at the cloud size distribution in fig. 3.24 where we find that the "no-radiation" simulation produces more smaller clouds whereas significantly larger cloud patches form in the simulations with radiation. Amplified, three-dimensional, thermal cooling in the cloud's outer shell region leads to a yet increased horizontal buoyancy gradient and further boosts cloud growth. We may therefore conclude that interactive radiation and especially so three-dimensional radiative transfer leads to an enhancement of convection, producing fewer but larger, deeper and thicker clouds.

Three-dimensional radiative transfer effects in the thermal and solar spectral range offset one another for the most part, i.e. do not introduce a strong bias. Although thermal cooling is increased we also find an increase in solar absorbed energy. That being said, we find changes in the evolution of individual clouds because the cooling and heating takes place at different locations. We should record that simulations with the TenStream solver produce a higher liquid water path, and horizontally extended clouds while the cloud fraction is actually slightly less than in the simulation with one-dimensional radiative transfer.

3.2.2 Evolution of a Shallow Cumulus Cloud Field with an Interactive Surface Model

In analogy to the warm-bubble simulations I performed the preceding shallow cumulus cloud simulations also with a coupled interactive surface model. The surface model leads to a significantly higher latent- and sensible heat flux compared to the bulk flux formulation with the fixed sea surface temperature. That in turn leads to a faster cloud development and instead of 6 h for the initial run and the 12 h in total, the simulation here is only run for 2 h. The various simulations are then restarted from that point on and run up to a total time of 6 h. As before, the surface model parameters are chosen to mimic grasslands supported by a moist loamy ground, characteristic for European pasture landscape (see section 4.3 for detailed namelist parameters). In the "no-radiation" simulation, the average surface radiative flux is fixed to 348 $\mathrm{W\,m^{-2}}$, which is the average surface irradiance of the Twostream simulation from 2 h to 6 h. The other input parameters are the same as for the simulation without surface model.

The enhanced surface fluxes invigorate the boundary layer mixing. After only 2 h of model time, we find the depth of the mixed layer to have grown to 800 m (see fig. 3.25). If we compare the liquid water path in the simulations with surface model in fig. 3.26 to the simulation with a fixed sea surface temperature (fig. 3.19), it is clear that the enhanced surface fluxes lead to an increased total liquid water content. Also, the cloud fraction does not level out at 12 % but rather rises continuously up to about 50 % after only 6 h of model time. Especially the simulation with the TenStream solver produces more cloud water. These rather large differences are not

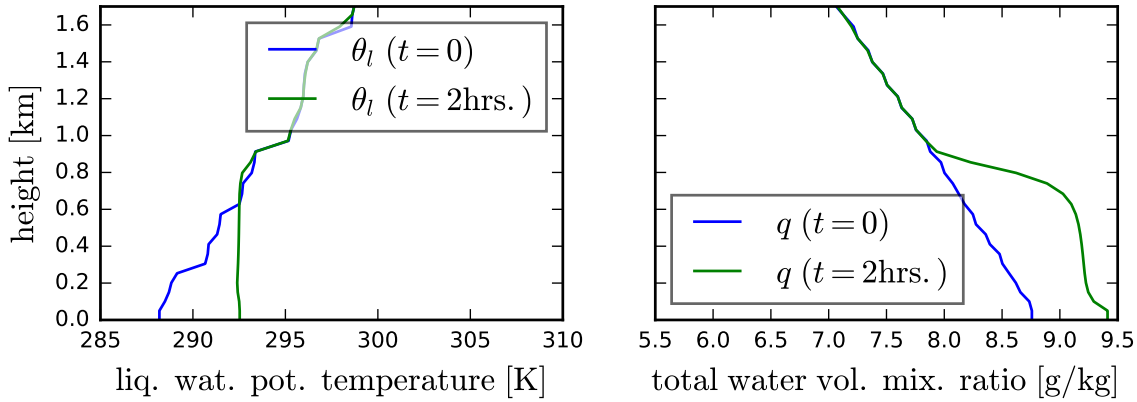

Figure 3.25: Initial vertical profiles of potential temperature and total water mixing ratio at time t=0 h where the Twostream simulation is started and at t=2 h from which point in time we will restart the other experiments. During the first 2 h, the simulation develops a well mixed layer up to 850 m and the lower atmosphere is considerable moistened by surface evaporation.

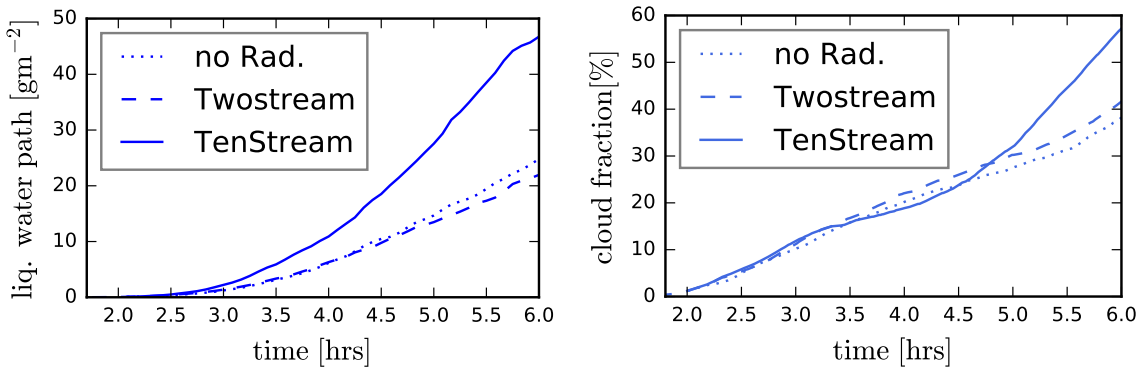

Figure 3.26: Shown on the left, a time-series of the liquid water path for the shallow cumulus cloud field simulations which include an interactive surface model. On the right, the average liquid water cloud fraction in the domain. The simulations with the TenStream solver develop more than twice as much liquid water.

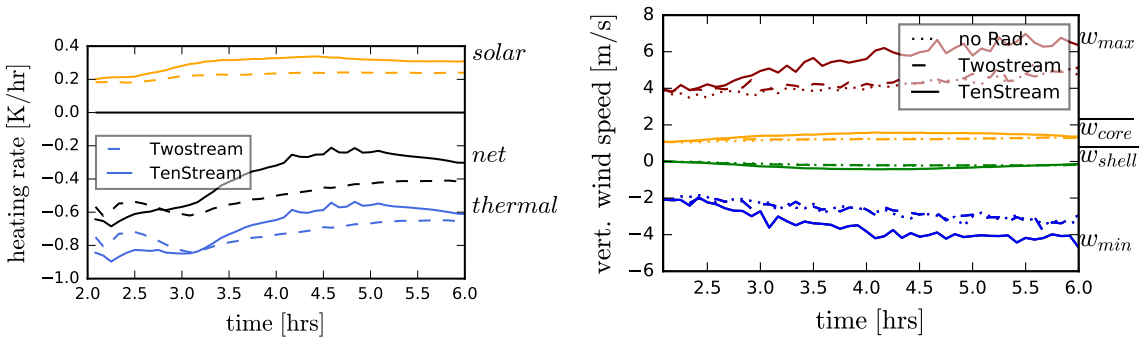

Figure 3.27: Shallow cumulus cloud field experiments with an interactive surface model: The figure shows the conditionally sampled mean radiative heating rate at cloudy voxels on the left and, on the right the minimum, maximum vertical velocities as well as the mean cloud core and cloud shell vertical wind speed. Core and shell are conditionally sampled according to LWC>0 and vertical velocity w $>$ .5 or w $<$ .5 respectively. Three dimensional radiative transfer shows stronger solar heating and weaker thermal cooling than in the one-dimensional case. The net radiative cooling of clouds is significantly reduced in the case of three-dimensional radiative transfer. Interactive three-dimensional radiation leads to significantly larger magnitudes in vertical velocities.

surprising if we recollect the results of the second warm-bubble experiment which coupled radiative transfer to the interactive surface model (section 3.1.2). There, three-dimensional radiative transfer lead to a constant supply of warm and moist air from beneath the cloud and showed to have a significant impact on the cloud's evolution.

One particular interesting feature is that, after about one hour, the TenStream solver simulation leads to a reduced thermal cooling rate. In fig. 3.27, left panel, we see that, for the first half hour, the thermal cooling rate is, as expected, larger in the case of three-dimensional radiative transfer. However, after hour three, the simulation changes and the Twostream simulation actually shows larger cooling rates. So, how come that three-dimensional thermal radiative transfer produces less cooling than the Twostream solver? Something must be going on with the structure of the clouds. If we take a look at the overview images of the scene (fig. 3.28), it becomes clear that the clouds seem to develop differently. Even at t=4 h, judging by eye, we may recognize that the Twostream run produces more smaller clouds than the "no-radiation"-run with the largest clouds in the case of the TenStream solver. In the case of the TenStream solver, we may also recognize a pattern that clouds form in bands perpendicular to the sun's direction. Additionally, we find that clouds are larger, more organized and further apart from each other. The latter is also visible in cloud fraction graph in fig. 3.26 between hours 3.5 h and 4.5 h. The organization and thus, increasingly compact cloud structure, lead to a reduced net radiative cooling.

The enhanced cloud development could of course be just a bias effect due to an increase in net surface irradiance in the case of the TenStream solver. However, if we examine the net radiative energy uptake at the surface in fig. 3.30a, it is clear that this is not the case. Net surface irradiance is equivalent for both the radiation

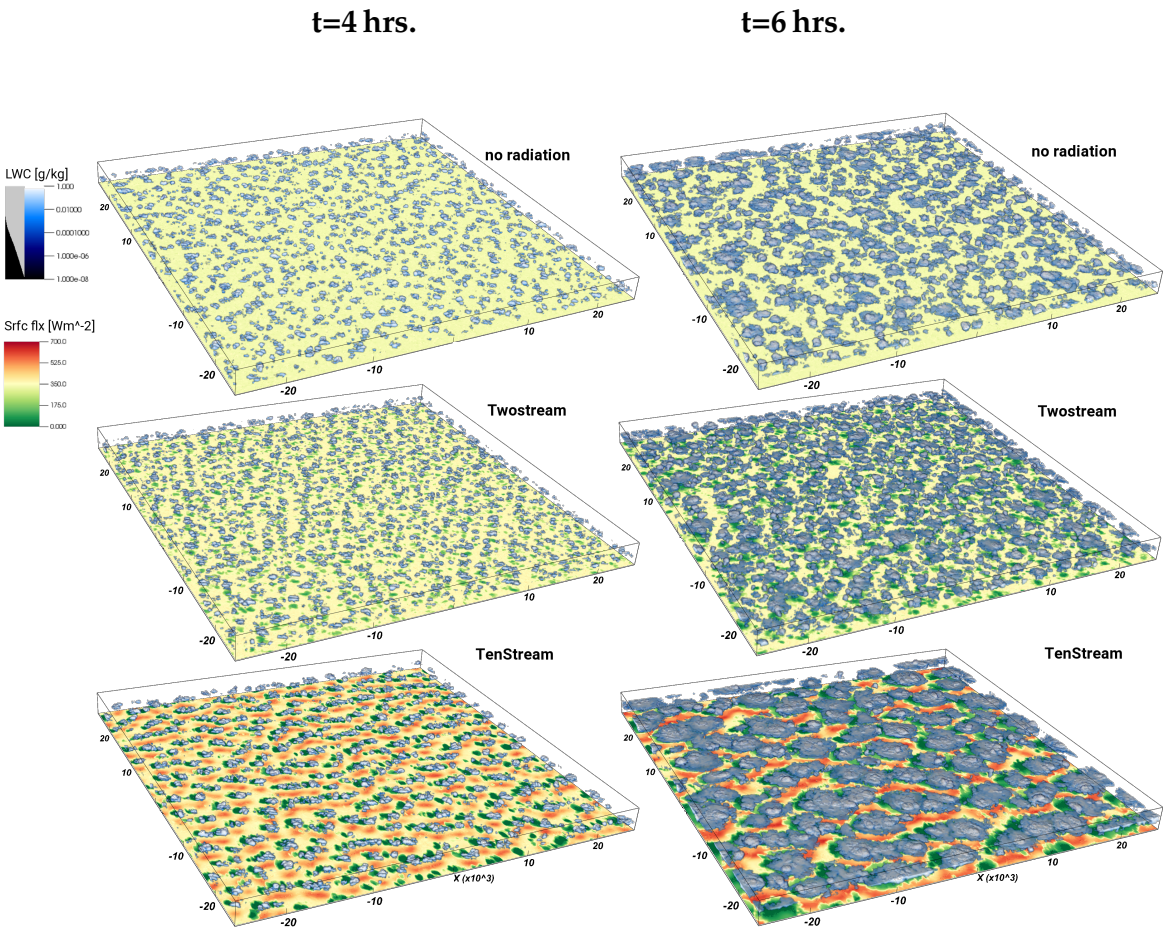

Figure 3.28: Shallow cumulus cloud field experiments with an interactive surface model: Volume rendered perspective on liquid water content and surface fluxes at t=4 h on the left and at t=6 h on the right. The surface flux is the combined latent and sensible heat flux. The sun is shining from the south (here from the bottom). At 4 h, the directional dependence of the TenStream solver already shows to organize the clouds in patterns perpendicular to the sun.

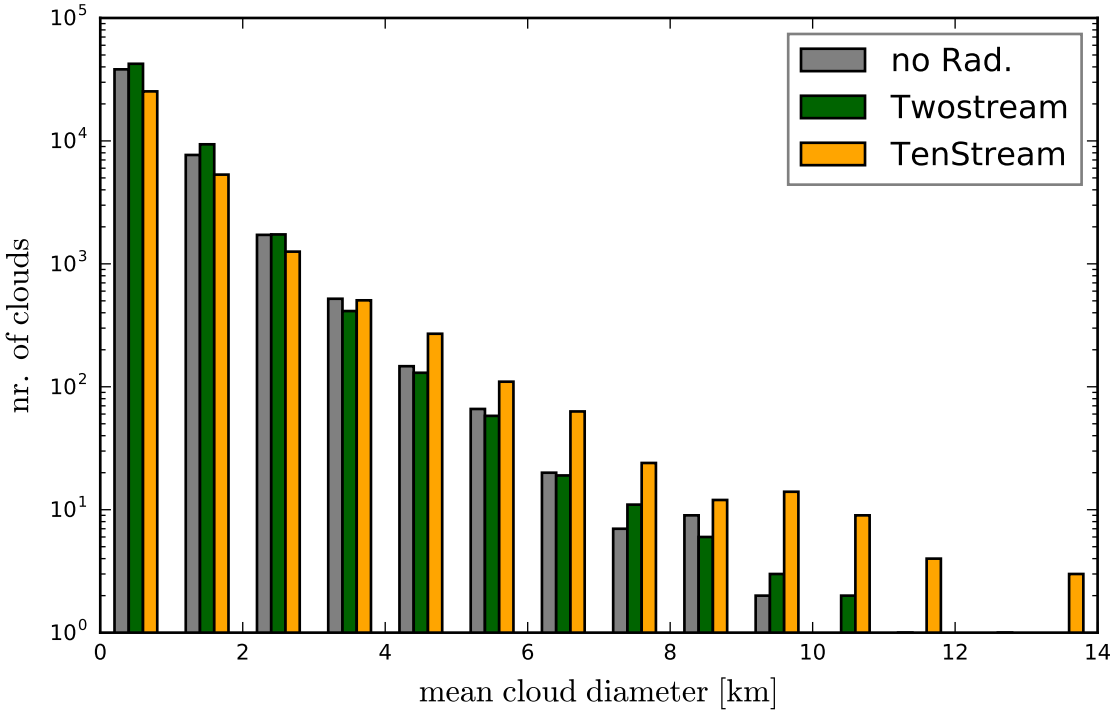

Figure 3.29: Cloud size statistics derived from liquid water path for the simulations including an interactive surface model. Cloud distribution is computed every 5 min from 2 h to 6 h. Cloud clusters are uniquely labeled for all areas that are consecutively connected through a 5-point stencil. The simulation with the Twostream solver produces more of the smaller clouds whereas we do find considerable larger clouds in the simulations with the TenStream solver.

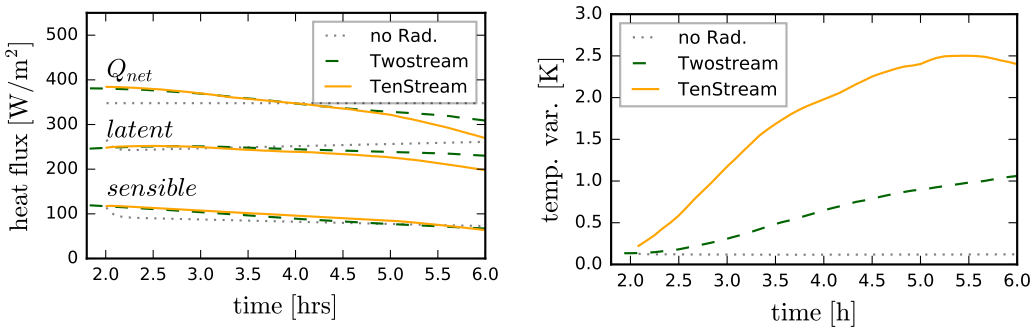

(a) surface energy fluxes

(b) skin temperature variability

Figure 3.30: Shallow cumulus cloud field experiments with an interactive surface model: Left panel depicts the horizontally averaged incident net flux Q with the corresponding latent and sensible heat fluxes. The right panel present the temperature variability of the skin layer. Net irradiance at surface is reduced over time due to an increase in cloud fraction. Differences between the Twostream and the TenStream solver are minor for the most part. The average net irradiance of the "no-radiation" run is set to match the one from the Twostream simulation. Interactive radiation produces an increasing amount of skin temperature variability whereas dynamical effects in the "no-radiation" run only introduce minor variability.

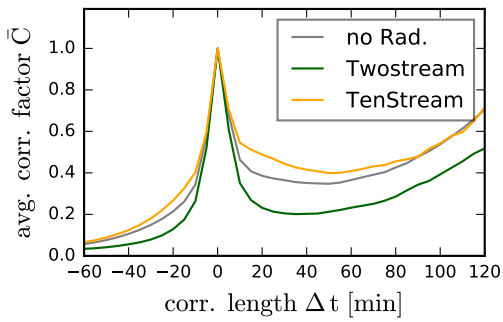

(a) Time-correlation of liquid water path according to eq. (3.1).

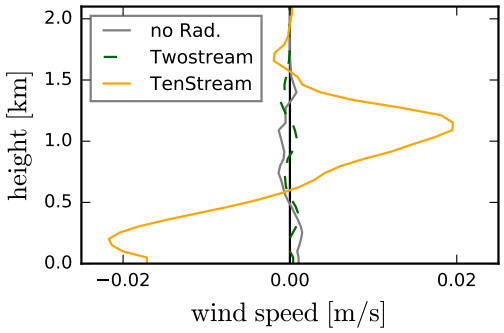

(b) Mean horizontal S-N wind component for the shallow cumulus cloud field simulation.

Figure 3.31: Time-series of the shallow cumulus cloud field simulations with interactive surface model. The "no-radiation" and TenStream simulation show more persistent and continuous clouds compared to the Twostream case. Correlation coefficients are averaged over the timespan of the simulation from 2 h to 6 h. The horizontal wind shear that is depicted in the right panel is induced by the differential heating at the illuminated cloud face versus shadowy regions. The circulation consists of a wind towards the sun at lower levels and away from the sun at the height of cloud.

simulations up until t=5 h and thus cannot be the source of the different course of the simulations.

As we argue already for the warm-bubble experiments in section 3.1.4 we find that the surface model introduces a "temperature-memory" effect. Figure 3.30b shows that the TenStream solver introduces one order of magnitude more surface temperature variability into the model than the one-dimensional radiative transfer. The increase in temperature variability for the TenStream simulation is consistent with the idea that the off-zenith sun illuminates the spot right beneath the cloud which constantly fuels the updraft with moist and warm air and so amplifies the cloud's lifetime. The Twostream solver on the other hand produces a skin temperature variability by casting the shadow of the cloud always directly beneath the cloud itself and therefore reduces surface fluxes in the updraft region.

With the goal to describe the longevity of clouds in a statistical sense, we may have a look at the time-correlation of the liquid water path and see if we find evidence that three-dimensional radiative transfer prolongs the cloud's lifetime. In other words, consider a cloudy pixel, what is the chance that it is still cloudy in the next time-step? The average time-correlation coefficient $\overline{C}$ is averaged over times t_i for various time delays Δt according to:

$$\overline{C} = \frac{1}{N}\sum_{i=1}^{N} C(t_i, \Delta t) = \frac{1}{N}\sum_{i=1}^{N} \frac{\sum\left(LWP(t_i + \Delta t) \cdot LWP(t_i)\right)}{\sum LWP(t_i)^2} \tag{3.1}$$

Figure 3.31a then shows the correlation coefficient averaged over the duration of the simulation with varying time-intervals. The asymmetry with regards of negative and positive time-intervals tells us that we have an overall trend that the clouds are

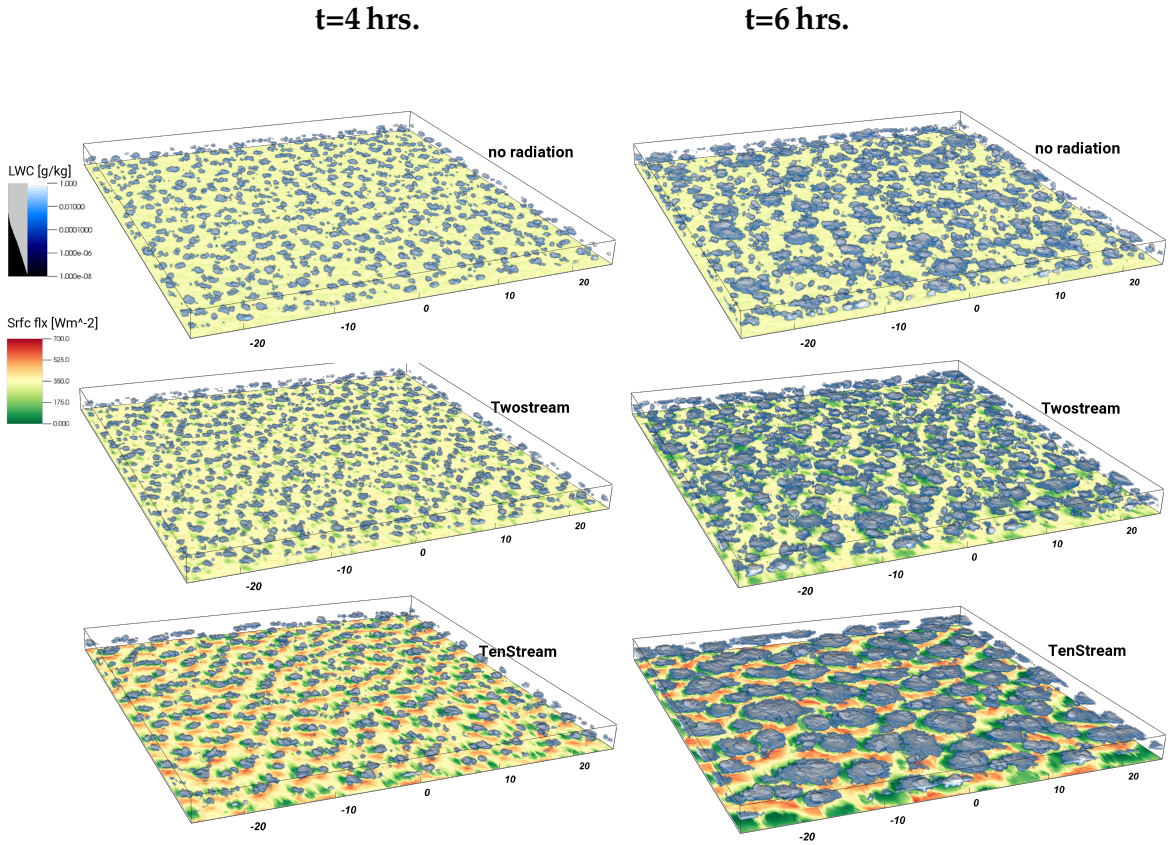

Figure 3.32: Volume rendered perspective on liquid water content and surface fluxes of the shallow cumulus cloud field simulations with interactive surface and a horizontal wind profile. The left panel shows the simulations at at $t = 4$ hrs and at $t = 6$ hrs on the right. The surface flux is the combined latent and sensible heat flux. The sun is shining from the east (here from the bottom right). At 4 h, the directional dependence of the TenStream solver already shows to organize the clouds in patterns perpendicular to the sun. The west-wind moves the clouds towards the sun.

growing. The higher correlation coefficient in the "no-radiation" and TenStream simulations, tells us that clouds, once formed, are more likely to stay there and live longer.

We already discussed the overturning circulation due to differential radiative heating in the preceding section 3.2.1. Now, including the three-dimensional effects of the horizontally displaced shadowing and increased surface fluxes beneath the cloud we find that the induced horizontal wind shear is pronounced even more. Figure 3.31b clearly shows the radiatively induced horizontal wind. At the lower levels from north to south, towards the sun and in the upper cloud layers, the opposite direction, away from the sun.

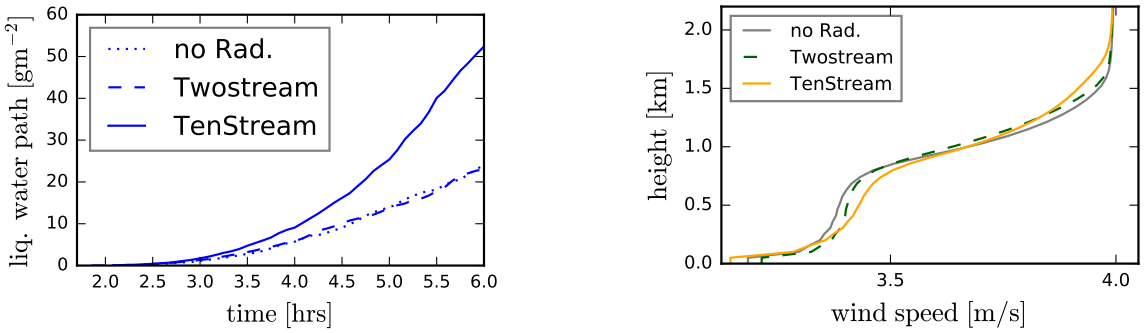

Figure 3.33: The left panel presents the domain averaged liquid water path. The TenStream run shows greatly increased production of liquid water while the Twostream and the "no-radiation" simulations show an equivalent amount of cloud water. The right panel shows the averaged horizontal E-W wind component for the shallow cumulus cloud field simulation with interactive surface model and horizontal background wind. The profiles are average over a timespan from 2 h to 6 h. The differential heating in the case of the TenStream radiative transfer solver enhances the circulation and induces a wind towards the sun at lower levels and away from the sun at the height of the cloud.

3.2.3 Evolution of a Shallow Cumulus Cloud Field with an Interactive Surface Model and a Horizontal Wind Profile

The preceding section, discussing the simulation of a shallow cumulus cloud field with an interactive surface, clearly shows significant differences in the evolution of the cloud field depending on which radiative transfer solver is used. However, as we already stated in the discussion of the warm-bubble experiments, in nature, we usually have a horizontal wind field which will smooth out the local effects of the differential surface heating. The warm-bubble experiment led us to the conclusion that the horizontal wind mitigated most of the three-dimensional effects but the simulations retained some "temperature-variability-memory" beyond the lifetime of the single cloud. This section tries to answer the question if the local variability in surface heating accumulates and changes the cloud evolution quickly enough even in the presence of a mean background wind profile. To that end, I repeat the simulations with the interactive surface model as in section 3.2.2, but this time with a horizontal background wind profile. The initial horizontal wind u is set according to a power law:

$$u(z) = \left(\frac{z}{1km}\right)^{1/7} \cdot 3\frac{m}{s}$$

which results in a wind speed of 3.5 m s^{-1} to 4 m s^{-1} between cloud base and top. The sun is shining from the east with a solar zenith angle of 60°.

Figure 3.32 again gives a overview of the simulations at 4 h and 6 h. Compared to the simulation without a horizontal wind profile, we find the surface flux variability to be reduced, yet still visible. The clouds still show enhanced growth and still seem to organize perpendicular to the sun direction.

Without going too much into the details of the simulation with a background wind profile, we find all the same mechanisms to be present in this set of simu-

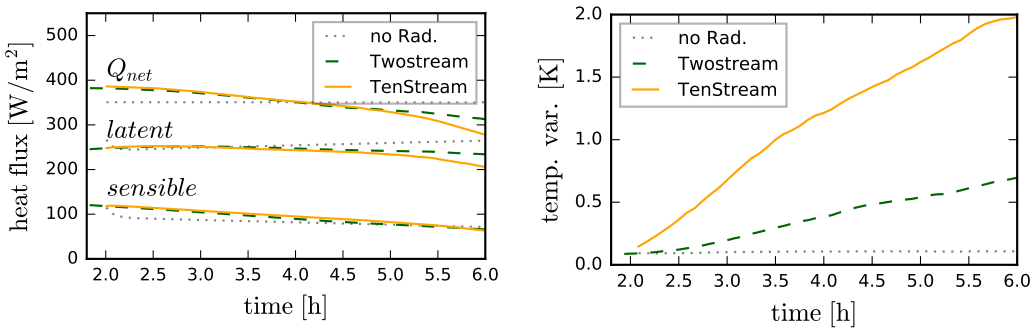

(a) surface heat fluxes

(b) skin temperature variability

Figure 3.34: Shallow cumulus cloud field experiments with an interactive surface model and horizontal wind: Left panel depicts the horizontally averaged incident net flux Q with the corresponding latent and sensible heat fluxes. The right panel present the temperature variability of the skin layer. Net irradiance at surface is reduced over time due to an increase in cloud fraction. Differences between the Twostream and the TenStream solver are minor for the most part. The average net irradiance of the "no-radiation" run is set to match the one from the Twostream simulation. Interactive radiation produces an increasing amount of skin temperature variability whereas dynamical effects in the "no-radiation" run only introduce minor variability.

lations. For example, in fig. 3.33 we see that the overall produced liquid water is increased by a factor of two for the TenStream run. Considering the fact that the liquid water path for the Twostream run develops at the same rate as in the "no-radiation" run, it seems that the horizontal wind, at least partly, compensates the cloud growth reducing effect that the one dimensional radiation solver had because of "self-shadowing". If we compare the skin temperature variability (fig. 3.34b) with the one presented earlier (simulations without the mean horizontal wind, see fig. 3.30b), we should record that the temperature variability is reduced by one order of magnitude through the horizontal wind, but is nevertheless present. Additionally, in the case of the TenStream run, we find the same radiatively induced circulation pattern which manifests itself in the mean horizontal wind speed (see fig. 3.33). The differential heating increases the wind towards the sun in the lower levels and in the opposite direction at cloud level heights.

3.2.4 Discussion on the Shallow Cumulus Cloud Field Experiments

The preceding section examines the cloud-radiative feedback mechanisms for a shallow cumulus cloud field. We examine three experiments in close analogy to the warm-bubble case study. The first experiment considers radiation only in the atmosphere whereas surface fluxes are only dependent on the surface temperature gradient and wind-speed. The second experiment uses an interactively coupled surface model. The warm-bubble experiments suggested that a horizontal background wind may mitigate the effects that three-dimensional radiative transfer has.

To that end we run a third experiment and examine the implications of a horizontal wind profile. At this point we may summarize the key findings of the shallow cumulus cloud field simulations as follows:

Cumulus experiment with radiative heating only in the atmosphere:

- Thermal radiative transfer leads to a cooling of the outer shell of clouds. This increases the local horizontal buoyancy gradient and enhances core updraft velocities. Three-dimensional radiative transfer enhances these effects through cloud-side cooling.
- Solar radiative transfer heats the core updraft regions of clouds and thus supports cloud development.
- Simulations with radiative heating produce deeper (vertically) and thicker clouds than simulations without interactive radiation calculations.
- Differences between one- and three-dimensional radiative transfer show only small differences in net radiative heating of the atmosphere. Yet we find that the simulations with three-dimensional radiative transfer produces fewer but larger cloud patches.
- Three-dimensional solar radiative heating strengthens a circulation pattern where air rises on the illuminated cloud side and descends on the shadowy side. This introduces a horizontal wind towards the sun at lower levels and with the opposite direction, away from the sun, at cloud height.

Cumulus experiment with radiation interactively heating the surface:

- In the case of one-dimensional radiative transfer and an interactive surface model we find a decreased cloud lifetime. The shadow that the clouds cast beneath themselves weakens the updraft and clouds consequently dissolve quicker.
- Three-dimensional radiative transfer displaces the cloud shadow and results in a local maximum in surface irradiance directly beneath the cloud. This excess energy in the updraft region constantly supports the cloud development with warm and moist air. As a consequence, we find the TenStream simulation to produce deeper, thicker and larger clouds.
- We observe that three-dimensional radiative transfer organizes the clouds in band structures perpendicular to the sun's orientation.
- The displacement of the surface shadow with three-dimensional radiative transfer further enhances the earlier observed circulation pattern.
- While the net surface energy uptake of both, the one- and the three-dimensional radiative transfer simulations, show to be unbiased, we find that the TenStream simulation introduces a significantly larger temperature variability. This may indicate the reason for the enhanced organization that is found in cloud structures.

Cumulus experiment with interactive surface model and an initial horizontal wind profile:

- A horizontal wind smooths the influence of radiative-surface interactions. The temperature variability is decreased by one order of magnitude but still present.
- The "self-shadowing" effect that is apparent with one-dimensional radiative transfer is partly mitigated.
- Simulations with three-dimensional radiative transfer still show the circulation pattern towards the sun superimposed on the background wind profile.
- Albeit diminished, we find that the TenStream simulation still shows to organize clouds in bands perpendicular to the sun's direction.
- Three-dimensional radiative heating produces more than twice the amount of liquid water despite the horizontal wind.

The shallow cumulus simulations conducted here give an introduction to the effects of radiative heating on cloud dynamics. We find particularly large differences in the case where we use the three-dimensional TenStream solver in conjunction with the interactively coupled surface model. The findings listed above generally agree well with the findings of Guan et al. [1997] and Klinger [2015] concerning the thermal radiative transfer. Particularly the observed wind pattern that is induced by the asymmetric solar heating agrees well with the work of Wapler [2007].

Clearly, there are still many unanswered questions. An outlook for future research is given in section 4.3. However, by now, you should be convinced that radiative transfer can have a fundamental influence on the evolution of clouds.

Chapter 4

Summary and Conclusions

This dissertation presents research on the intricate linkage between radiation, the atmosphere, the surface, and clouds, with a special emphasis on three-dimensional radiative transfer effects. This chapter will give a short overview of the manuscript: the herein developed methods, the conducted experiments, and the conclusions drawn from these experiments. At the end, we will find an outline of some ideas about future research and experiments that may further our understanding of cloud-radiative processes.

4.1 Summary

The goal of this study is to gain insight into cloud-radiative feedback mechanisms and what role three-dimensional radiative transfer effects play in the evolution of convective clouds. We know from several other studies [O'Hirok and Gautier, 2005, Wapler and Mayer, 2008, Wissmeier et al., 2013] that the usually employed one-dimensional radiative transfer solvers introduce considerable local errors in surface and atmospheric heating rates. Those studies assessed the errors only for single snapshots of cloud fields, i.e. only instantaneous errors in the temperature tendencies. However, if we truly want to answer the questions of "if" and "how" radiative transfer influences clouds we need to consider the non-linear feedbacks. To that end, a radiative transfer solver is needed which accurately incorporates three-dimensional effects and is computationally fast enough to be run in tandem with a cloud resolving model. In the past, numerous such approximations were developed with varying success. The introductory chapter (section 1.4) of this work highlights achievements and shortcomings of the various methods that were proposed. In conclusion, so far, there was no silver bullet that would solve the task at hand — namely, compute three-dimensional radiative heating rates in the atmosphere — fast enough to be coupled interactively.

Naturally, the first milestone of this work was to develop a new suitable method for the radiative transfer computations. Chapter 2 presents the TenStream solver — a new approach to solving the radiative transfer equation in three-dimensional inhomogeneous participating media which is accurate, parallelizable on modern compute architectures yet orders of magnitude faster than rigorous three-dimensional radiative transfer solvers like Monte Carlo or SHDOM. The TenStream

solver has been coupled to the cloud resolving atmospheric model, the UCLA–LES. A considerable amount of work has been put into the characterization of the accuracy of the TenStream solver and its runtime characteristics, especially with respect to the parallel scalability on todays super-computers.

Chapter 3 presents two sets of numerical experiments to examine the effects of radiative transfer on the evolution of clouds, and particularly the impact of three-dimensional radiative transfer. Both sets of experiments compare simulations with no radiation computations at all, to simulations with the Twostream solver which neglects horizontal energy transfer, and with the TenStream solver.
The first set of experiments in section 3.1 examine the evolution of a single, artificially forced, convective cloud. To disentangle the various feedbacks between cloud dynamics and radiative heating, three simulations are performed.
The first simulations (section 3.1.1) consider radiative heating or cooling only in the atmosphere. Absorption or emission at the surface is kept constant for the sake of simplicity. However, it is obvious that three-dimensional radiative transfer tremendously alters the local distribution of surface fluxes.
Naturally, the second set of simulations (section 3.1.2) uses an interactive surface model that links radiative transfer to the latent and sensible-heat fluxes at the surface. Horizontal wind is expected to smooth the effects that are introduced by radiative heating. Consequently, the third set of simulations (section 3.1.3) further introduces a horizontal wind profile to examine if three-dimensional radiative transfer has a persistent effect on the structure of the atmosphere.

In the second set of experiments in section 3.2, we extend the simulation from one convective plume to many over a longer period of time (hours). The simulations examine the influence of radiative transfer on a shallow cumulus cloud field, 50 km by 50 km in size. The second set of experiments is conducted in close analogy to the first one, in that we compute the simulations with the Twostream solver, the TenStream solver and without interactive radiation calculations. The simulations are also done for atmospheric heating only (section 3.2.1), with a coupled interactive surface model (section 3.2.2), and additionally with a superimposed horizontal wind profile (section 3.2.3).

4.2 Conclusions

At this point, let us recapitulate the key findings in this work. The novel TenStream solver is able to compute three-dimensional radiative heating rates in the atmosphere and compared to traditionally employed one-dimensional radiative transfer solvers, significantly reduces errors in atmospheric and surface heating rates. The accuracy of the TenStream solver is validated against Monte Carlo benchmark simulations and shows approximately 20 % relative root-mean-squared-error for a wide range of cloud scenes. A limited knowledge of microphysics and optical properties, or the method of the spectral integration introduces errors that are comparable to those of the TenStream solver. Although the TenStream method is flexible enough that it could be used to achieve higher accuracy (using more streams) for the cost of additional computational time it seems that using ten streams for the discretization of radiation is a sweet spot for our intents.

The advent of high performance computing allows the scientific community to simulate, ever increasing, larger domains on higher resolutions, considering physical processes with higher accuracies. However, the increasing performance of supercomputers is achieved primarily through massive parallelization. This trend necessitates the development of algorithms that may scale on modern hardware architectures. Parallel scalability was a primary concern developing the TenStream solver. Rigorous tests reveal that the performance, compared to one-dimensional solvers, depends on the memory bandwidth of the machine, the solar zenith angle, the resolution of the simulation and the complexity of the cloud field. Specifically the solar zenith angle and the resolution determine the "interaction-radius" of a cloud, e.g. how far in terms of pixels, the shadow is cast and thus how much communication between processors has to be done. It became clear that in order to reach acceptable parallel scaling behavior one needs to apply some form of multigrid matrix preconditioning. This means we solve the radiative transfer problem on several cascaded meshes simultaneously to reduce communication efforts. Section 2.2 shows the TenStream solver to excel with a parallel weak scaling efficiency of up to 90 % when it is run on 4096 cores. Under realistic conditions, we find that the TenStream solver is a factor of 5 to 10 more expensive than a Twostream solver. The question we initially set out to answer was:

> "Do effects of three-dimensional radiative transfer have an influence on the development and evolution of clouds and if so, how?"

Concluding from the results of the experiments with the UCLA–LES in chapter 3, I think we can safely answer the "if" with a clear "yes". The "how" part is a much trickier question. We find that the differential solar radiative heating between the illuminated cloud face and the shaded side induces a circulation that alters the shape and evolution of clouds. This overturning circulation does not fundamentally change the cloud's lifetime but nevertheless changes the state of the atmosphere through feedbacks in the cloud dynamics. We find these changes to accumulate if we look at longer time periods of several hours spanning the life time of several cumulus clouds. Considering that one-dimensional radiative transfer produces local errors in surface irradiance of several hundred $\mathrm{W\,m^{-2}}$, it is not surprising that the simulations are highly affected if we couple radiative transfer to an interactive surface model. We find that the horizontal displacement of the cloud's shadow has a profound impact on the circulation pattern in the atmosphere. The earlier mentioned overturning circulation is pronounced much stronger. Especially the contrast between one-dimensional and three-dimensional radiative transfer shows a significantly different evolution of the simulations. Whereas the Twostream solver casts the cloud's shadow directly beneath it and thus cuts off the inflow of moist and warm air, we find that the TenStream allows to further heat the updraft region and consequently prolongs and intensifies the cloud. The lifetime of the single, convective, warm-bubble cloud is approximately doubled. The shallow cumulus cloud field simulations consistently show an increase of the liquid water path by a factor of two or more over the course of four hours.

Given the strong impact we may wonder — is this actually a realistic setup? We rarely find the atmosphere to be still and we would certainly expect to have some form of a horizontal wind! It is also clear that when we move a cloud horizontally,

the influence of radiation at the surface would be smoothed. To that end, each experiment is repeated with a horizontal wind profile. Indeed, once we introduce a horizontal wind to the warm-bubble experiment, we find that the wind mitigates most effects of three-dimensional radiative transfer. However, we find a residual signature in the surface temperature beyond the end of the warm-bubble simulation. This setup with a directional dependence of the wind does introduce a new parameter: the angle between the wind direction and the solar radiation. To make it even more complicated, it turns out that the magnitude of three-dimensional effects depends on that as well.

The shallow cumulus cloud field experiment reveals that, while the horizontal wind smooths the surface temperature variability, the TenStream simulation still shows a significantly different evolution than the ones without or with one-dimensional radiative transfer. This means that the surface gives the radiation a memory to persist beyond the lifespan of one cumulus cloud. Interestingly, the one-dimensional effect of "self-shadowing" and the corresponding diminished cloud growth is at least partially removed by the introduction of a horizontal wind. This leads us to the conclusion that this memory effect strongly depends on the wind velocity, on the cloud height and the solar zenith angle.

From the fact that the solar azimuth plays an important role in conjunction with the mean wind field leads me to the conclusion that there might not be an easy answer to the earlier posed question regarding the "how". However, even if the final answer seems to be far away, we may yet find comfort in the fact that the TenStream makes a powerful ally in disentangling cloud-radiative feedbacks.

4.3 Outlook

Although we have learned a lot about the linkage between radiative transfer and the evolution of clouds, many questions have yet to be answered.

Personally, I find the organization of clouds perpendicular to the incident solar radiation very exciting. Further studies will have to examine the sensitivity of these patterns to surface properties, the zenith angle and especially the background wind speed. The wind shear should at one point mitigate the effects of the radiatively induced temperature variability. At the same time, the heat capacity of the surface layer will also have a smoothing effect. Especially the regime of marine cumulus clouds is of great importance to constrain climate simulations. It would be great to study the degree of organization with respect to these three parameters. Characterizing those sensitivities will hopefully guide us to where we should look for this kind of cloud organization in the real world.

There are many more parameters that may influence the cloud-radiative feedback. For one, we may ask, how do the results of this work depend on the initial conditions of the atmosphere (e.g. the temperature and moisture profile)?

Numerical weather models often produce too few variability which is of great importance to trigger convection. Hence, what is the effect of the increased temperature variability due to three-dimensional radiative transfer and how would it influence the diurnal cycle and the onset of precipitation?

The findings are surely regime dependent and should be evaluated for other

types of clouds such as deep convective clouds, or organized convection such as squall lines, frontal systems or tropical cyclones.

The question raised above can be answered using the tools developed here. For others, it may prove essential to rethink how we couple radiative transfer to our atmospheric models.

So far, we considered the radiative heating to only act on the mean temperature of a voxel. Roach [1976] however proposes, that thermal cooling acts directly on liquid droplets, quickly changing the supersaturation with respect to the surrounding air, and thus increases droplet growth rates. Consequently, we should ask, how may changes in radiative-heating rates feed back on cloud droplet microphysics? How would that influence the formation of rain and change the course of the simulations? Furthermore, what is the interplay between three-dimensional radiative transfer, aerosols or other hydro-meteors such as ice clouds? Atmospheric chemistry non-linearly depends on photolysis rates and whether particles are in a wet or dry environment. Given that some chemical processes react on very fast timescales, how would the increased variability of three-dimensional radiative transfer change chemical reaction rates?

Two research projects will carry on the work that has begun here. The Transregional Collaborative Research Center "Waves to Weather" (W2W) investigates the root causes for errors in weather prediction. The key concept evolves around the idea that, over time, errors grow from small to larger scales. One aspect that will be examined is the error-growth-rate of radiative heating errors from cloud scales (tens of meters) to convective scales (km-range) to synoptic scales (hundreds of km).

At the same time, the "**H**igh **D**efinition **C**louds and **P**recipitation for **C**limate **P**rediction", the HD$(CP)^2$ project will continue the effort to improve our understanding of cloud-radiative processes through high-resolution modeling with the goal to enhance parameterizations for climate prediction. This will involve the implementation of the TenStream solver in the new ICON model [Dipankar et al., 2015] and run weather hindcasts with three-dimensional radiative transfer in a realistic setup.

Appendix

Input parameters for the PETSc solvers

Listing 4.1: BiConjugate-Gradient-Squared iterative solver. The block-jacobi preconditioner does a Incomplete LU preconditioning on each rank with fill level 1 independent of its neighbouring ranks

```
-ksp_type bcgs
-pc_type bjacobi
-sub_pc_type ilu
-sub_pc_factor_levels 1
```

Listing 4.2: Flexible GMRES solver with algebraic multigrid preconditioning. Use plain aggregation to generate coarse representation (dropping values less than .1 to reduce coarse matrix complexity) and use up to 5 iterations of SOR on coarse grids

```
-ksp_type fgmres
-ksp_reuse_preconditioner
-pc_type gamg
-pc_gamg_type agg
-pc_gamg_agg_nsmooths 0
-pc_gamg_threshold .1
-pc_gamg_square_graph 1
-mg_levels_ksp_type richardson
-mg_levels_pc_type sor
-mg_levels_ksp_max_it 5
```

CodeAvailability

The UCLA–LES model is publicly available at https://github.com/uclales. The calculations in section 2.2 were done with the modified radiation interface which is available at git-revision: "bbcc4e0" Calculations in chapter 3 were done with the UCLA–LES model at version: "599d91b"

The TenStream model is publicly available at https://github.com/tenstream. Section 2.2 used the TenStream model at git-revision: "e0252dd". Calculations in chapter 3 were done with the TenStream model at version: "1611855".

The model repositories are also archived at the Leibnitz-Rechen-Zentrum as part of the daily user-home backups.

For the sake of reproducibility I provide the input parameters for the UCLA–LES computations along with the TenStream sources.

Bibliography

B. A. Albrecht, C. S. Bretherton, D. Johnson, W. H. Scubert, and A. S. Frisch. The atlantic stratocumulus transition experiment-astex. *Bulletin of the American Meteorological Society*, 76(6):889–904, 1995. doi: 10.1175/1520-0477(1995)076⟨0889:TASTE⟩2.0.CO;2.

S. Balay, W. D. Gropp, L. C. McInnes, and B. F. Smith. Efficient management of parallelism in object oriented numerical software libraries. In E. Arge, A. M. Bruaset, and H. P. Langtangen, editors, *Modern Software Tools in Scientific Computing*, pages 163–202. Birkhäuser Press, 1997.

S. Balay, S. Abhyankar, M. F. Adams, J. Brown, P. Brune, K. Buschelman, V. Eijkhout, W. D. Gropp, D. Kaushik, M. G. Knepley, L. C. McInnes, K. Rupp, B. F. Smith, and H. Zhang. PETSc users manual. Technical Report ANL-95/11 - Revision 3.5, Argonne National Laboratory, 2014.

A. Bozzo, R. Pincus, I. Sandu, and J.-J. Morcrette. Impact of a spectral sampling technique for radiation on ecmwf weather forecasts. *Journal of Advances in Modeling Earth Systems*, 6(4):1288–1300, 2014. ISSN 1942-2466. doi: 10.1002/2014MS000386. URL http://dx.doi.org/10.1002/2014MS000386.

R. F. Cahalan, L. Oreopoulos, A. Marshak, K. F. Evans, A. B. Davis, R. Pincus, K. H. Yetzer, B. Mayer, R. Davies, T. P. Ackerman, et al. The i3rc: Bringing together the most advanced radiative transfer tools for cloudy atmospheres. *Bulletin of the American Meteorological Society*, 86(9), 2005.

S. Chandrasekhar. *Radiative transfer*. Courier Corporation, 2013.

A. Dipankar, B. Stevens, R. Heinze, C. Moseley, G. Zängl, M. A. Giorgetta, and S. Brdar. A large eddy simulation version of icon (icosahedral nonhydrostatic): Model description and validation. *Journal of Advances in Modeling Earth Systems*, 2015.

C. Emde, R. Buras-Schnell, A. Kylling, B. Mayer, J. Gasteiger, U. Hamann, J. Kylling, B. Richter, C. Pause, T. Dowling, et al. The libradtran software package for radiative transfer calculations (version 2.0. 1). *Geoscientific Model Development*, 9(5): 1647–1672, 2016.

K. Evans and W. Wiscombe. Improvements to the shdom radiative transfer modeling package. In *Proc. 13th ARM Sci. Team Meeting*, 2003.

K. F. Evans. The spherical harmonics discrete ordinate method for three-dimensional atmospheric radiative transfer. *Journal of the Atmospheric Sciences*, 55(3):429–446, 1998. doi: 10.1175/1520-0469(1998)055⟨0429:TSHDOM⟩2.0.CO;2. URL http://dx.doi.org/10.1175/1520-0469(1998)055<0429:TSHDOM>2.0.CO;2.

J. W. Frame, J. L. Petters, P. M. Markowski, and J. Y. Harrington. An application of the tilted independent pixel approximation to cumulonimbus environments. *Atmospheric Research*, 91(1):127–136, 2009. doi: 10.1016/j.atmosres.2008.05.005. URL http://dx.doi.org/10.1016/j.atmosres.2008.05.005.

Q. Fu and K. Liou. On the correlated k-distribution method for radiative transfer in nonhomogeneous atmospheres. *Journal of the Atmospheric Sciences*, 49(22):2139–2156, 1992. doi: 10.1175/1520-0469(1992)049⟨2139:OTCDMF⟩2.0.CO;2.

H. Gerber, S. Malinowski, A. Bucholtz, and T. Thorsen. 9.3 radiative cooling of stratocumulus. *AMS Confex*, 2014.

H. Guan, M. K. Yau, and R. Davies. The effects of longwave radiation in a small cumulus cloud. *Journal of the Atmospheric Sciences*, 54(17):2201–2214, 1997. doi: 10.1175/1520-0469(1997)054⟨2201:TEOLRI⟩2.0.CO;2. URL http://dx.doi.org/10.1175/1520-0469(1997)054<2201:TEOLRI>2.0.CO;2.

L. Henyey and J. Greenstein. Diffuse radiation in the galaxy. *Astrophys. Journal*, 93: 70–83, 1941.

T. Heus, C. van Heerwaarden, H. Jonker, A. Pier Siebesma, S. Axelsen, K. van den Dries, O. Geoffroy, A. Moene, D. Pino, S. de Roode, et al. Formulation of the dutch atmospheric large-eddy simulation (dales) and overview of its applications, geosci. model dev., 3, 415–444, doi: 10.5194, 2010.

J. R. Holton and G. J. Hakim. *An introduction to dynamic meteorology*, volume 88. Academic press, 2012.

H. Iwabuchi. Efficient monte carlo methods for radiative transfer modeling. *Journal of the atmospheric sciences*, 63(9):2324–2339, 2006. doi: 10.1175/JAS3755.1.

F. Jakub. Parametrization of 3d radiative transfer effects on solar heating rates in nwp models using cascaded uniform filters on decomposed flux fields. unpublished thesis, January 2013.

F. Jakub and B. Mayer. A three-dimensional parallel radiative transfer model for atmospheric heating rates for use in cloud resolving modelsthe tenstream solver. *Journal of Quantitative Spectroscopy and Radiative Transfer*, (0):–, 2015. ISSN 0022-4073. doi: http://dx.doi.org/10.1016/j.jqsrt.2015.05.003. URL http://www.sciencedirect.com/science/article/pii/S0022407315001727.

F. Jakub and B. Mayer. 3-d radiative transfer in large-eddy simulations experiences coupling the tenstream solver to the ucla-les. *Geoscientific Model Development*, 9(4):1413–1422, 2016. doi: 10.5194/gmd-9-1413-2016. URL http://www.geosci-model-dev.net/9/1413/2016/.

S. Kato, T. P. Ackerman, J. H. Mather, and E. E. Clothiaux. The k-distribution method and correlated-k approximation for a shortwave radiative transfer model. *Journal of Quantitative Spectroscopy and Radiative Transfer*, 62(1):109–121, 1999. doi: 10.1016/S0022-4073(98)00075-2.

C. Klinger. Influence of 3d thermal radiation on cloud development. Dezember 2015. URL http://nbn-resolving.de/urn:nbn:de:bvb:19-190464.

K.-N. Liou, Q. Fu, and T. P. Ackerman. A simple formulation of the delta-four-stream approximation for radiative transfer parameterizations. *Journal of the atmospheric sciences*, 45(13):1940–1948, 1988.

A. Marshak and A. Davis. *3D radiative transfer in cloudy atmospheres*. Springer Science & Business Media, 2005.

A. Marshak, A. Davis, R. Cahalan, and W. Wiscombe. Nonlocal independent pixel approximation: direct and inverse problems. *Geoscience and Remote Sensing, IEEE Transactions on*, 36(1):192 –205, jan 1998. ISSN 0196-2892. doi: 10.1109/36.655329.

B. Mayer. Radiative transfer in the cloudy atmosphere. In *EPJ Web of Conferences*, volume 1, pages 75–99. EDP Sciences, 2009. doi: 10.1140/epjconf/e2009-00912-1.

B. Mayer, , and A. Kylling. Technical note: The libradtran software package for radiative transfer calculations-description and examples of use. *Atmospheric Chemistry and Physics*, 5(7):1855–1877, 2005. doi: 10.5194/acp-5-1855-2005. URL http://www.atmos-chem-phys.net/5/1855/2005/acp-5-1855-2005.html.

J. D. McCalpin. Memory bandwidth and machine balance in current high performance computers. *IEEE Computer Society Technical Committee on Computer Architecture (TCCA) Newsletter*, pages 19–25, Dec. 1995.

W. Meador and W. Weaver. Two-stream approximations to radiative transfer in planetary atmospheres: A unified description of existing methods and a new improvement. *Journal of the atmospheric sciences*, 37(3):630–643, 1980. doi: 10.1175/1520-0469(1980)037⟨0630:TSATRT⟩2.0.CO;2.

E. J. Mlawer, S. J. Taubman, P. D. Brown, M. J. Iacono, and S. A. Clough. Radiative transfer for inhomogeneous atmospheres: Rrtm, a validated correlated-k model for the longwave. *Journal of Geophysical Research: Atmospheres (1984–2012)*, 102 (D14):16663–16682, 1997. doi: 10.1029/97JD00237.

W. O'Hirok and C. Gautier. The impact of model resolution on differences between independent column approximation and monte carlo estimates of shortwave surface irradiance and atmospheric heating rate. *Journal of the atmospheric sciences*, 62 (8), 2005. doi: 10.1175/JAS3519.1. URL http://dx.doi.org/10.1175/JAS3519.1.

W. OHirok, P. Ricchiazzi, and C. Gautier. Incorporation of 3d shortwave radiative effects within the weather research and forecasting model. In *15th ARM science meeting proceedings. Daytona Beach, Florida*, pages 14–18, 2005.

E. W. Peterson and J. P. Hennessey. On the use of power laws for estimates of wind power potential. *Journal of Applied Meteorology*, 17(3):390–394, 1978. doi: 10.1175/1520-0450(1978)017⟨0390:OTUOPL⟩2.0.CO;2. URL http://dx.doi.org/10.1175/1520-0450(1978)017<0390:OTUOPL>2.0.CO;2.

J. L. Petters. The impact of radiative heating and cooling on marine stratocumulus dynamics. 2009.

R. Pincus and K. F. Evans. Computational cost and accuracy in calculating three-dimensional radiative transfer: Results for new implementations of monte carlo and shdom. *Journal of the Atmospheric Sciences*, 66(10):3131–3146, 2009.

R. Pincus and B. Stevens. Monte carlo spectral integration: A consistent approximation for radiative transfer in large eddy simulations. *Journal of Advances in Modeling Earth Systems*, 1(2), 2009. doi: 10.3894/JAMES.2009.1.1.

M. Rieck, C. Hohenegger, and C. C. van Heerwaarden. The influence of land surface heterogeneities on cloud size development. *Monthly Weather Review*, 142(10): 3830–3846, 2014.

M. Rieck, M. Claussen, and C. Hohenegger. *The role of heterogeneities and land-atmosphere interactions in the development of moist convection*. PhD thesis, Universität Hamburg Hamburg, 2015. URL https://www.mpimet.mpg.de/fileadmin/publikationen/Reports/WEB_BzE_167.pdf.

W. Roach. On the effect of radiative exchange on the growth by condensation of a cloud or fog droplet. *Quarterly Journal of the Royal Meteorological Society*, 102(432): 361–372, 1976. doi: 10.1002/qj.49710243207.

Y. Saad. A flexible inner-outer preconditioned gmres algorithm. *SIAM Journal on Scientific Computing*, 14(2):461–469, 1993.

Y. Saad. *Iterative methods for sparse linear systems*. Siam, 2003.

V. Savic-Jovcic and B. Stevens. The structure and mesoscale organization of precipitating stratocumulus. *Journal of the Atmospheric Sciences*, 65(5):1587–1605, 2008.

U. Schumann, A. Dörnbrack, and B. Mayer. Cloud-shadow effects on the structure of the convective boundary layer. *Meteorologische Zeitschrift*, 11(4):285–294, 2002.

J. Smagorinsky. General circulation experiments with the primitive equations. *Monthly Weather Review*, 91(3):99–164, 1963. doi: 10.1175/1520-0493(1963)091⟨0099:GCEWTP⟩2.3.CO;2. URL http://dx.doi.org/10.1175/1520-0493(1963)091<0099:GCEWTP>2.3.CO;2.

K. Stamnes, S.-C. Tsay, W. Wiscombe, and K. Jayaweera. Numerically stable algorithm for discrete-ordinate-method radiative transfer in multiple scattering and emitting layered media. *Applied optics*, 27(12):2502–2509, 1988.

K. Stamnes, S.-C. Tsay, W. Wiscombe, and I. Laszlo. Disort, a general-purpose fortran program for discrete-ordinate-method radiative transfer in scattering and emitting layered media: documentation of methodology. *Goddard Space flight center, NASA*, 2000.

B. Stevens, C.-H. Moeng, A. S. Ackerman, C. S. Bretherton, A. Chlond, S. de Roode, J. Edwards, J.-C. Golaz, H. Jiang, M. Khairoutdinov, et al. Evaluation of large-eddy simulations via observations of nocturnal marine stratocumulus. *Monthly weather review*, 133(6):1443–1462, 2005. doi: 10.1175/MWR2930.1.

G. K. Vallis. *Atmospheric and oceanic fluid dynamics: fundamentals and large-scale circulation*. Cambridge University Press, 2006.

H. A. Van der Vorst. Bi-cgstab: A fast and smoothly converging variant of bi-cg for the solution of nonsymmetric linear systems. *SIAM Journal on scientific and Statistical Computing*, 13(2):631–644, 1992. doi: 10.1137/0913035.

T. Varnai and R. Davies. Effects of cloud heterogeneities on shortwave radiation: Comparison of cloud-top variability and internal heterogeneity. *Journal of the atmospheric sciences*, 56(24):4206–4224, 1999. doi: 10.1175/1520-0469(1999)056⟨4206:EOCHOS⟩2.0.CO;2.

K. Wapler. Der einfluss des dreidimensionalen strahlungstransportes auf wolkenbildung und -entwicklung. April 2007. URL http://nbn-resolving.de/urn:nbn:de:bvb:19-68948.

K. Wapler and B. Mayer. A fast three-dimensional approximation for the calculation of surface irradiance in large-eddy simulation models. *Journal of Applied Meteorology & Climatology*, 47(12), 2008. doi: 10.1175/2008JAMC1842.1.

M. Wild, D. Folini, C. Schär, N. Loeb, E. G. Dutton, and G. König-Langlo. The global energy balance from a surface perspective. *Climate dynamics*, 40(11-12):3107–3134, 2013.

U. Wissmeier, R. Buras, and B. Mayer. pantica: A fast 3d radiative transfer scheme to calculate surface solar irradiance for nwp and les models. *Journal of Applied Meteorology & Climatology*, 52(8), 2013. doi: 10.1175/JAMC-D-12-0227.1. URL http://dx.doi.org/10.1175/JAMC-D-12-0227.1.

W. Zdunkowski, T. Trautmann, and A. Bott. *Radiation in the atmosphere: a course in theoretical meteorology*. Cambridge University Press, 2007.

Y. Zhiyin. Large-eddy simulation: Past, present and the future. *Chinese Journal of Aeronautics*, 28(1):11–24, 2015.

T. Zinner, A. Marshak, S. Lang, J. V. Martins, and B. Mayer. Remote sensing of cloud sides of deep convection: towards a three-dimensional retrieval of cloud particle size profiles. *Atmospheric Chemistry and Physics*, 8(16):4741–4757, 2008.

Zuidema and Evans. On the validity of the independent pixel approximation for boundary layer clouds observed during astex. *JOURNAL OF GEOPHYSICAL RESEARCH*, 103(D6):6059–6074, 1998. ISSN 0148-0227. doi: 10.1029/98JD00080. URL http://dx.doi.org/10.1029/98JD00080.

Acknowledgments

I would like to thank my supervisor, Bernhard Mayer for the continuous support and advice during the last years. Special thanks also go to my former advisor Robert Buras. I want to thank both of you for your extraordinary confidence and support. Thank you that you trusted me so much and allowed me to pursue new and admittedly sometimes unusual ideas. This open-minded and liberal atmosphere that you provided was certainly a fundamental basis for the success of this work.

Many-many thanks to my close colleagues and my co-advisor, George Craig, for their support in formulating this thesis. Especially Carolin Klinger and Gerard Kilroy did a fair share of proofreading over the years.

I'd also like to thank all the lovely people at the meteorological institute that enabled my growth as a researcher and as a person. Especially to those who shaped ideas in lectures and discussions during working- as well as after-hours. Without you, my friends, it would not have been possible to finish this chapter of my life and surely, would not have been as much fun. Thanks for the ride!

Last but not least I wish to thank Bjorn Stevens for the continuous support and the DKRZ, Hamburg for providing the computational resources to conduct the numerical studies.

This work was funded by the Federal Ministry of Education and Research (BMBF) through the "**H**igh **D**efinition **C**louds and **P**recipitation for **C**limate **P**rediction", the HD$(CP)^2$ project (FKZ: 01LK1208A). Section 2.1 was funded by the Federal Ministry of Transport, Building and Urban Development (BMVBS) through the German Weather Service (Extramurales Forschungsprojekt FKZ 8) and the Federal Ministry of Education and Research (BMBF) through the High Definition Clouds and Precipitation for Climate Prediction (HD (CP)2) project (FKZ: 01LK1208A).